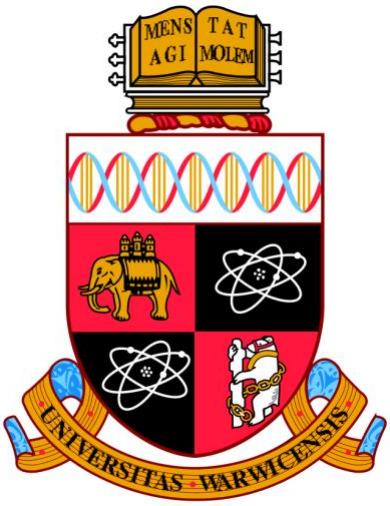

Electronic transport simulations of thermoelectric nanostructures

by

Samuel Foster

Thesis

Submitted to the University of Warwick

for the degree of

Doctor of Philosophy

School of Engineering

October 2019

Dedicated to the memory of
my father and grandfather

Table of Contents

List of figures

Acknowledgements

First and foremost, I wish to express immense gratitude to my supervisor Dr Neophytos Neophytou. I've learnt a huge amount during the last few years and that has come not only from your seemingly limitless expertise, but also from your deeply committed mentorship.

I am very grateful to my examiners Dr Ricardo Grau-Crespo and Prof David Quigley for taking the time to so thoroughly familiarize themselves with my work, particularly David for his rapid responses during the corrections procedure, as well as my examination adviser Dr Peter Brommer.

I would also like to thank Dr Mark Hadley without whom I would never have even applied for this PhD. Your advice, support and encouragement during such a difficult period of my life were truly invaluable.

Next, I would like to thank all the members of my research group who have each provided fruitful discussion and support. Thanks go to Damiano Archetti, Dhritiman Chakraborty, Laura de Sousa Oliveira, Patrizio Graziosi, and Chathu Kumarasinghe. In particular, I would like to thank Vassilios Vargiamidis with whom I collaborated with for the work in chapter 4.

I was lucky during my PhD to be able to visit the group of Marisol de Martin-Gonzalez. I would like to thank her and all her group who made me feel so welcome and gave me some wonderful insight into the workings of an experimental laboratory. I would also like to extend my thanks to the Arthur Shercliff Memorial Trust for funding this visit.

There are a great number of people who have helped make my time at Warwick such an enjoyable one. Although there are far too many to name, I would like to thank friends from the music centre, the physics department, chess society, and my housemates over the years. In addition, I thank all those at the CPS network, and the congregations of St Margaret's and Christ Church, Cheylesmore for their fellowship and prayers.

Finally I would like to thank my family who have given me such generous support and always shown great interest in my work. I owe you all so much.

Declaration

This thesis is submitted to the University of Warwick in support of my application for the degree of Doctor of Philosophy. No part of this thesis has been submitted for a research degree at any other institution.

This thesis represents my own work, except where references to other works are given, carried out under the supervision of Dr Neophytos Nephytou. The work presented in Chapter 4 was undertaken in collaboration with Dr Vassilios Vargiamidis.

The work presented in this thesis has been published in the following peer-reviewed journal articles:

- S. Foster, M. Thesberg, and N. Neophytou, "Thermoelectric power factor of nanocomposite materials from two-dimensional quantum transport simulations" *Physical Review B*, **96**, 195425, 2017. [Chapter 3]
- V. Vargiamidis, S. Foster, and N. Neophytou, "Thermoelectric power factor in nanostructured materials with randomized nanoinclusions" *Physica Status Solidi A*, **215**, 1700997 (2018) [Chapter 4]
- S. Foster, M. Thesberg, and N. Neophytou, "Quantum transport simulations for the thermoelectric power factor in 2D nanocomposites" *Materials Today Proceedings*, **8**, 690 (2019) [Chapter 5]
- S. Foster and N. Neophytou, "Doping optimization for the power factor of bipolar thermoelectric materials" *Journal of Electronic Materials*, **48**, 1889 (2018) [Chapter 6]
- S. Foster and N. Neophytou, "Effectiveness of nanoinclusions for reducing bipolar effects in thermoelectric materials" *Computational Materials Science*, **164**, 91, (2019) [Chapter 7]

Abstract

Thermoelectric materials have the unusual but highly desirable property of converting between heat and electricity. While their poor efficiencies have so far limited them to niche applications such as space exploration, they have great potential for waste heat recovery. Recent years have seen the demonstration of large performance improvements through the use of nanostructured materials. These materials have shown efficiency gains predominantly through dramatic decreases in the thermal conductivity, however it is desirable to achieve these thermal conductivity reductions without also impacting on the material's electronic properties. For this, a high level of understanding of the electronic transport through such structures is needed.

This thesis uses a variety of simulation methods—ranging from the classical to the quantum mechanical and including a Monte Carlo simulator constructed as part of the work—to explore the electronic transport through nanostructured systems. We identify key optimization guidelines to maintain and even enhance the electronic transport in the presence of nanostructures. Most significantly we outline a new concept we term "clean filtering" which shows the potential to provide substantial increases in thermoelectric performance.

Abbreviations

ADP	Acoustic-phonon deformation potential
DFT	Density functional theory
DOS	Density of states
EFM	Energy filtering mechanism
IIS	Ionized impurity scattering
LDOS	Local density of states
MC	Monte Carlo
MD	Molecular dynamics
MFP	Mean-free-path
NEGF	Non-equilibrium Green’s function
NI	Nanoinclusion
PF	Power factor
SL	Superlattice
TE	Thermoelectric

I. Introduction

1.1 Background

The Intergovernmental Panel on Climate Change Special Report *Global Warming of 1.5 °C* warns that pathways to limit global temperature rises to within 1.5 °C are becoming more and more limited and increasingly reliant on technological fixes such as Carbon Capture Storage [1]. Meanwhile, approximately two-thirds of all global energy consumption is lost as waste heat [2]. Thermoelectric (TE) materials, which convert directly between heat and electricity, could therefore play an important role in reducing energy demand and moving us towards a low-carbon future by increasing energy efficiencies through waste heat recovery. Additionally, thermoelectric generators could be strong candidates for powering Wireless Sensor Networks and the Internet of Things [3].

Currently, however, thermoelectrics remain relegated to niche applications such as space exploration (e.g. Voyager 1 and 2, and the Curiosity Rover). This is due to the poor conversion efficiencies and the high costs of current technologies. The efficiency of a TE material is quantified by the dimensionless figure of merit

$$ZT = \frac{\sigma S^2 T}{\kappa_e + \kappa_l} \tag{1.1}$$

where σ is the electrical conductivity, S is the Seebeck coefficient, κ_e is the electron thermal conductivity, and κ_l is the lattice thermal conductivity. Historically, increasing this figure above 1 has been challenging due to the variables being interdependent (Fig. 1.1a). More recently, nanoscale materials have shown the potential for significant improvements. These nanostructures, with feature sizes which vary from a few to 100s of nanometers, offer the opportunity to control electron and phonon flow to a much higher degree of precision such that the variables governing ZT can be independently fine-tuned to allow higher values, as well as introducing otherwise absent dimensional effects. This has lead to both a significant increase in the values of ZT achieved (Fig. 1.1b) and also a surge in scientific interest (Fig. 1.1c).

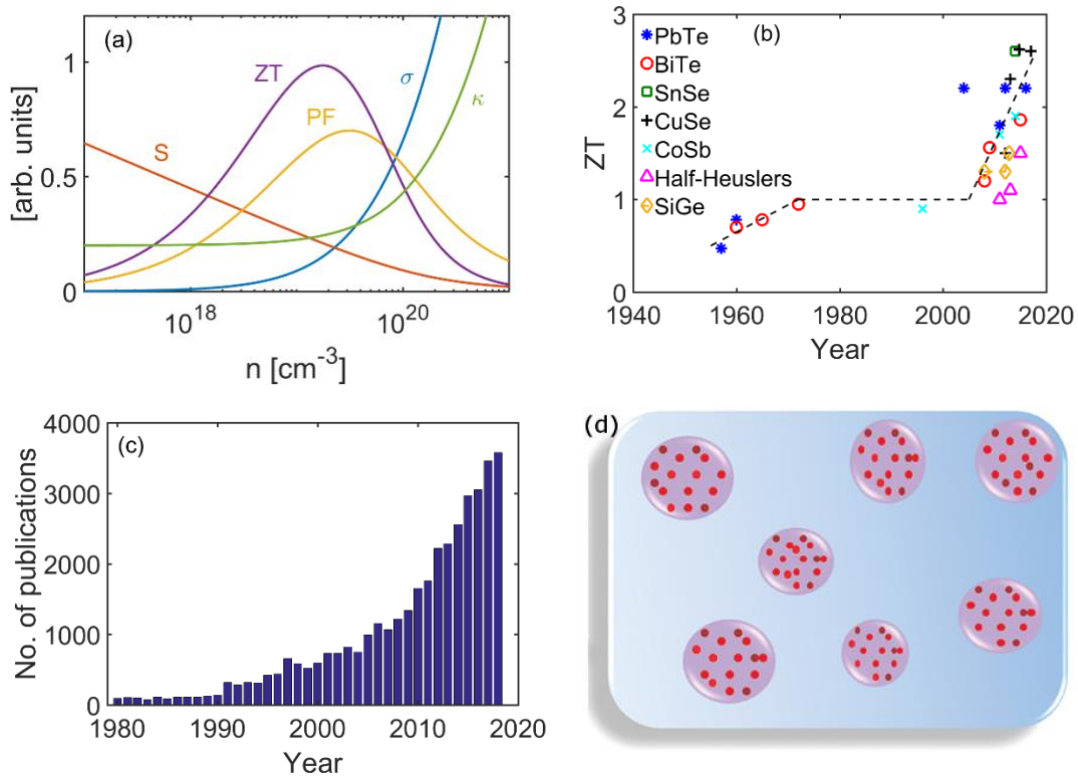

Fig. 1.1: (a) The thermoelectric coefficients σ, S, κ, σS^2 (the power factor), and ZT versus carrier concentration demonstrating the interdependency of the parameters involved. (b) a timeline of some of the best experimental ZT results reported in the literature for PbTe [4]–[7], BiTe [8]–[10], SnSe [11], CuSe [12]–[15], CoSb [16]–[18], Half-Heuslers [19]–[21], and SiGe [22]–[24]. Values for pre-1980 results are cross-referenced from Ref. [25]. (c) Publications per year on the topic of thermoelectrics. (d) A schematic representation of the modulation doping concept. Reproduced from Ref. [26].

1.2 Nanostructured thermoelectrics – thermal conductivity

Initial attempts to improve the figure of merit focused primarily on reducing the thermal conductivity. Many methods exist for reducing κ beyond bulk values. These include superlattices [27], alloying [28], heavy doping [29], nanoporous materials [30]–[32], and nanograining [33], [34]. One of the most widespread methods for the reduction of the thermal conductivity has been the use of nanoinclusions [6], [35]–[38]. These cause scattering of short wavelength phonons and can produce significant reductions in κ. This is because in common thermoelectric materials, such

as PbTe, a large portion of the phonons have mean-free-paths for scattering on the order of nanometers [39]. This technique is therefore widely used to enhance thermoelectric performance in a broad range of materials, including BiTe [40], [41], PbTe [4], [6], [42], SiGe [28], [43], ZnSb [44], FeSi [45], MnSi [46], SnTe [47], PbS [48], CuSe [49], PbZnSb [50], YbCoSb [51], and ZrNiSn [52]. Indeed, by embedding nanoinclusions within PbTe in a hierarchical manner, record high $ZT = 2.2$ values were achieved due to drastic reductions in κ, but also due to retaining high power factors [6]. Reference [53], in particular, denotes the importance of matrix/inclusion band alignment to retain the original conductivity of the material and avoid degradation in the power factor.

1.3 Nanostructured thermoelectrics – power factor

Attempts to reduce κ appear to have reached their amorphous limits, and, although there are suggestions of improving κ even beyond the amorphous limit [27], attention has instead begun to turn to the power factor, σS^2 [54]. Nanostructuring offers the possibility of independently tuning S and σ, thereby maximizing the power factor. Initial focus was on low-dimensionality, with Hicks and Dresselhaus suggesting that improvements in the Seebeck coefficient could be provided by the sharp features in the low-dimensional density of states. They predicted a ZT as large as 14 for a Bi_2Te_3 1D wire with a cross section and width of 5 Å [55]. Such high values have, however, not been demonstrated in any real materials, with the interdependence of S and σ appearing more complicated than first thought, being controlled also by the energy dependence of the scattering mechanisms [54].

Ionized impurity scattering (IIS) is the scattering mechanism which dominates power factor degradation. While σS^2 in the phonon-limited regime is maximized at carrier concentrations on the order of $n = 10^{19}$ cm^{-3}, at this level of doping IIS begins to dominate scattering, reducing mobility by up to an order of magnitude, when compared to phonon-limited transport [56]. Several techniques have been proposed to limit this effect, including modulation doping, and gating of the channel materials. Modulation doped materials are two-phase composites where dopants are contained only in one of the phases (Fig. 1.1d) [26]. Combined with band engineering, carriers can be directed into the undoped grain, giving an enhanced mobility in comparison to

uniform doping because of the reduction in IIS. While this increases electrical conductivity, it can also lead to an increase in the thermal conductivity, giving an improved power factor, but not an improved figure-of-merit. Careful designing of the material and band alignment has, however, shown the possibility of overcoming this [23]. Further improvements in both the electrical conductivity and the Seebeck coefficient have also been achieved by the inhomogeneous distribution of the dopants within the doped region [57].

One recent area of interest is that of the energy filtering mechanism (EFM). When barriers are added to a material's potential profile, carriers with energies smaller than the height of the barrier can be prevented from conducting, raising the Seebeck coefficient and consequently the power factor [58]. Initial studies investigating this effect used a semi-classical approach, employing the Boltzmann transport equation and treating the grain boundaries as scattering mechanisms [38], [59]. At the nanoscale, however, many of the characteristic lengths are shorter than the electron de Broglie wavelength, and so it becomes necessary to include quantum effects [60]. The work of Kim and Lundstrom incorporating these effects showed that optimizing parameters such as barrier height and grain size can yield improvements in the Seebeck coefficient with little effect on conductivity, and so improve *ZT* [61]. This study was, however, limited to 1D materials, thick barriers to minimize tunnelling and a uniform thermal conductivity. Experimental evidence for the effectiveness of the EFM remained elusive for a while, but reports have come out more recently that claim to demonstrate such improvements, with *ZT* values of up to 1.4 presented [44], [50].

1.4 State of the art materials

Many of the recent improvements in thermoelectric performance have come from nanostructuring [37], [62]. Altering the composition of structures at the nanoscale has provided the possibility of 'killing off' phonon flow, and so reducing thermal conductivity as discussed previously. Increases in the power factor have also been achieved. The work by Neophytou *et al.* in Ref. [33] reported a two phase crystalline and amorphous material which formed potential barriers resulting in the EFM occurring, followed by a corresponding increase in the Seebeck coefficient. The doping in this material was designed to be concentrated in the middle of the crystalline region which provides modulation doping and an increase in the electrical

conductivity. Studies of this type of geometry, which achieves simultaneous low κ and high power factor, will form a significant part of my thesis.

Another more recent attempt to reduce κ has been to introduce holes in the material. Known as nanoporous membranes, or nanomeshes, these structures have produced ZT values of 0.4-0.6 – comparable to many previously mentioned – but show superior promise as a potential thermoelectric solution due to their structural stability and the viability of large-scale production [63]. Further exploration of the parameters involved has shown that further reductions in thermal conductivity can be achieved by increasing the porosity, introducing boundary roughness scattering, and designing the arrangement of the pores within the material [64], [65] and such materials have indeed consequently shown record low thermal conductivities [66].

More recently numerous other bulk materials have been studied or characterized such as transition metal dichalcogenides [67]–[70], skutterudites [71]–[73], clathrates [74], oxides [75], Zintl phases [76], [77], silicides [78], and half-Heuslers [21], [79], [80]. A large number of these materials demonstrate ZT above 1, primarily by the reduction of the thermal conductivity, κ [81].

In this thesis we present electronic transport simulations of nanostructured geometries, representative of some of the most promising results in thermoelectric materials. Using methods ranging from the classical Boltzmann transport formalism to the quantum mechanical non-equilibrium Green's function we provide guidelines for the enhancement of the thermoelectric properties of such systems.

1.5 Thesis outline

In chapter 2 we give an outline of the Boltzmann transport formalism and its relation to thermoelectric transport as well as the theory and our implementation of the non-equilibrium Green's function (NEGF) method.

In chapter 3 we use the NEGF method to investigate the effect of nanoinclusions on the electronic and thermoelectric coefficients of two-dimensional nanoribbon geometries. We show that the presence of nanoinclusions within a matrix material offers opportunities for only weak energy filtering, significantly lower in comparison to superlattices, and thus only moderate power factor improvements. However, we describe how such nanocomposites can be optimized to limit degradation in the thermoelectric power factor and elaborate on the conditions that

achieve the aforementioned mild improvements. Importantly, we show that under certain conditions, the power factor is independent of the density of nanoinclusions, meaning that materials with large nanoinclusion densities which provide very low thermal conductivities can also retain large power factors and result in large *ZT* figures of merit.

In chapter 4 we extend the work presented in chapter 3 to consider the effect of variability in the nanoinclusions on the thermoelectric properties using the NEGF method. The effect of randomness of the NIs on the thermoelectric power factor is investigated by varying the positions, diameter, and heights of the barriers according to a Gaussian probability distribution. It is found that the power factor shows indications of tolerance to variations in the parameters of the NIs when the Fermi level is placed into the bands and the barrier height is of a similar value.

In chapter 5 we extend the work presented in chapter 3 to consider the effect that nanoinclusions and voids have on the electronic and thermoelectric coefficients of two-dimensional geometries, again using the NEGF method. The power factor is shown to be approximately independent of nanoinclusion and void density in the ballistic case. On the other hand, in the presence of phonon scattering voids degrade the power factor and their influence increases with density. However, we also present experimental and theoretical results from the literature showing that the thermal conductivity drops far more significantly in such structures, meaning increases in *ZT* can be expected.

Chapter 6 is the first of two chapters looking at the bipolar effect which is often a limiting factor for many important thermoelectric materials at high temperatures. This chapter uses the Boltzmann transport formalism and a two-band model to investigate the doping optimization of such materials showing the detrimental impact that rising temperatures have if the doping (and the Fermi level) is not optimized for each operating temperature. We also show that the doping levels for optimized power factors at a given operating temperature differ in bipolar systems compared to unipolar ones. We show finally that at 600 K, in a bipolar material with bandgap approximately that of Bi_2Te_3, the optimal doping required can reside between 10% and 30% larger than that required for an optimal unipolar material depending on the electronic scattering details of the material.

In chapter 7 we combine the topics of previous chapters by considering the impact of nanoinclusions on the bipolar effect. Using the NEGF transport formalism, we simulate electronic transport through two-dimensional systems containing densely packed nanoinclusions, separated by distances similar to the electron mean-free-path. Specifically, considering an n-type material, where the bipolar effect comes from the valence band, we insert nanoinclusions that impose potential barriers only for the minority holes. We then extract the material's electrical conductivity, Seebeck coefficient, and electronic thermal conductivity including its bipolar contribution. We show that nanoinclusions can indeed have some success in reducing the minority carrier transport and the bipolar effect on both the electronic thermal conductivity and the Seebeck coefficient. The benefits from reducing the bipolar conductivity are larger the more conductive the minority band is to begin with (larger hole mean-free-path in particular), as expected. Interestingly, however, the benefits on the Seebeck coefficient and the power factor are even more pronounced not only when the minority mean-free-path is large, but when it is larger compared to the majority conduction band mean-free-path. Finally, we extract an overall estimate for the benefits that nanoinclusions can have on the *ZT* figure of merit.

In chapter 8 we introduce the theory of the electron Monte Carlo method and outline our implementation of it. We then introduce a new thermoelectric enhancement concept that we term "clean filtering". In this strategy the EFM is brought about by modulation doping. By doping regions of the material while also leaving strips undoped, potential barriers are produced that increase the Seebeck coefficient through the EFM. Such potential barriers would normally be accompanied by a significant reduction in the conductance, but due to the "cleaning" of the barrier regions through the removal of dopants there is a decrease in the effect of IIS and the conductance consequently recovers. Using the Monte Carlo simulator we have constructed we show that "clean filtering" can provide power factors more than double that of a pristine material even though we do not present any optimization of the concept.

Finally, in chapter 9 we summarize the thesis and present some possibilities for future work.

II. Electronic transport theory

2.1 Introduction

In this chapter we present the theory behind electronic and thermoelectric transport including the Boltzmann transport theory and the non-equilibrium Green's function (NEGF) formalism. The specific implementation of the NEGF framework is also outlined.

2.2 Thermoelectric theory

In 1821 Johann Seebeck discovered that a closed circuit formed of two dissimilar metals would deflect a magnetic compass when heated from one end. Although he erroneously termed this phenomenon the "thermomagnetic effect", he carefully documented the strength of the deflection in a wide range of materials. In the case of an open-circuit, the temperature difference ΔT causes a potential difference ΔV and we can consequently define the Seebeck coefficient:

$$S = -\frac{\Delta V}{\Delta T} \tag{2.1}$$

This was followed in 1834 by the discovery by Jean Peltier that applying a current through two dissimilar metals results in a cooling/heating effect dependent on the direction of the current. The rate of heat current I_q for an electric current I is given by

$$I_q = \Pi I \tag{2.2}$$

where Π is the Peltier coefficient.

Finally, in 1855, Lord Kelvin unified these two effects by showing that the two coefficients can be related by the simple expression:

$$\Pi = TS \tag{2.3}$$

The performance of a thermoelectric material is governed by a figure of merit, ZT, as introduced in chapter 1. The maximum efficiency is then given by [82]

$$\eta_{\max} = \frac{T_H - T_C}{T_H} \frac{\sqrt{1+ZT_m} - 1}{\sqrt{1+ZT_m} + T_C/T_H} \tag{2.4}$$

where T_H is the temperature of the hot contact, T_C is the temperature of the cold contact, and $T_m = (T_H + T_C)/2$. It can be seen that as $ZT_m \to \infty$, η_{max} approaches the Carnot efficiency $(T_H - T_C)/T_H$. In order to maximize the efficiency of thermoelectric devices materials with high values of *ZT* must be found.

As discussed in chapter 1 this is not trivial due to the interdependence of the parameters involved (see Fig. 1.1a). In particular it should be noted that as the carrier concentration is increased σ increases while S decreases. The power factor consequently shows a peak near to the band edge. Methods to break this interdependence have included modulation doping and energy filtering. Likewise, while σ increases this is matched by an increase in κ_e due to the Wiedemann-Franz law:

$$\kappa_e = L\sigma T \tag{2.5}$$

where L is the Lorenz number. For a metal this number can be shown to be equal to $L = \frac{\pi^2}{3}\left(\frac{k_B}{q_0}\right)^2 = 2.44\times10^{-8}\,\mathrm{W\Omega K^{-2}}$ (where k_B is the Boltzmann constant and q_0 is the charge on the electron), and such a value typically also holds for highly degenerate semiconductors. However, it has been shown that the Wiedemann-Franz law breaks down in a variety of cases, potentially offering sources of *ZT* optimization [83].

2.3 Landauer formalism

In the Landauer formalism the electric current is given by

$$I = \frac{2q_0}{h}\int \tilde{T}(E)M(E)(f_1 - f_2)dE \tag{2.6}$$

where h is the Planck constant, $\tilde{T}(E)$ is the transmission for a single mode[1], E is energy, $M(E)$ is the number of modes, and $f_{1/2}$ are the Fermi-Dirac distributions of the contacts:

$$f = \frac{1}{e^{(E-E_F)/k_BT} + 1} \tag{2.7}$$

[1] Note that the quantities $T(E)$ and $Tr(E)$ are used interchangeably in this thesis to mean the transmission times the number of modes, and are referred to here on in as just "the transmission" unless otherwise stated.

where E_F is the Fermi level. Note that from Eqs. (2.6) and (2.7) it can be seen that currents can be driven either by a difference in Fermi level, or by a difference in temperature (see Fig. 2.1).

The total current through a channel can then be expressed as the sum of the voltage-induced current and the temperature-induced current:

$$I = G\Delta V + SG\Delta T \tag{2.8}$$

where G is the conductance, ΔV is the potential difference and ΔT is the temperature difference.

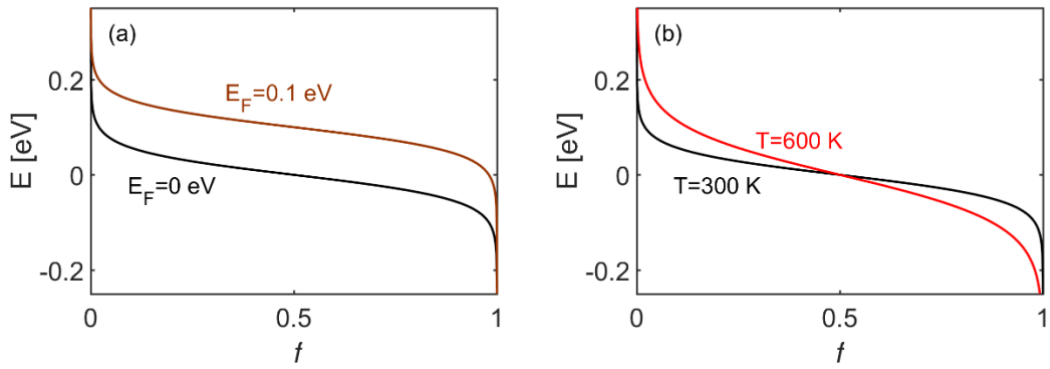

Fig. 2.1: (a) The Fermi-Dirac distributions of a contact with E_F = 0 eV (black line) and with E_F = 0.1 eV (brown line), both at T = 300 K, and (b) the Fermi-Dirac distributions of a contact with T = 300 K (black line) and T = 600 K (red line), both at E_F = 0 eV.

2.4 Boltzmann transport

The semi-classical Boltzmann transport equation for electrons is given by [84]

$$\frac{\partial \tilde{f}}{\partial t} + v \cdot \nabla_r \tilde{f} + \mathbf{F} \cdot \nabla_p \tilde{f} = \left.\frac{\partial \tilde{f}}{\partial t}\right|_{coll} \tag{2.9}$$

where $\tilde{f} = \tilde{f}(\mathbf{r}, \mathbf{p}, t)$ is the distribution function (a number between one and zero describing the average distribution of carriers in position, momentum and time), $\mathbf{r}$ is position, $\mathbf{p}$ is momentum, t is time, v is velocity, $\mathbf{F}$ is the electromagnetic force, $\left.\frac{\partial \tilde{f}}{\partial t}\right|_{coll}$ is the rate of change of the distribution function due to collisions, and

$$\nabla_r \tilde{f} = \frac{d\tilde{f}_x}{dx}\hat{x} + \frac{d\tilde{f}_y}{dy}\hat{y} + \frac{d\tilde{f}_z}{dz}\hat{z} \tag{2.10}$$

$$\nabla_p \tilde{f} = \frac{d\tilde{f}_x}{dp_x}\hat{x} + \frac{d\tilde{f}_y}{dp_y}\hat{y} + \frac{d\tilde{f}_z}{dp_z}\hat{z} \tag{2.11}$$

Since the distribution function, $\tilde{f}$, appears on both sides of the equation it is normally necessary to solve the Boltzmann transport equation self-consistently, however in this work we employ the commonly used relaxation time approximation which simplifies the scattering term, breaking its dependence on the distribution function [56], [85]–[89].

Under the linearized Boltzmann transport regime under a relaxation time approximation, the electronic transport coefficients - electrical conductivity (σ), the Seebeck coefficient (S) and the electronic thermal conductivity (κ_e) - are given by [86], [87]

$$\sigma = q_0^2 \int_{-\infty}^{\infty} dE \left(-\frac{\partial f}{\partial E} \right) \Xi(E) \tag{2.12}$$

$$S = \frac{q_0 k_B}{\sigma} \int_{-\infty}^{\infty} dE \left(-\frac{\partial f}{\partial E} \right) \Xi(E) \left(\frac{E - E_F}{k_B T} \right) \tag{2.13}$$

$$\kappa_e = k_B^2 T \int dE \left(-\frac{\partial f}{\partial E} \right) \Xi(E) \left(\frac{E - E_F}{k_B T} \right)^2 - \sigma S^2 T \tag{2.14}$$

where the quantity $\Xi(E)$ is called the transport distribution function and is defined as

$$\Xi(E) = v^2(E) \tau(E) g(E) \tag{2.15}$$

where $v(E) = \frac{1}{\hbar} \frac{\partial E(k)}{\partial k}$ is the bandstructure velocity, τ is the relaxation time and g is the density of states (DOS) and k is the electron wavevector. In this thesis we will only consider bandstructures described by an effective mass approximation: $E(k) = \frac{\hbar^2 k^2}{2m^*}$ where $\hbar$ is the reduced Planck's constant, and m^* is the effective mass. The DOS is dependent on bandstructure details and dimensionality, but for a single isotropic parabolic conduction band becomes:

$$g_{1D} = \frac{1}{\pi \hbar} \sqrt{\frac{2m^*}{(E - E_C)}} \theta(E - E_C) \tag{2.16}$$

$$g_{2D} = \frac{m^*}{\pi \hbar^2} \theta(E - E_C) \tag{2.17}$$

$$g_{3D} = \frac{m^*}{\pi^2 \hbar^3} \sqrt{2m^*(E - E_C)} \theta(E - E_C) \tag{2.18}$$

where E_C is the conduction band edge and θ is the Heaviside function. In Fig. 2.2 we show schematics of the typical shape of g in the cases of 1D (Fig. 2.2a), 2D (Fig. 2.2b), and 3D (Fig. 2.2c).

The transport distribution can also be expressed in terms of the transmission of a single mode and number of modes as [90]**:**

$$\Xi(E) = \frac{2}{h}\tilde{T}(E)M(E) \tag{2.19}$$

The number of modes is also dependent on the dimensionality of the system:

$$M_{1D} = \theta(E - E_C) \tag{2.20}$$

$$M_{2D} = \frac{\sqrt{2m^*(E - E_C)}}{\pi\hbar}\theta(E - E_C) \tag{2.21}$$

$$M_{3D} = \frac{m^*}{2\pi\hbar^2}(E - E_C)\theta(E - E_C) \tag{2.22}$$

Schematics of the typical shapes of the number of modes are shown in Fig. 2.2 for the cases of 1D (Fig. 2.2d), 2D (Fig. 2.2e), and 3D (Fig. 2.2f).

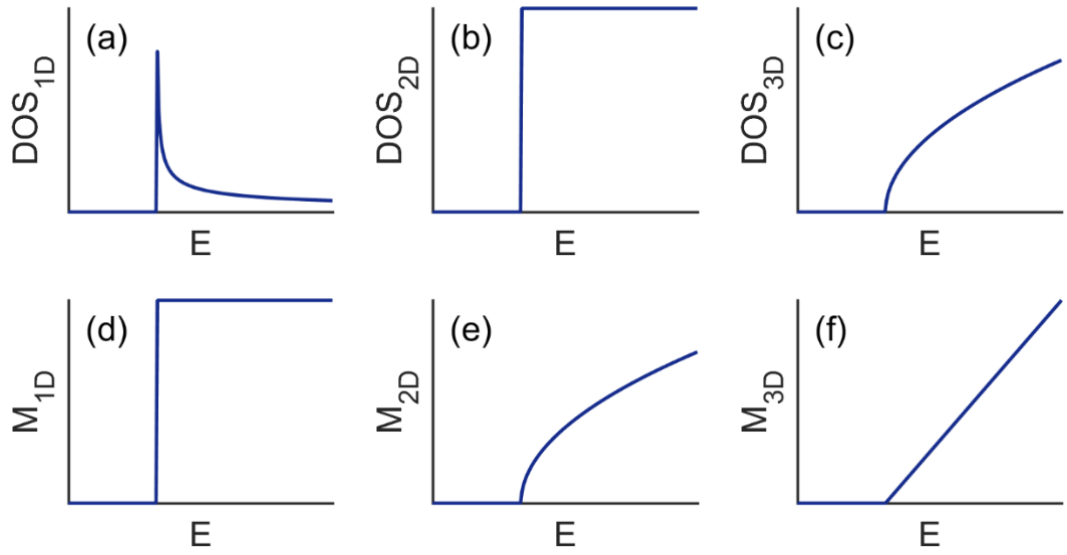

Fig. 2.2: Schematics of (a-c) the density of states and (d-f) the number of modes versus energy for 1D, 2D and 3D under the parabolic band approximation.

2.5 Non-equilibrium Green's function

Some of the most promising results in thermoelectrics have come from nanostructured materials as discussed in Chapter 1. While these materials show

promising values for the thermal conductivity, a clear understanding of how best to optimize their electronic properties remains missing. Due to the small feature sizes that characterize these structures it is necessary to use a simulation method that captures all important quantum mechanical details such as resonances and quantum tunnelling, as well as details of electron-phonon scattering and complex geometries.

In chapters 3, 4, 5, and 7 we use the non-equilibrium Green's function (NEGF) formalism [91]–[96]; a quantum mechanical transport simulation method capable of capturing all important details such as those described above. While we perform only electronic transport simulations in this thesis the NEGF formalism is applicable to both electron and phonon transport [94]. The NEGF is a versatile formalism able to treat small electronic devices quantum mechanically and atomistically (although our implementation in this thesis is not atomistic). It has previously been applied to a wide variety of problems, including carbon nanotubes [97], silicon nanowires [98], graphene nanoribbons [99], and superlattice geometries [100]–[102].

In this section we outline the theory behind this method as it applies to electrons and describe the specific implementation used throughout this thesis. We begin by introducing the Green's function itself, before describing how to construct the various components that go into its form.

2.5.1 The Green's function

Green's functions are a powerful mathematical tool used in a wide range of physical systems to describe impulse response. In electron transport they represent the propagation of a wave function excitation to any other point in the system, or from a slightly more particle-based view, the evolution of an electrons path from its injection into the device until it loses coherence (either by scattering into a new state or by exiting the device into a contact).

In the NEGF method a system/device, described by a Hamiltonian H, is connected to two contacts (left and right) which are represented by self-energy functions Σ_L and Σ_R (see Fig. 2.3). These self-energies represent the influence of the semi-infinite left and right leads on the device, respectively and through which charge can flow in/out of the device; these will be discussed further in section 2.5.3. The effect of electron-phonon scattering processes are incorporated into the NEGF

formalism through an additional self-energy function Σs which will be discussed in section 2.5.4.

The Green's function, G[2], of a device is given by

$$G(E) = [EI - H - \Sigma(E)]^{-1} \tag{2.23}$$

where I is the identity matrix (of the same size as the device Hamiltonian), H is the device Hamiltonian and Σ(E) is the sum of the self-energies:

$$\Sigma(E) = \Sigma_{\mathrm{L}}(E) + \Sigma_{\mathrm{R}}(E) + \Sigma_{\mathrm{S}}(E) \tag{2.24}$$

as introduced above.

Below we construct these necessary elements beginning with the device Hamiltonian.

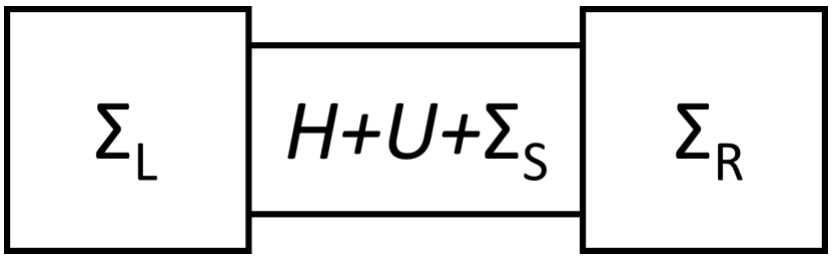

Fig. 2.3: A simple schematic of the NEGF description of a system with two contacts.

2.5.2 Choice of Hamiltonian for description of channel

In this thesis we discretize the Schrödinger equation under the effective mass approximation. This is equivalent to the single orbital tight binding Hamiltonian expressed with a complete and orthonormal basis set of s-orbitals (also called linear combination of atomic orbitals) [103]. The objective of this method is to represent the wave function of a particle in our system as a linear combination of known states localized at discrete lattice points.

The effective mass we choose is assumed to be uniform throughout the channel, although the NEGF formalism can also model systems with a spatially varying effective mass, as well as multi-band effective mass Hamiltonians and atomistic Hamiltonians. We take the relevant band to be the conduction band, although in chapter 7 we explain how to combine such simulations in order to describe bipolar systems where contributions come from both electrons and holes.

[2] Note that outside of Section 2.5 the symbol *G* is exclusively used to refer to the conductance.

In the single effective mass case, the energy levels of a conduction band are described by the simple relation:

$$E(k) = E_c + \frac{\hbar^2 k^2}{2m^*} \tag{2.25}$$

where E_c is the conduction band minimum, k is the wavevector, and m^* is the effective mass. This dispersion relation represents the description of the electron energy levels in a pristine channel material. In order to model the effect of nanostructures (specifically, in this work, nanoinclusions) we introduce a change in the band profile which is caused by the introduction of a different species within the lattice that distorts the original E_c and which we represent by a band offset term, $U(x)$ (see Fig. 2.4) which is added into our Schrödinger equation and consequently the onsite energies of the matrix Hamiltonian (as seen in the discussion below). This built-in potential can result from band discontinuities or electrostatics. It is possible to capture the electrostatics by coupling to the Poisson equation (as described in chapter 3), however, in this work we do not couple to the Poisson equation and instead model the features we are interested in by adding U by hand.

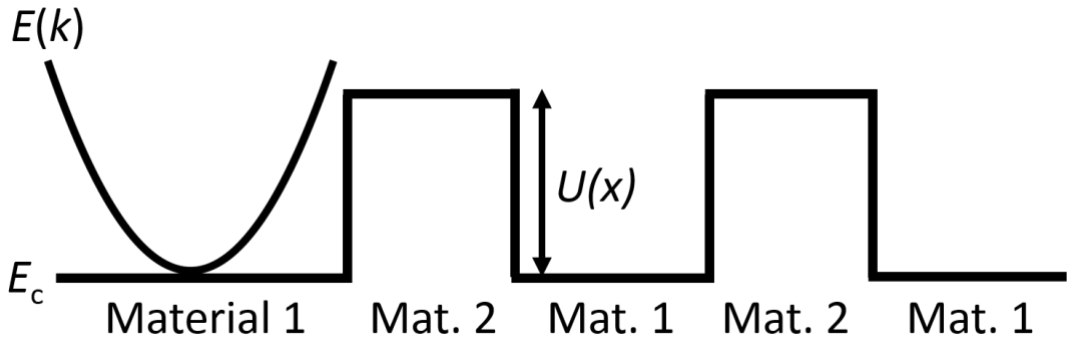

Fig. 2.4: Schematic of the band profile in a nanostructured material showing the parabolic conduction band, $E(k)$, and the band offset, $U(x)$, between two materials in the lattice.

2.5.2.1 The Hamiltonian in 1D

In order to construct our channel Hamiltonian we begin with the one-dimensional time-independent Schrödinger equation of the form

$$\hat{H}\psi(x) = \left[E_c + U(x) - \frac{\hbar^2}{2m^*}\frac{\partial^2}{\partial x^2} \right]\psi(x) = E\psi(x) \tag{2.26}$$

where $\psi(x)$ is the wave function, $U(x)$ is the band offset term.

In order to solve this numerically we discretize the wave function across our simulation domain (see Fig. 2.5) and likewise the Hamiltonian, rewriting it as the sum of the individual lattice Hamiltonians and the interactions between lattice points

$$H = H_0 + \tilde{V} \tag{2.27}$$

where

$$H_0 = \sum_{j=1}^{n} H_\alpha^j \tag{2.28}$$

$$\tilde{V} = \sum_{j=1}^{n} \Delta\tilde{V} \tag{2.29}$$

where H_0 is the sum of the Hamiltonians at each lattice point, H_α^j, and $\tilde{V}$ is the sum of all the contributions to the potential energy, $\Delta\tilde{V}$, due to all other lattice points:

$$H_\alpha^j = -\frac{\hbar^2}{2m^*}\frac{d^2}{dx^2} + \tilde{V}(x_j - r_j) \tag{2.30}$$

$$\Delta\tilde{V} = \sum_{k\neq j}^{n} \tilde{V}(x_j - r_k) \tag{2.31}$$

where $\tilde{V}(x_j\text{-}r_k)$ is the potential energy for the jth lattice point (located at position x_j) due to the kth lattice point (located at position r_k).

As stated, we use single orbital tight binding, i.e. each lattice point in the channel is assumed to have one s-orbital (orthogonal to the orbitals on the other lattice points), and only nearest-neighbour interactions are included. The matrix elements of the Hamiltonian expressed in Dirac notation then become

$$\langle j'|H|j\rangle = \langle j'|H_0|j\rangle + \langle j'|H_0|j+1\rangle + \langle j'|H_0|j-1\rangle + \langle j'|\tilde{V}|j\rangle \tag{2.32}$$

We now set

$$\langle j|'H_0|j\rangle = E_s \tag{2.33}$$

$$\langle j'|H|j\pm 1\rangle = V_s \tag{2.34}$$

$$\langle j'|\tilde{V}|j\rangle = V_j \tag{2.35}$$

which in matrix form looks like

$$H = \begin{pmatrix} E_s + V_1 & V_s & 0 & \cdots & 0 \\ V_s & E_s + V_2 & V_s & \ddots & \vdots \\ 0 & V_s & \ddots & V_s & 0 \\ \vdots & \ddots & V_s & E_s + V_{n-1} & V_s \\ 0 & \cdots & 0 & V_s & E_s + V_n \end{pmatrix} \tag{2.36}$$

where n is the number of lattice points in the system (or the number of lattice points in the x-direction for a larger dimensional system). It now remains to figure out the quantities E_s+V_j and V_s which are the onsite energies and the coupling between the sites respectively.

To do so we begin again with the one-dimensional time-independent Schrödinger equation

$$\hat{H}\psi(x) = \left[E_c + U(x) - \frac{\hbar^2}{2m^*}\frac{\partial^2}{\partial x^2} \right]\psi(x) = E\psi(x) \tag{2.37}$$

Using the finite difference method (discretizing in real space) and assuming a 1D system with a lattice spacing, a (see Fig. 2.5), we can express the second derivative of the wave function in Eq. (2.37) at a particular point in the channel, x_j as

$$\left[\frac{\partial^2\psi}{\partial x^2}\right]_{x=x_j} \approx \frac{\frac{\psi(x_{j+1})-\psi(x_j)}{a} - \frac{\psi(x_j)-\psi(x_{j-1})}{a}}{a} = \frac{\psi(x_{j+1}) - 2\psi(x_j) + \psi(x_{j-1})}{a^2} \tag{2.38}$$

The Schrödinger equation in Eq. (2.26) with the above approximation for the derivative then becomes

$$\hat{H}\psi(x_j) = E_c\psi(x_j) + U(x_j)\psi(x_j) - \frac{\hbar^2}{2m^*}\left(\frac{\psi(x_{j-1}) - 2\psi(x_j) + \psi(x_{j+1})}{a^2}\right) = E\psi(x_j) \tag{2.39}$$

or rearranging

$$-t\psi(x_{j-1}) + (E_c + 2t + U(x_j))\psi(x_j) - t\psi(x_{j+1}) = E\psi(x_j) \tag{2.40}$$

where we have set $t \equiv \hbar^2/2m^*a^2$, which is the hopping parameter and represents the easiness of transport from node to node. We can now express Eq. (2.40) in matrix form as

$$H\psi = \begin{pmatrix} E_c + U_1 + 2t & -t & 0 & \cdots & 0 \\ -t & E_c + U_2 + 2t & -t & \ddots & \vdots \\ 0 & -t & \ddots & -t & 0 \\ \vdots & \ddots & -t & E_c + U_{n-1} + 2t & -t \\ 0 & \cdots & 0 & -t & E_c + U_n + 2t \end{pmatrix} \begin{pmatrix} \psi_1 \\ \psi_2 \\ \vdots \\ \psi_{n-1} \\ \psi_n \end{pmatrix} = E\psi$$

(2.41)

where $U_j = U(x_j)$, and n is the number of lattice points in the system (or the number of lattice points in the x-direction for a larger dimensional system).

If we now compare this form of the Hamiltonian with that presented in Eq. (2.36) we can see that a natural correspondence comes about, namely

$$E_s + V_j = E_c + 2t + U(x_j) \tag{2.42}$$

$$V_s = -t \tag{2.43}$$

Further details on the equivalency of these two methods can be found in Ref. [103].

We wish to note again at this point that in this thesis we are not working atomistically and so neither these lattice points nor the lattice spacing represent real atomistic parameters. However, it can be shown that this model is accurate provided that the spacing a is small enough such that t is greater than the energy of range of interest [94] (in the majority of the following work this is up to ~0.4 eV, and since we primarily take $m^* = m_0$ where m_0 is the mass of the electron, this gives us a lattice spacing of a = 0.5 nm which we use throughout the thesis). Note, also, that the system described so far is closed, and as such will provide particle in a box solutions to the eigenvalue problem. Assuming periodicity within these boundary conditions we can also derive the energy dispersion relation, however in the NEGF formalism we do not need these and are able to open up the system using the contact self-energies, $\Sigma_{L/R}$, which we get to shortly. First, we discuss the construction of the Hamiltonian in 2D.

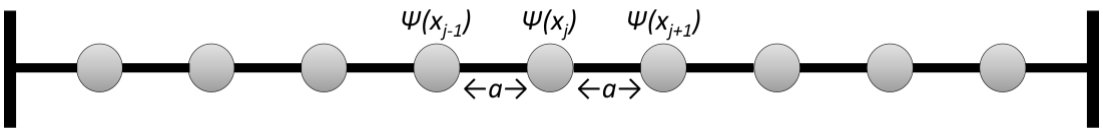

Fig. 2.5: Schematic of the 1D lattice with discretized wave function.

2.5.2.2 The Hamiltonian in 2D

While the scheme outlined above holds for the modelling of a 1D system, we wish to expand this to model a 2D system. In this case, each lattice point is connected to four others, as shown in Fig. 2.6a, and the Hamiltonian must consequently be expanded. As shown in Fig. 2.6b, the 2D system can be treated as a series of connected 1D systems. The 2D Hamiltonian therefore follows naturally:

$$H_{2D} = \begin{pmatrix} A & -\tau & 0 & 0 \\ -\tau & B & -\tau & \vdots \\ 0 & -\tau & \ddots & -\tau \\ 0 & \cdots & -\tau & M \end{pmatrix} \tag{2.44}$$

where A, B… are matrices of the form

$$M = \begin{pmatrix} E_C + U_{1,m} + 4t & -t & 0 & 0 \\ -t & E_C + U_{2,m} + 4t & -t & \vdots \\ 0 & -t & \ddots & -t \\ 0 & \cdots & -t & E_C + U_{n,m} + 4t \end{pmatrix} \tag{2.45}$$

where m is the number of lattice points in the y-direction, and where τ is a matrix of the form

$$\tau = \begin{pmatrix} t & 0 & 0 \\ 0 & \ddots & 0 \\ 0 & 0 & t \end{pmatrix} \tag{2.46}$$

A, B… and τ have dimensions of $n \times n$. Each matrix A, B represents the Hamiltonian of a 1D system/layer (see in Fig. 2.6b) and the coupling between each layer is given by τ, i.e. τ is a matrix describing the nearest-neighbour connection of each discretized node in one layer to the next. Note that the diagonal elements in Eq. (2.45) now have an addend of $4t$ as opposed to $2t$ as in Eq. (2.41). This comes from the fact each node now has 4 nearest neighbours (Fig. 2.6a) rather than 2, and can be seen mathematically from the second derivative in the Schrödinger equation which must now be taken in two dimensions.

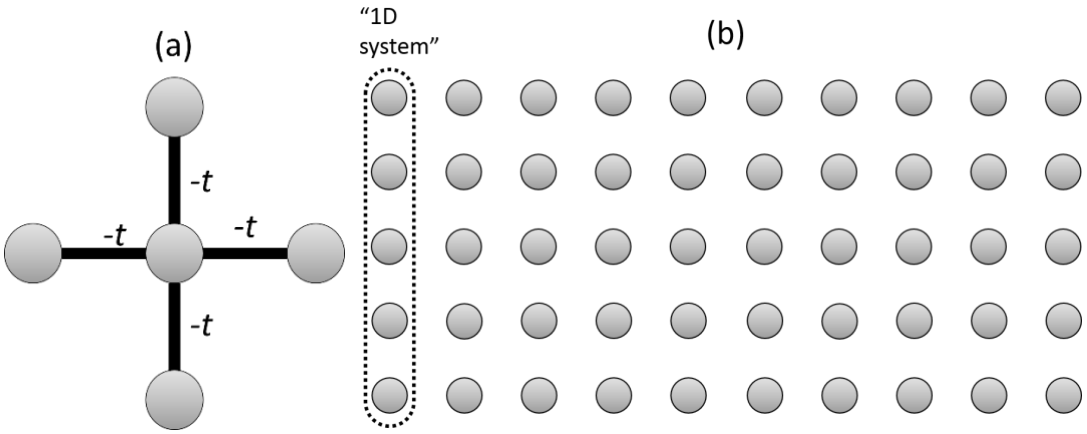

Fig. 2.6: (a) Schematic of the lattice point dependencies for a 2D system, (b) The lattice points in a 2D system, noting how one column can be treated as a 1D system coupled to another 1D system.

2.5.3 The contact self-energies

We now discuss the treatment of the contacts in NEGF, i.e., answering the question: what happens when we go from a closed system to an open system? As introduced in Eq. (2.23) we model these as an additional term added onto the Hamiltonian and below we derive their necessary form in 1D and 2D.

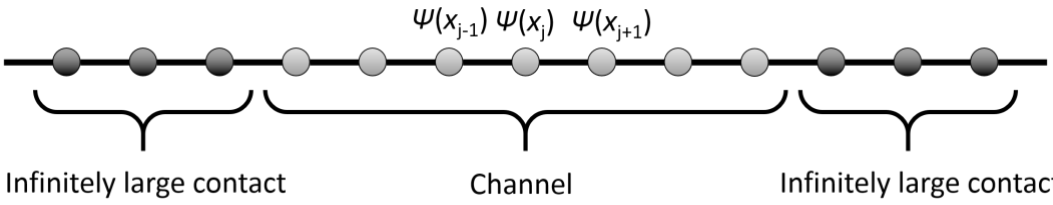

Fig.2.7: Schematic of the lattice points with open boundary conditions where we have now connected the channel to semi-infinite contacts.

2.5.3.1 The contacts in 1D

To find the form of the self-energies we consider an isolated contact with a wave function Φ, before connecting this to the wave function of the channel ψ. We begin with the Schrödinger equation for the isolated first lattice point in the channel

$$\hat{H}\psi = E\psi = (E_c + U_1 + 2t)\psi \tag{2.47}$$

We then connect this lattice point to the first lattice point in the contact

$$E\psi = (E_c + U_1 + 2t)\psi - t\Phi_{-1} \tag{2.48}$$

where Φ_{-1} is the wave function of the contact's first lattice point. We assume a contact Hamiltonian of the same form as seen in Eq. (2.40) (i.e. we assume that the contact is of the same nature as the channel, specifically discretizing the Schrödinger equation again with the same lattice spacing, *a*):

$$E\Phi_\eta = -t\Phi_{\eta-1} + (E_c + 2t)\Phi_\eta - t\Phi_{\eta+1} \tag{2.49}$$

where Φ_η is the wave function of the ηth lattice point in the contact. Assuming plane waves we can write the wave function at any point as the sum of the incident and reflected waves as

$$\Phi_\eta = Be^{ik\eta a} + Ce^{-ik\eta a} \tag{2.50}$$

Since the wave functions of the contact and the channel must match at the interface (as a consequence of continuity) we can then substitute in the values for η=0 and η=-1 (at the interface and the first lattice point of the contact) to get

$$\psi \equiv \Phi_0 = B + C \tag{2.51}$$

$$\Phi_{-1} = Be^{-ika} + Ce^{ika} \tag{2.52}$$

and substituting for *C* in Eq. (2.52) get

$$\Phi_{-1} = Be^{-ika} + (\psi - B)e^{ika} = \psi e^{ika} + B(e^{-ika} - e^{ika}) \tag{2.53}$$

Substituting Eq. (2.53) into Eq. (2.48) we can then see that

$$E\psi = (E_c + U + 2t)\psi - te^{ika}\psi + tB(e^{ika} - e^{-ika}) \tag{2.54}$$

or

$$E\psi = (H + \Sigma)\psi + S \tag{2.55}$$

where *H* is the Hamiltonian of the isolated system as before (see Eq. (2.47)), $\Sigma = -te^{ika}$ is called the contact self-energy and provides a modification to the closed boundary to open it up, and $S = tB(e^{-ika} - e^{ika})$ is a source term representing channel excitations from the contact. We have now found a new Schrödinger equation with a modified Hamiltonian which now describes open boundary conditions. We now construct a more general representation for the two-dimensional contact.

2.5.3.2 The contacts in 2D

In 1D it is possible to write down an explicit form for Σ, the self-energy modification to the Hamiltonian, as seen above. However, in 2D the contact interface

is no longer a single lattice point, but a layer of lattice points. The self-energy, Σ, must therefore become a matrix, but how do we now construct it? We will follow the same logic as in 1D - beginning with the isolated contact and channel before connecting the two.

Following Ref. [94] we begin with the Hamiltonian of the isolated contact

$$[E - H_{\mathrm{R}}]\{\Phi_{\mathrm{R}}\} = 0 \tag{2.56}$$

where H_{R} and Φ_{R} are the Hamiltonian and wave function of the reservoir, respectively. This is then modified to include electron flow as

$$[EI_{\mathrm{R}} - H_{\mathrm{R}} + i0^{+}_{\mathrm{R}}]\{\Phi_{\mathrm{R}}\} = \{S_{\mathrm{R}}\} \tag{2.57}$$

where I_{R} is an identity matrix of the same size as H_{R}, $0^{+}_{\mathrm{R}} = 0^{+}[I_{\mathrm{R}}]$ is a positive infinitesimal times the identity matrix that represents the extraction of electrons from the contact, and S_{R} is a source term representing the re-injection of electrons from external sources [94]. Naturally, in a simulation it is not possible to add a true infinitesimal, a typical value for 0^{+} in a simulation therefore is $0^{+} \approx 10^{-11}$.

If we now connect the Hamiltonian of one isolated contact with that of the channel we can write

$$\begin{pmatrix} EI_{\mathrm{R}} - H_{\mathrm{R}} + i0^{+}_{\mathrm{R}} & -\tau^{+} \\ -\tau & EI - H \end{pmatrix} \begin{pmatrix} \Phi_{\mathrm{R}} + \chi \\ \psi \end{pmatrix} = \begin{Bmatrix} S_{\mathrm{R}} \\ 0 \end{Bmatrix} \tag{2.58}$$

where χ is a modification to the pristine (isolated) contact due to the presence of the channel. We want to write this equation in a similar form to Eq. (2.55), and figure out what Σ and S_{R} look like for this system. We begin by multiplying out the matrices as

$$(EI_{\mathrm{R}} - H_{\mathrm{R}} + i0^{+}_{\mathrm{R}})(\Phi_{\mathrm{R}} + \chi) - \tau^{+}\{\psi\} = S_{\mathrm{R}} \tag{2.59}$$

$$-\tau(\Phi_{\mathrm{R}} + \chi) + (EI - H)\psi = 0 \tag{2.60}$$

Rearranging and using Eq. (2.57) these can be expressed as

$$(EI_{\mathrm{R}} - H_{\mathrm{R}} + i0^{+}_{\mathrm{R}})\{\chi\} - \tau^{+}\{\psi\} = 0 \tag{2.61}$$

$$(EI - H)\{\psi\} - \tau\{\chi\} = \tau\{\Phi_{\mathrm{R}}\} \tag{2.62}$$

Rearranging Eq. (2.61) we can write

$$\{\chi\} = \frac{\tau^{+}\{\psi\}}{(EI_{\mathrm{R}} - H_{\mathrm{R}} + i0^{+}_{\mathrm{R}})} = G_{\mathrm{R}}\tau^{+}\{\psi\} \tag{2.63}$$

where we have set $G_{\mathrm{R}} = (EI_{\mathrm{R}} - H_{\mathrm{R}} + i0_{\mathrm{R}}^{+})^{-1}$ which is the Green's function of the isolated contact. Substituting Eq. (2.63) into Eq. (2.62) we can write

$$(EI - H)\{\psi\} - \tau G_{\mathrm{R}} \tau^{+} \{\psi\} = \tau \{\Phi_{\mathrm{R}}\} \tag{2.64}$$

and (c.f. Eqs. (2.54) and (2.55)) therefore write down a modified Schrödinger equation for the open system of

$$E\psi = (H + \Sigma)\psi + S \tag{2.65}$$

where we have set $\Sigma = \tau G_{\mathrm{R}} \tau^{+}$ which is the self-energy of the contact, and $S = \tau \Phi_{\mathrm{R}}$ which is a source term representing the flow of electrons from the contact to the channel. We have now constructed a more general open boundary Schrödinger equation with the same form as that seen in Eq. (2.55).

However, since G_{R} is the Green's function of the infinitely large contact (reservoir) it is therefore a huge (infinite) matrix. This problem can be solved by truncating it using the surface Green's function (see [94] and [96])

$$g_{\mathrm{surface}}(E) = [EI - \alpha - \tau_{\mathrm{L/R}} g_{\mathrm{surface}} \tau_{\mathrm{L/R}}^{\dagger}]^{-1} \tag{2.66}$$

where I is the identity matrix, α is the initial/final element of the Hamiltonian, and $\tau_{\mathrm{L/R}}$ is the first/last off-diagonal element of the channel Hamiltonian. Since the g_{surface} appears on both sides of this equation we must solve it self-consistently. The initial guess for the surface Green's function is taken to be $g_{surface} = [EI - \alpha]^{-1}$ and Eq. (2.66) is then solved iteratively using the Sancho-Rubio algorithm [104] until the quantity $\tau_{\mathrm{L/R}} g_{\mathrm{surface}} \tau_{\mathrm{L/R}}^{\dagger}$ varies by less than 10^{-6} eV (since this is significantly less than the magnitude of the energies relevant to our system). The surface Green's function can be seen as the effect of propagating the device wave function into the contacts (i.e. each iteration propagates the function to the next lattice point in the contact beginning with the initial/final element of the device Hamiltonian (i.e. our initial guess)), with this effect then folded into the device through the self-energies which now become

$$\Sigma_{\mathrm{L/R}} = \tau_{\mathrm{L/R}} g_{\mathrm{surface}} \tau_{\mathrm{L/R}}^{\dagger} \tag{2.67}$$

Note that the applied voltage appears indirectly in the contact self-energies through the initial/final element of the Hamiltonian, i.e. the applied voltage is added by hand on the onsite energies of the Hamiltonian (along with U) and then enters the contact self-energy through the surface Green's function.

2.5.4 The scattering self-energy

Finally we come to the last term needed for the Green's function, the scattering self-energy. This describes the electron-phonon interactions within the device and is made up of two parts; the in-scattering:

$$\Sigma_{\text{scatt}}^{\text{in}}(E) = D_0 G^n(E) \tag{2.68}$$

i.e all the electrons that flow *into* a particular energy *E*, and out-scattering:

$$\Sigma_{\text{scatt}}^{\text{out}}(E) = D_0 G^p(E) \tag{2.69}$$

i.e. all the electrons that flow *out of* a particular energy *E*.

In the above equations D_0 is the acoustic electron-phonon coupling strength similar to (but not the same as) the deformation potential. This is normally set by calibrating to a chosen mean-free-path as described in chapter 3, but a typical value is of the order of 10^{-3} eV^2. This approximation has been shown to be quantitatively valid for many systems [105], such as electrons in silicon [98], transport in carbon nanotubes [97], and many more, and captures all the essential transport features.

G_n and G_p are the electron density and the density of unoccupied states respectively:

$$G^n(E) = G\left(\Sigma_{\text{L}}^{\text{in}} + \Sigma_{\text{R}}^{\text{out}} + \Sigma_{\text{scatt}}^{\text{in}}\right)G^\dagger \tag{2.70}$$

$$G^p(E) = G\left(\Sigma_{\text{L}}^{\text{out}} + \Sigma_{\text{R}}^{\text{out}} + \Sigma_{\text{scatt}}^{\text{out}}\right)G^\dagger \tag{2.71}$$

where *G* is the retarded Green's function as defined in the following section, and $\Sigma_{\text{L/R}}^{\text{in}}$ and $\Sigma_{\text{L/R}}^{\text{out}}$ are the in-flow from filled contact states and out-flow from empty contact states of the left/right contacts respectively. To compute the filled/empty states we must know the distribution function of the contacts which we take to be the Fermi-Dirac distribution (Eq. (2.7)) with the relevant Fermi level, i.e. although the channel itself is not in equilibrium we consider each contact to be in equilibrium, although of course not with each other - in fact the difference in Fermi level of the two contacts must be equal to any voltage difference added on to the Hamiltonian through the "built-in" potential *U* in order to obey electrostatics. The in-flow/out-flow energies for each contact are then

$$\Sigma_{\text{L/R}}^{\text{in}} = \Gamma_{\text{L/R}} f(E - E_{\text{F}}^{\text{L/R}}) = i(\Sigma_{\text{L/R}} - \Sigma_{\text{L/R}}^\dagger) f(E - E_{\text{F}}^{\text{L/R}}) \tag{2.72}$$

$$\Sigma_{\mathrm{L/R}}^{out} = \Gamma_{\mathrm{L/R}}[1 - f(E - E_{\mathrm{F}}^{\mathrm{L/R}})] = i(\Sigma_{\mathrm{L/R}} - \Sigma_{\mathrm{L/R}}^{\dagger})[1 - f(E - E_{\mathrm{F}}^{\mathrm{L/R}})] \quad (2.73)$$

where we have defined the broadening

$$\Gamma_{\mathrm{L/R}} = i(\Sigma_{\mathrm{L/R}} - \Sigma_{\mathrm{L/R}}^{\dagger}) = \Sigma^{\mathrm{in}} + \Sigma^{\mathrm{out}} \quad (2.74)$$

which can physically related to the broadening of the density of states in the channel **[Datta05]**.

Like G, G_{n} and G_{p} are tridiagonal matrices where the diagonal elements can be seen as the electron densities and the off-diagonal elements as the current densities (c.f. the Hamiltonian where we have the onsite energies and hopping parameters respectively).

Finally we form the total scattering rate that we need to form the Green's function:

$$\Sigma_{\mathrm{S}}(E) = -\frac{i}{2}[\Sigma_{\mathrm{scatt}}^{\mathrm{in}}(E) + \Sigma_{\mathrm{scatt}}^{\mathrm{out}}(E)] = -\frac{i}{2}\Gamma_{\mathrm{scatt}}(E) \quad (2.75)$$

The expression above is the imaginary part of the total scattering self-energy which is responsible for the scattering rate. The real part is typically ignored as it only brings about a small shift in the eigenvalues.

2.5.5 The Green's function

We have now constructed our discretized Hamiltonian, the contact self-energies, and the scattering self-energy. The retarded Green's function of the device is then given by

$$G(E) = [(E + i0_{\mathrm{D}}^{+})I - H - \Sigma(E)]^{-1} \quad (2.76)$$

where 0_{D}^{+} is an infinitesimally small positive number which pushes the poles of G to the lower half plane in complex energy. This has the effect of making the Green's function causal in the time domain [95]. A typical value for this quantity in a simulation is $0_{\mathrm{D}}^{+} \approx 10^{-12}$. I is the identity matrix, and Σ(E) is the sum of the self-energies

$$\Sigma(E) = \Sigma_{\mathrm{L}}(E) + \Sigma_{\mathrm{R}}(E) + \Sigma_{\mathrm{S}}(E) \quad (2.77)$$

Note the interdependencies at play here: the Green's function, G, depends on the scattering self-energy, Σ_{S}, which depends on the densities G_{n} and G_{p}, which then depend on both Σ_{S} and G (see Fig. 2.8a). Consequently, this system of equations must

be solved self-consistently (see Fig. 2.8b). For our 'initial guess' we take the ballistic Green's function which can be calculated without self-consistency. The convergence criteria for the ensuing self-consistent calculation is chosen to be current conservation, i.e. we consider convergence is achieved when the current is conserved along the length of the channel to within 1%. The current from site to site within the channel is calculated as

$$I_{j\to j+1} = \frac{ie}{\hbar}\int_{-\infty}^{+\infty}\frac{dE}{2\pi}\left[H_{j,j+1}G^{n}_{j+1,j}(E) - H_{j+1,j}G^{n}_{j,j+1}(E)\right] \tag{2.78}$$

Although we do not present a derivation for this equation (which requires also a discussion on the spectral functions – even though ultimately they do not enter the final implementation of the formalism (see Ref. [94])), the form of this equation can be seen intuitively as the easiness of transport from one site to the next ($H_{j,j+1}$ is an off-diagonal element of the Hamiltonian, i.e. the hopping parameter, t) times the current density between those sites $G^{n}_{j,j+1}$, minus 'easiness times current density' in the opposite direction (i.e. we have the net flow of two electron fluxes).

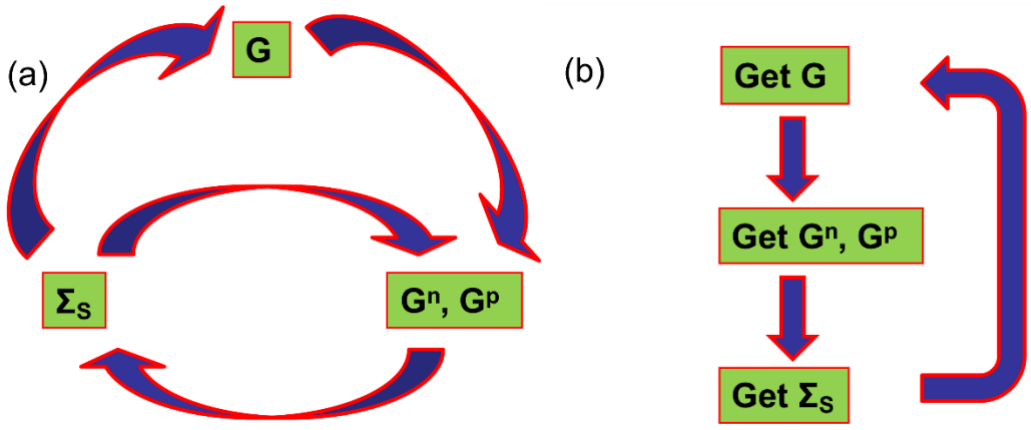

Fig. 2.8: (a) The interdependencies of the various elements involved in the formalism (b) The computational scheme for the self-consistent calculation.

2.5.6 Transport features

In the ballistic case ($\Sigma_S = 0$) we can define the transmission of the system as:

$$T(E) = \mathrm{Trace}(\Gamma_L G \Gamma_R G^{\dagger}) \tag{2.79}$$

where $\Gamma = i(\Sigma - \Sigma^{\dagger})$ is the broadening as seen in Eq. (2.74). The current through the device can then simply be calculated using the Landauer formalism (see Eq. (2.6)). Note that in this case the Fermi distributions of the contacts do not enter the Green's function formalism itself and are only added after-the-fact through the Landauer calculation of the current (the transmission is not a Fermi level dependent property, telling us only the probability of an electron with a particular energy traversing the channel and not how many electrons actually occupy those states). In the non-coherent (phonon-limited) case, however, the Fermi levels of the contacts enter in to the formalism through the in-flow and out-flow energies of the two contacts (see Eqs. (2.72) and (2.73)).

It is also possible to define an effective transmission for the phonon-limited case as:

$$T(E) = \frac{h}{2e^2} \frac{I(E)}{f_1(E) - f_2(E)} \tag{2.80}$$

In Fig. 2.9a we show the transmission function of a pristine channel of length L = 60 nm and width W = 30 nm under two different conditions: i) coherent (ballistic) transport (blue line), and ii) incoherent transport (red line), The ballistic transmission of the pristine channel shows the usual staircase shape, with an increment every time a new subband is reached in energy. Those features are removed when phonon scattering is included. In Fig. 2.9b we also show the local density of states (LDOS) at the first node in the channel. It can be seen that each new subband contributes a 1D DOS but that collectively they combine to form a DOS approaching that of a 2D system like the one we simulate (cf. Fig. 2.2).

The power factor, GS^2, is obtained using the expression:

$$I = G\Delta V + SG\Delta T \tag{2.81}$$

For each value of the power factor, the simulation is run twice, initially with a small potential difference and no temperature difference (ΔT=0), which yields the conductance ($G=I_{(\Delta T=0)}/\Delta V$), then again with a small temperature difference and no potential difference (ΔV=0), which yields the Seebeck coefficient ($S=I_{(\Delta V=0)}/G\Delta T$). This method is validated in Ref. [106].

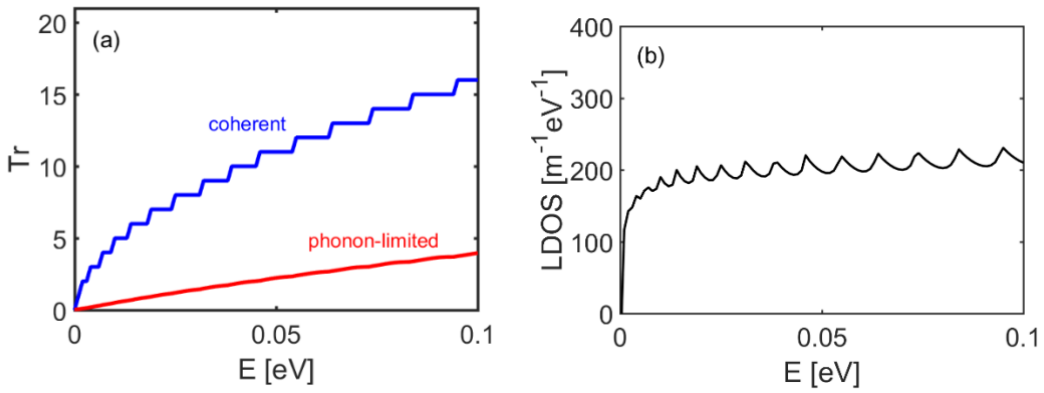

Fig. 2.9: (a) A comparison of the transmissions for an empty channel under ballistic coherent conditions (blue line) and an empty channel under phonon scattering transport conditions (red line). (b) The local density of states versus energy of an empty channel of dimensions length L = 60 nm and width W = 30 nm.

2.6 Comparison of methods

Finally, we would like to comment on the relationship between the Boltzmann transport formalism and the NEGF method and their differing uses. The Boltzmann transport formalism as implemented here is based on a classical view of transport (being derived from the Boltzmann transport equation). As such it is not able to capture important nanostructure details such as geometry, the scattering of electrons from nanoinclusions (beyond relaxation time approximations such as in Ref. [107]) and quantum effects such as resonances and tunnelling. It is, however, suited to simulating single-phase bulk materials where the electron scattering processes can be described accurately by the relaxation time approximation (such as for acoustic (elastic) phonon scattering and ionized impurity scattering). For multi-phase disordered materials, however, it is necessary to use a fully quantum mechanical formalism such as NEGF in order to capture the details mentioned above, although this comes with a computational cost, limiting the structures we study in this thesis to two dimensions and sizes of just tens of nanometers. An in-depth discussion of the conceptual similarities and differences between the Boltzmann and NEGF formalisms can be found in chapter 8 of Ref. [95].

III. Thermoelectric power factor of nanocomposite materials from two-dimensional quantum transport simulations

3.1 Introduction

As discussed in chapter 1, nanoinclusions have are a widely employed method for the reduction of the thermal conductivity in thermoelectric materials. While this impact of nanoinclusions on the thermal conductivity is well documented [30], [108], previous works are not as clear on their impact on the power factor, with results varying significantly, from only small influence [40], [41], [43], [109], to large potential improvements [44], [50], [51], [110]. Thus, it is imperative that a high level of understanding on the influence of nanoinclusions on the power factor, both qualitative and quantitative is also established, if *ZT* is to be maximized. However, the complexity of the electronic transport, combining semiclassical effects, quantum effects, ballistic and diffusive regimes, as well as the geometry details, makes accurate modelling a difficult task. Several works in the literature use semi-classical models, simplified geometries, and various approximations to provide understanding of transport in such systems [38], [107], [109], [110].

In this chapter we show how the non-equilibrium Green's function (NEGF) simulation method can be employed to calculate the electron transport properties in 2D nanostructures in a fully quantum mechanical way that includes the details of geometry, electron-phonon interactions, quantization, tunnelling, and the ballistic to diffusive nature of transport, all combined in a unified simulation approach. Such simulations are very demanding, thus, for computational effectiveness we consider 30 nm × 60 nm 2D nanoribbon channels embedded with nanoinclusions in a regular hexagonal configuration. These short channels are, however, large enough to capture all essential transport physics as we will explain. We present a detailed study of the influence of nanoinclusions on the *PF* of nanocomposite materials. We show that, unfortunately, the presence of potential barriers originating from nanoinclusions within a matrix material offers opportunities for only moderate power factor improvements, resulting from their inability to act as effective energy filters, a behaviour very different than that of superlattice structures. We describe, however, how such nanocomposites can be optimized to limit *PF* degradation and even achieve

mild improvements. We show that the key design elements for this *PF* resilience is to begin with a degenerately doped matrix material in which the Fermi level is placed 1-2k_BT into the bands, and then insert nanoinclusions of barrier heights between the Fermi level and conduction band edge. This introduces a small filtering effect which improves the Seebeck coefficient and is more effective when the nanoinclusions are large enough to prevent quantum tunnelling. Importantly, we also show that under these conditions, the power factor is independent of the density of nanoinclusions, even slightly benefiting at higher densities (where strong reduction in κ is also anticipated). This provides opportunities for dense nanoparticle materials with low κ and still acceptable *PF*s, thus high *ZT* figures of merit.

At this point we would like to discuss the experimental interpretation of the variables that we consider. The height of the nanoinclusion barriers can be controlled experimentally by the choice of band offset between the matrix material and the nanoinclusion material, and often further fine-tuned through alloying of either material. The Fermi level is controlled by the level of doping, and the spatial placement of this doping can further effect the potential profile of the channel as discussed later (see Fig. 3.9). Other parameters considered such as the effective mass and the mean-free-path are specific to the material choice although can also sometimes be engineered through e.g. alloying.

Thus, the goal of this chapter is to illuminate aspects of the thermoelectric power factor in nanostructures for which several contradicting reports are encountered in the literature. The chapter is organized as follows: In Section 3.2 we describe our NEGF approach including our calibration procedure and indicate the geometries we study. In Section 3.3 we present our results. In Section 3.4 we discuss the results, and in Section 3.5 we conclude.

3.2 Approach

To compute the electronic transport, we employ the 2D quantum transport simulator based on the non-equilibrium Green's function (NEGF) formalism including electron-acoustic phonon scattering in the self-consistent Born approximation as described in chapter 2. This approach is highly suitable since it can capture all relevant quantum effects such as quantization, energy mixing, interferences, and tunnelling, as

well as all geometrical complexities, which can be important in transport through disordered materials.

The system is treated as a 2D channel within the effective mass approximation, where we use a uniform $m^* = m_0$ in the entire channel, where m_0 is the rest mass of the electron. The nanoinclusions are modeled as potential barriers of cylindrical shape within the matrix material as shown in the schematic of Fig. 3.1c. We consider regular hexagonal placement of the nanoinclusions, but in the discussion section we elaborate on the possible effects of their random placement based on our findings.

The sharp features of the system required a large number (~100) of convergence steps. Figure 3.1c shows a typical band diagram of the nanocomposite under consideration. The Fermi level is denoted by the dashed-red line. Current flows through the nanoinclusion barriers and over them.

3.2.2 Channel calibration

Previous theoretical and experimental works [33], [34], [61], [111], [112] have shown degenerately doped materials, once nanostructured to improve filtering, could provide significant power factor increases. Placing the Fermi level well into the bands improves conductivity, which compensates for the reduction that is caused by nanostructuring. Thus, in this work as well, as a starting point, we place the Fermi level high into the bands at $2k_BT$ above the conduction band edge. We assume room temperature T = 300 K throughout the chapter. The value of D_0 is then chosen such that the conductance of an L = 15 nm long pristine channel is found to be 50% of the ballistic value. This effectively amounts to fixing a mean-free-path of 15 nm for the system; a value that is comparable to common semiconductors such as silicon [56], [113], [114]. The appropriate D_0 was found to be $D_0 = 0.0026$ eV^2 as shown in Fig. 3.1a. Thus, with such a mean-free-path, the L = 60 nm channel length we consider is large enough to result in diffusive transport in the material we simulate, although in the discussion section we also elaborate on the features of ballistic transport. The conduction band is set at $E_C = 0.00$ eV and the Fermi level, unless otherwise stated, is placed at $E_F = 0.05$ eV. It should be noted that the chosen value of D_0 only produces a mean-free-path (as defined here) of exactly 15 nm when $E_F = 0.05$ eV as this is the Fermi level used during the calibration. As the Fermi level moves, the average energy of the electrons changes and consequently so does the mean-free-path, deviating

somewhat linearly as the E_F changes. We can then extract the power factor as shown in Fig. 3.1b versus the reduced Fermi level η_F, i.e. the position of the Fermi level with respect to the band edge, $\eta_F = (E_F - E_C)/k_BT$. As expected, the maximum power factor is observed when the Fermi level is in the vicinity of the band edge [90].

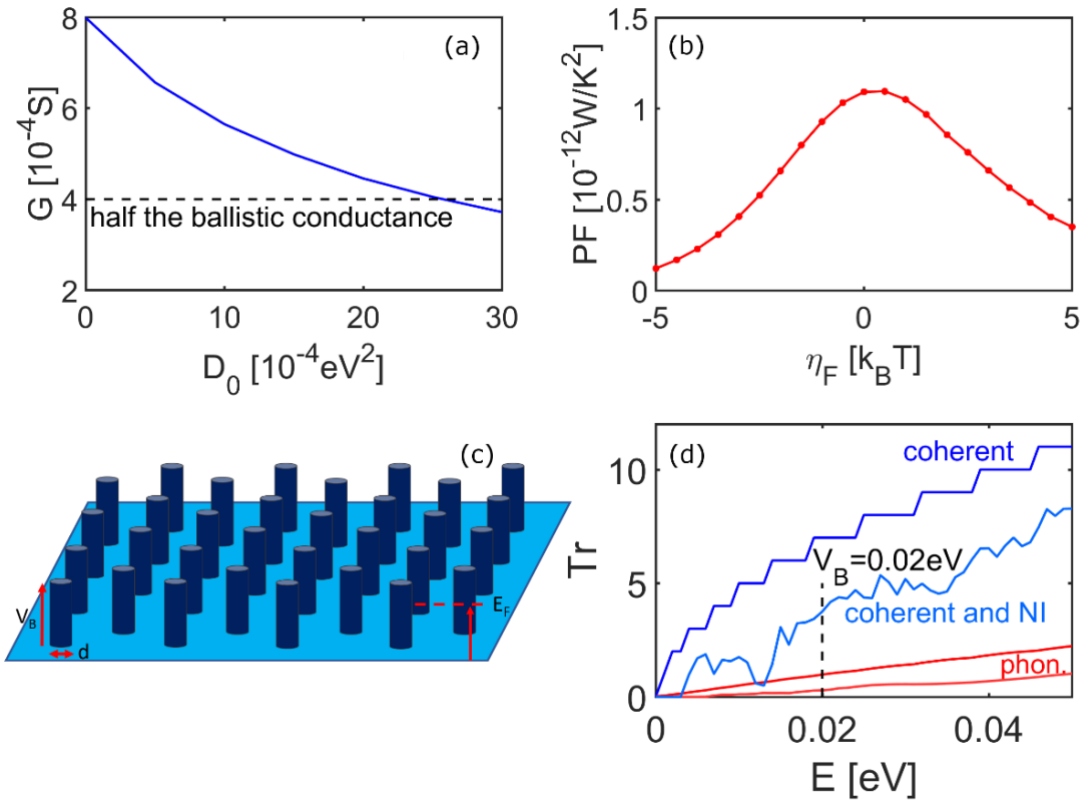

Fig. 3.1: (a) Calibration of the simulations' scattering parameters. The scattering strength is increased in an L = 15 nm channel until the conductance falls to half of the ballistic value (dashed-black line), thereby setting the mean-free-path of the electrons to 15 nm. (b) The power factor (defined as GS^2) of a pristine (without nanoinclusions) channel as the Fermi level is scanned across the bands. (c) A schematic of a typical geometry we consider. V_B is the barrier height, d the nanoinclusion diameter, and E_F the Fermi level. (d) A comparison of the transmissions for an empty channel under ballistic coherent conditions (blue line), a channel with nanoinclusions under coherent transport (light-blue line), an empty channel under phonon scattering transport conditions (red line), and a channel with nanoinclusions under phonon scattering transport conditions (light-red line).

With regards to the transport properties, in Fig. 3.1d we show the transmission function of the nanocomposite channel under four different conditions: i) coherent

(ballistic) transport for a pristine channel (blue 'staircase' line), ii) coherent transport for a channel with nanoinclusions (light-blue line), iii) incoherent transport for a pristine channel (red line), and iv) incoherent transport for a channel with nanoinclusions (light-red line). The barrier height of the nanoinclusions is set to V_B = 0.02 eV and the Fermi level at E_F = 0.05 eV. The ballistic transmission of the pristine channel shows the usual staircase shape, with an increment every time a new subband is reached in energy. A large drop is observed when the nanoinclusions are added in the geometry, where resonance features are also evident. Those features are removed when phonon scattering is included, and the transmission is reduced even more when nanoinclusions are added in addition to phonon scattering.

An interesting feature from these results is the fact that the transmission suffers significantly once the nanoinclusions are added, even at energies much higher than the barrier height, and we elaborate on this more in the Discussion Section 3.4. This is in contrast to a common approximation that energies above the barrier are not severely affected and are considered to be restored to their pristine material value. The transmission in this case is dominated by the regions of high resistance, which are the nanoinclusions. In the nanoinclusion regions, the bands that contribute to transmission begin just above V_B, i.e. it is as if the ballistic transmission is shifted downwards by the number of bands it has at V_B. Since in 2D there are numerous numbers of subbands at lower energies, the reduction in the transmission is strong, and it is not recovered even at energies much higher that V_B.

3.3 Results

Once the calibration is completed we proceed to consider geometries which include circular nanoinclusions (NIs) of different barrier heights, V_B, different NI densities, and different NI diameters. The channel width was kept at W = 30 nm, and the length at L = 60 nm in all cases.

3.3.1 Influence of barrier height V_B and Fermi level position E_F

The first investigation we perform is on the influences of: i) the nanoinclusion barrier height V_B, and ii) the Fermi level, E_F, on the thermoelectric coefficients, conductance G, Seebeck coefficient S, and power factor GS^2. Transport in an 8×4 hexagonal array of nanoinclusions of diameter d = 3 nm (as indicated in the inset of

Fig. 3.2c) is simulated at five different Fermi levels, E_F = -0.025 eV (purple lines), E_F = 0 eV (green lines), E_F = 0.025 eV (black lines), E_F = 0.05 eV (red lines), and E_F = 0.075 eV (blue lines). For each Fermi level, we vary the nanoinclusion barrier height from V_B = 0 eV to V_B = 0.2 eV in steps of 0.02 eV. These are similar band offset values that one encounters in promising thermoelectric materials, for example, PbSe/CdSe with a valence band offset of 0.06 eV, PbSe/ZnSe with a valence band offset of 0.13 eV, and PbS/CdS with a valence band offset of again 0.13 eV [53]. The comprehensive results are shown in Fig. 3.2a, 3.2b, and 3.2c for the conductance G, the Seebeck coefficient S, and the power factor GS^2, respectively. As can be observed in Fig. 3.2a, the conductance G shows the expected decrease at all Fermi levels as V_B is increased, due to the potential barriers blocking the electron flow. For higher barriers G saturates, with the saturation being observed more evidently ~$2k_BT$ above the Fermi level, i.e. the saturation tends to shift to the right with increasing E_F. Increasing the Fermi level increases the conductance as well, since higher velocity states are increasingly occupied. Naturally, as the Fermi level increases, the Seebeck coefficient in Fig. 3.2b drops almost linearly (comparing the different lines in Fig. 3.2b) following the usual reverse trend compared to G. The Seebeck coefficient is proportional to the average energy of the current flow with respect to the Fermi level, $S \propto \langle E - E_F \rangle$ which is reduced as the Fermi level is raised until degenerate conditions are reached. At each individual constant Fermi level line, the Seebeck coefficient only slightly increases with V_B, a sign of weak energy filtering, before it saturates as also observed in the case of G.

The corresponding power factors are shown in Fig. 3.2c. Comparing the lines that correspond to the various Fermi levels, a large variation in the power factor is observed in the left of Fig. 3.2c, for small nanoinclusion barrier heights. As V_B increases, the power factors follow a declining trend and finally all lines saturate at a lower value compared to the pristine material power factors. One important observation that can be detected from Fig. 3.2c is that the highest power factor is observed for the channel where the Fermi level is placed around the conduction band edge, or somewhat higher (green and black lines, E_F = 0 eV, 0.025 eV), but more importantly when the band edges of the matrix and the nanoinclusions are aligned (i.e. V_B = 0 eV). This clearly shows that in principle the introduction of energy filtering

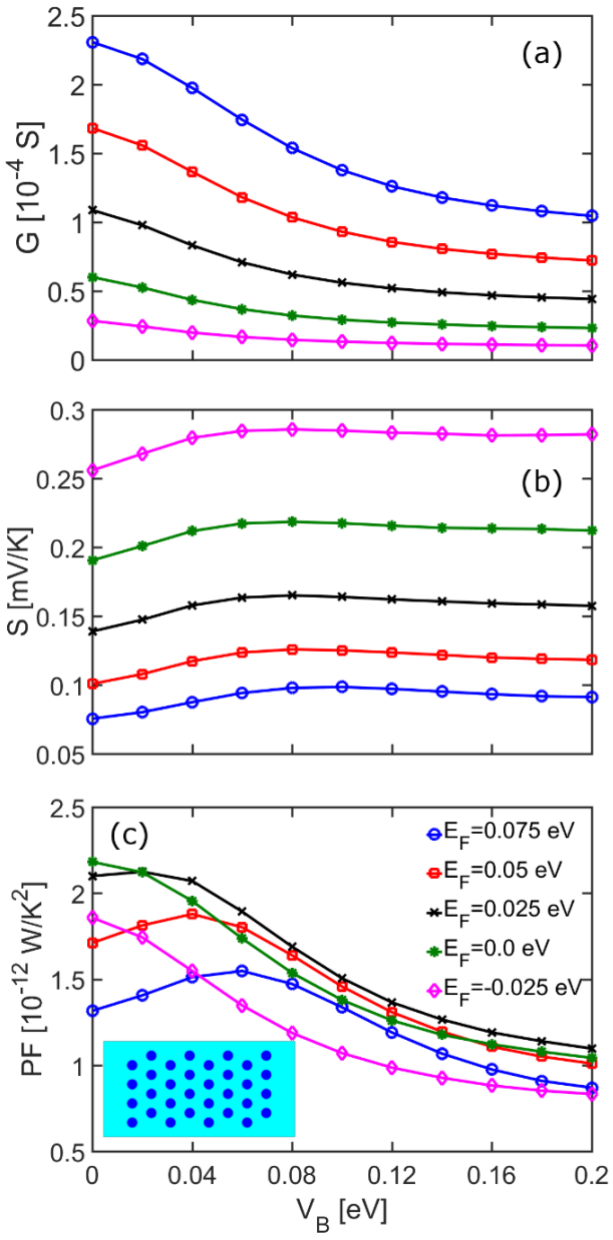

Fig. 3.2: The thermoelectric coefficients of an L = 60 nm channel with an 8×4 hexagonal arrangement of nanoinclusions (inset of (c)) and acoustic phonon scattering transport conditions versus nanoinclusion barrier height, V_B. (a) The conductance. (b) The Seebeck coefficient. (c) The power factor defined as GS^2. Five different Fermi levels are considered: E_F = -0.025 eV (purple-diamond lines), E_F = 0 eV (green-star lines), E_F = 0.025 eV (black-cross lines), E_F = 0.05 eV (red-square lines), and E_F = 0.075 eV (blue-circle lines).

potential barriers by the use of nanoinclusions *cannot* increase the power factor. This is of course if one considers a material with an optimized Fermi level position at $E_F \sim E_C$ to begin with, which is rarely the case in practice. If one considers, however, that the position of the Fermi level is in general not at the optimal point, then there is a possibility of moderate power factor improvements of the order of ~10% (red, blue lines). The power factor lines in Fig. 3.2c for $E_F > E_C$ indicate that as the barrier heights V_B of the nanoinclusions increase, a maximum is reached when V_B is approximately E_F, producing a 5-10% increase in the power factors. Raising V_B even further takes away this increase and forces the power factor to saturate at a lower level (to around 50% of the initial *PF*). This requirement for small band offsets to retain high conductivity has previously been identified in Refs. [53], [81], [115], [116] but its effect on the power factor had not yet been quantified.

3.3.2 Influence of the nanoinclusion density

The next investigation we perform is to illustrate the influence of the NI density on the thermoelectric coefficients. Fig. 3.3 shows the thermoelectric coefficients *G, S* and *PF*, again versus nanoinclusion barrier height V_B for four different geometries of increasing density as shown in the insets of Fig. 3.3c. These four simulated geometries are: a 2×4 array (green lines), a 4×4 array (black lines), a 6×4 array (blue lines), and an 8×4 array (red lines). The Fermi level is again placed at $E_F = 0.05$ eV (dashed-red line in Fig. 3.3c). Fig. 3.3a shows that, as before, the conductance *G* falls as V_B increases, and, as expected, *G* also falls as the number of nanoinclusions in the channel is increased. Likewise, as the number of nanoinclusions increases, the effect of energy filtering is increased and an improvement in *S* is observed. The increase is of the order of 10% for the 2×4 channel, and is increased to approximately 25% for the 8×4 channel as seen in Fig. 3.3b. As V_B increases, we initially see a linear rise in *S*. At barrier heights V_B, just above the Fermi level, *S* peaks. For larger V_B it decreases slowly before saturating for barrier heights much above the Fermi level. It is interesting observe that in this region, both *G* and *S* are simultaneously decreasing, a counterintuitive effect – we provide an explanation for this later. Fig. 3.3c shows the result of these features on the power factor. From zero barrier heights up until $V_B \sim E_F$, a small increase in the power factors is observed, with a maximum of the order of 10% for the 8×4 channel

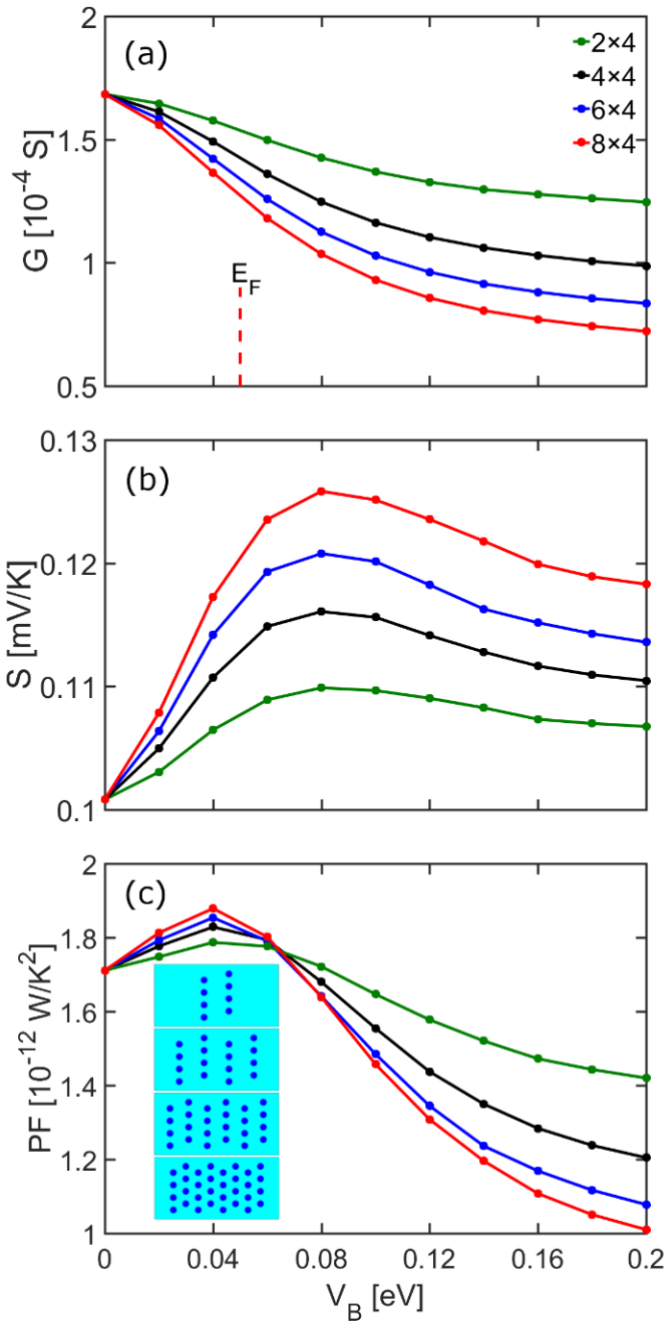

Fig. 3.3: The thermoelectric coefficients of an L = 60 nm channel with E_F = 0.05 eV (dashed-red line) and acoustic phonon scattering transport conditions versus nanoinclusion barrier height, V_B. (a) The conductance. (b) The Seebeck coefficient. (c) The power factor defined as GS^2. Hexagonal arrays of four different nanoinclusion densities are considered as shown in the inset of (c): 2×4 array (green lines), 4×4 array (black lines), 6×4 array (blue lines), and 8×4 array (red lines).

(red line). As V_B increases even further, the power factor then falls to values below the pristine channel value for all channels. Although for small barrier heights of $V_B < E_F$ the density has little effect on the power factor, the fact that the *PF* increases, and is even independent of NI density, is quite important. It indicates that the density of nanostructured materials with nanoinclusions can be optimized for maximal reduction in the thermal conductivity, fine-tuning the distances between the nanoinclusions in order to be of the length scale of the phonon mean-free-path without causing any adverse effects on the power factor. At higher V_B, on the other hand, the detrimental effect of density is more important, with the decrease from pristine material power factor ranging from 17% for the 2×4 array to 40% for the 8×4 array as the barrier height is increased to $V_B = 0.2$ eV.

The results in Fig. 3.2 and Fig. 3.3, indicate that although the possibility of using nanocomposites with nanoinclusions embedded within a matrix material to improve the power factor is limited, importantly, neither will the careful use of such nanoinclusions limit the power factor significantly. The main reason for using such nanostructures is to provide *ZT* improvements by reducing the thermal conductivity of the material, and the results of Fig. 3.2 and Fig. 3.3 show that such structures can provide resilience to the power factor, as well as showing the possibility of slight benefits. Note here that in our simulations we only consider acoustic phonon scattering. The presence of impurity scattering as well as variation in the thermal conductivities of the different regions can also improve the Seebeck coefficient even further as explained in Refs. [33], [106], [112], which might allow for higher power factors compared to what we compute here.

3.3.4 The simultaneous decrease in *G* and *S*

A non-intuitive point to elucidate here, is the simultaneous drop in both *G* and *S* as the barrier height V_B of the nanoinclusions is increased. What is non-intuitive is that in general these two quantities follow a reverse trend, i.e. as *G* is decreased at the presence of large V_B, we would have expected *S* to increase. The fact that both quantities drop causes a large degradation to the power factor, and limits the filtering capabilities of such nanocomposites. To understand this simultaneous decrease we must consider what happens to the average energy of the current flow as V_B increases, since this determines the Seebeck coefficient $S \propto \langle E - E_F \rangle$ [106]. The x-axis of Fig.

3.4 shows the distribution of the energy of the current flow, $E \times I(E)$, with the average marked with a star, for six different barrier heights, V_B = 0 eV (black line), V_B = 0.04 eV (red line), V_B = 0.08 eV (blue line), V_B = 0.12 eV (green line), V_B = 0.16 eV (purple line), V_B = 0.2 eV (brown line). The inset of Fig. 3.4 zooms around the average energy of the current flow. As V_B is initially raised, some of the lower energy electrons are cut off while higher energy electrons are less affected, raising the average energy of the current, and thus, raising the Seebeck coefficient (see from black, to red, to blue lines in the inset of Fig. 3.4). This behaviour continues until V_B is approximately k_BT above E_F, i.e. $V_B < E_F + k_BT$. It is important to note that electrons with energies less than the barrier height can still contribute to the current by flowing around the nanoinclusion barriers (which is a different scenario compared to superlattice structures which are commonly employed for thermoelectric energy filtering). Thus, as V_B continues to increase, lower energy electrons continue to flow around the

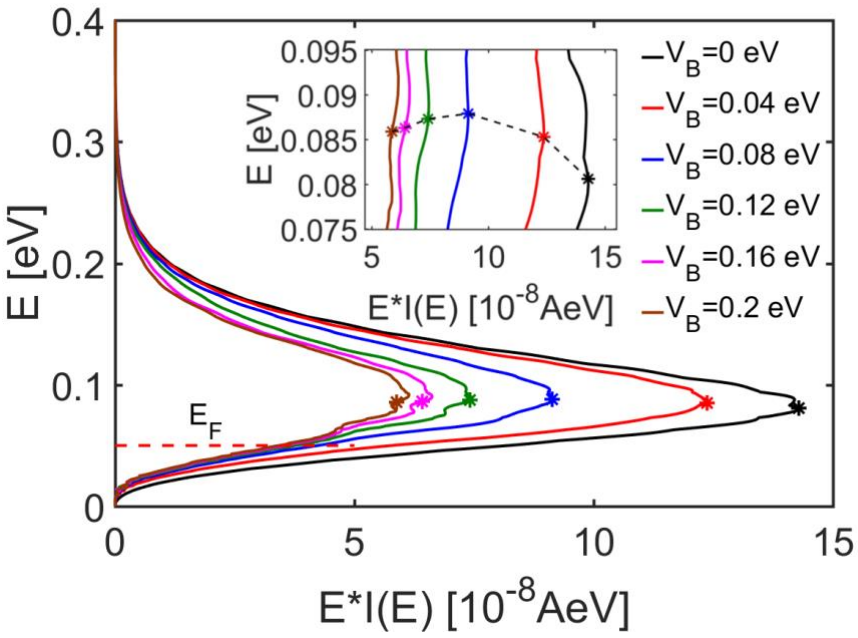

Fig. 3.4: The distribution of the energy of the current flow for an L = 60 nm channel with an 8×4 array of nanoinclusions and E_F = 0.05 eV. The stars denote the average energy of the current flow. A zoomed version of these is shown in the inset. Six different nanoinclusion barrier heights are shown: V_B = 0 eV (black), V_B = 0.04 eV (red), V_B = 0.08 eV (blue), V_B = 0.12 eV (green), V_B = 0.2 eV (purple), and V_B = 0.1 eV (brown). The dotted line in the inset indicates from right to left the trend of increase in V_B.

barriers and so their contribution is hardly affected because the change in the barrier affects only much larger energies. Higher energy electrons, however, are then begun to be cut off and the average energy begins to fall again (see from blue, to green, to purple, to brown line in the inset of Fig. 3.4), as does the Seebeck coefficient. Eventually, V_B is high enough that it affects all energies similarly, and the majority of the current flows around the nanoinclusions. Therefore, additional increases in V_B have little effect, and the Seebeck coefficient saturates.

3.3.4 Influence of quantum tunnelling

An important effect that needs to be considered in evaluating the influence of nanoinclusions on the power factor of nanocomposites is quantum mechanical tunnelling. In prior works related to the effect of tunnelling in superlattices, we have shown that tunnelling is detrimental to the Seebeck coefficient as it makes potential barriers transparent and takes away any benefits that energy filtering could provide to the power factor [101], [102]. We have shown that in the case of superlattices tunnelling becomes important when the thicknesses of the barriers drop below 1-2 nm (for channels with effective mass $m^* = m_0$). Here, we compare the case of nanoinclusions of small diameters $d \sim 1$ nm which would be strongly influenced by tunnelling, versus the case of structures with larger diameters $d \sim 3$ nm, which we expect not to be influenced by tunnelling to such a degree. Figure 3.5 shows the effect of nanoinclusion diameter on the thermoelectric coefficients G, S and PF for the d = 1.5 nm nanoinclusions (red lines, S1) and d = 3 nm nanoinclusions (black lines, S2) for the geometry with 8×4 nanoinclusion arrays (first two insets of Fig. 3.5c). As before, G falls with increasing V_B in both diameter cases, but the fall is more marked for nanoinclusions of larger diameters, which hinder transport more (Fig. 3.5a). The smaller diameter nanoinclusions not only occupy less space that obscures transport, but quantum tunnelling causes them to become semi-transparent and allow some current to flow through them. Likewise, due to their transparent nature they do not cause large changes in the Seebeck coefficient as shown by the red line in Fig. 3.5b (only a ~5% increase is observed at high V_B), thus, only a weak energy filtering effect is observed. Consequently, the power factor results in Fig. 3.5c for the d = 1.5 nm nanoinclusions do not show any beneficial effect on the power factor for any of the barrier heights. The beneficial effects of energy filtering are only seen for the larger

diameter of d = 3 nm, although, as explained earlier, this only appears to occur up to a barrier height approximately halfway between E_C and E_F. Beyond this V_B, the degradation in G outweighs the gains in S, and the power factor falls even further below than that of the NIs with diameter d = 1.5 nm. These results demonstrate that, as with superlattices [101], [102], quantum tunnelling has a detrimental impact on the energy filtering effect and, thus, on any potential Seebeck coefficient improvements. To prevent this, diameters of d > 3 nm should be used to obtain power factor enhancements (the diameters of course need to be adjusted according to the effective mass of the carriers in the specific material under consideration).

3.3.5 Influence of nanoinclusion diameter

In order to further understand the influence of tunnelling versus density of nanoinclusions, in Fig. 3.5 we also plot the situation where we keep the areal density of nanoinclusions the same as that of the d = 3 nm 8×4 array channel (S2), using a lot more nanoinclusions of diameter d = 1.5 nm as shown in the third inset of Fig. 3.5c. Now we have a 15×7 array channel (S3) where the total area of included material is approximately the same across the two structures. The thermoelectric coefficients for this case are shown in Fig. 3.5 by the blue lines. Quite interestingly, this channel behaves very close to the d = 3 nm 8×4 array channel, indicating that at first order one can consider that the overall areal density of nanoinclusions has a stronger impact in determining the thermoelectric performance, compared to the actual size and their distribution. Although the d = 1.5nm nanoinclusions will still be semi-transparent, in this case they are many, and are placed in close proximity, in distances smaller than the carriers' relaxation length. This introduces quantum reflections and interferences, which introduce a larger resistance (lower G) and increase the energy filtering effect (higher S). However, if one looks at the PF results of Fig. 3.5c (blue line), it can be seen that such a channel is the worst of both previously examined channel cases, with no noticeable power factor improvement for low V_B (in contrast to what is shown by the black line), and large PF degradation at high V_B (even stronger than what is shown by the black line). Thus, an important recommendation at this point, is that nanoinclusions with low barrier heights and larger diameters are preferable for power factor resilience.

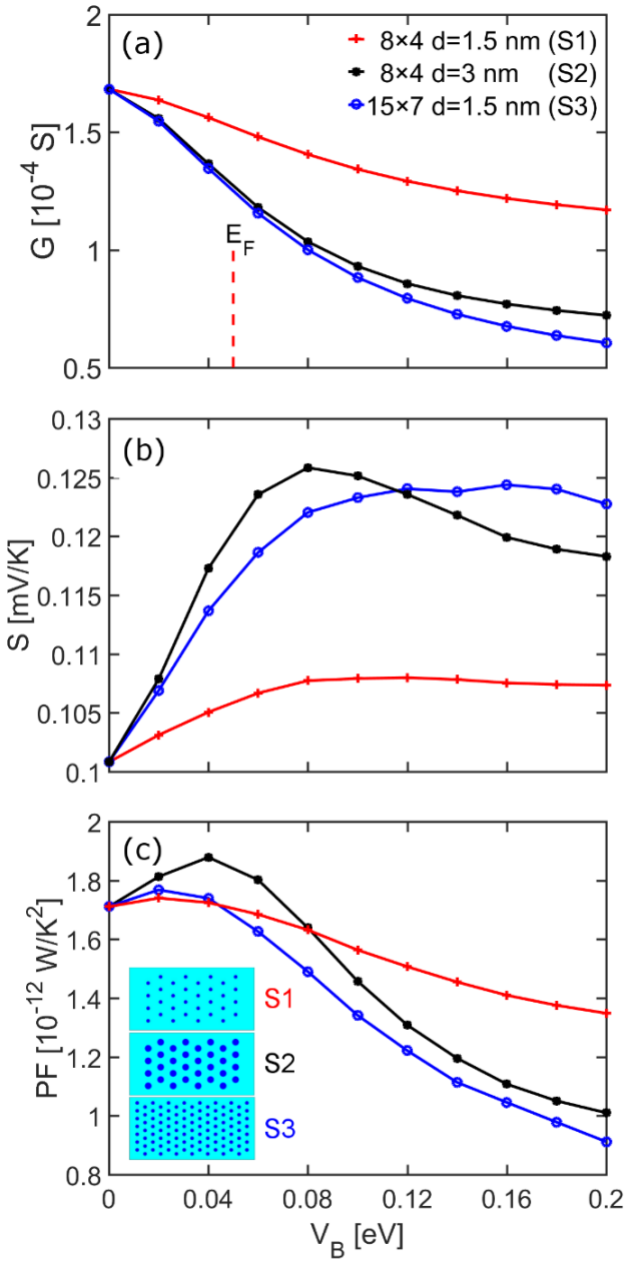

Fig. 3.5: The thermoelectric coefficients of L = 60 nm channels (insets of (c)) with 8×4 array of nanoinclusions versus nanoinclusion barrier height, V_B, for two different nanoinclusion diameters: d = 1.5 nm (red lines) and d = 3 nm (black lines), and a 15×7 array with d = 1.5 nm (blue lines) whose density is equivalent to the 8×4 array with d = 3 nm. (a) The conductance. (b) The Seebeck coefficient. (c) The power factor defined as GS^2.

3.4 Discussion

3.4.1 Features of the electron flow

To better understand the electronic transport and transmission (as previously shown in Fig. 3.1d) through the structures we consider, we show in Fig. 3.6a a colour plot of the component of the current flow along the length of the structure. Results are taken from the d = 3 nm 8×4 channel with V_B = 0.04 eV and E_F = 0.05 eV. The blue regions indicate the nanoinclusions (where through them the current is low), whereas the yellow regions indicate the matrix material (where the current is high). Note that this spatially varying current is still conserved in the transport direction at all energies independently, i.e. if we integrate along the width direction at every point along the length we get the same value. In Fig. 3.6b we show a cross-section of the L-directed current through two of the nanoinclusions (shown by the dashed-black line in Fig. 3.6a) at four different energies: E = 0.01 eV (below the V_B, green line), E = 0.02 eV (at the V_B, black line), E = 0.05 eV (at the E_F, blue line), E = 0.075 eV (above the E_F, purple line). From Fig. 3.6a it can be seen that the current is reduced where the nanoinclusions are situated (blue areas), but the area affected by the nanoinclusions is not quite the same as the nanoinclusion itself. Due to quantum tunnelling, the sides of the nanoinclusion are semi-transparent, narrowing the affected area, while in the direction of current flow, the affected area is elongated due to reflections off the nanoinclusion face. This can also be seen in Fig. 3.6b where there is a dip in the current at the position of the nanoinclusion and beyond. Crucially, this occurs at all energies where current is still flowing, showing that electrons with energies much higher than V_B are still significantly affected as they pass over the barrier. More detail on this is given in Fig. 3.6c where we plot the current as it varies in energy at two different points in the channel: i) at the centre of one of the nanoinclusions (blue line, position shown by the dotted-blue line in Fig. 3.6b), and ii) in the pristine matrix material (black line, position shown by the dotted-black line in Fig. 3.6b). The barrier height is shown by the dashed-black line and Fermi level by the dashed-red line. It might have been expected that flow below V_B would be cut off and flow above it unaffected. What we see from Fig. 3.6c however, is that current still flows through the nanoinclusion at lower energies by quantum tunnelling, and at higher energies (even as high as ~2 k_BT above V_B) the current has not yet reached the pristine matrix material level. Due to this far-reaching effect of the nanoinclusion, it also appears that there is no clear relation

between the optimal V_B and the position of E_F in the results above, other than the optimal V_B for maximizing the power factor appears to be approximately half-way between the band edge and the Fermi level. We next discuss this effect with comparison to superlattices.

3.4.2 Nanoinclusions vs Superlattices (SLs) - transport features

Other than the reduction of thermal conductivity, the incorporation of nanoinclusions would have been expected to provide an energy filtering effect and consequently improve the power factor as is the case in transport through cross-plane superlattices (SLs) composed of potential barriers and wells. In SLs, the electrons in the wells have to overpass the heights of the barriers. The higher the barrier, the stronger the reduction in the conductance, which overall is exponential in nature, whereas the Seebeck coefficient increases linearly with the barrier height. It is interesting to compare how the presence of nanoinclusions and superlattice potential wells each influence electronic and thermoelectric transport. In Fig. 3.7 we plot the transmission of a L = 60 nm channel under ballistic coherent conditions for three cases as shown in the insets: i) pristine channel (red line), ii) channel with an 8×4 hexagonal array of NIs (blue line) with barrier height V_B = 0.1 eV and diameter d = 3 nm, and iii) a SL structure of 8 barriers of height V_B = 0.1 eV and width W = 3 nm (black line). What is important to note is the differing effects the two structures have on the low energy electrons below the barrier height. The SL structure effectively cuts of the current flow below V_B = 0.1 eV, providing an energy filtering mechanism that increases the Seebeck coefficient. The behaviour in the presence of NIs is different, because the charge carriers flow not only above the NI barriers, but in between them as well. This means the NIs still allow a finite transmission of carriers across low energies, and thus, do not provide the energy filtering effect and large Seebeck coefficients that can be achieved in superlattices [101], [102], [112].

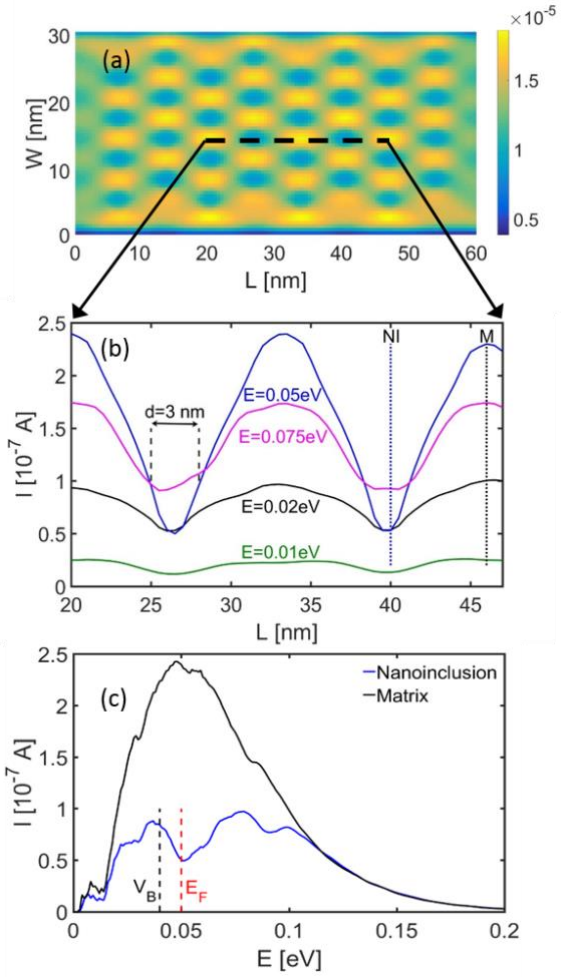

Fig. 3.6: (a) Colour map of the current flow directed along the length of the channel (L-directed) through an 8×4 hexagonal array of nanoinclusions (d = 3 nm, V_B = 0.04 eV). Nanoinclusions can be seen as the blue areas and the matrix material as the yellow and green areas. (b) The channel length directed current along the dashed-black line shown in (a) at four different energies, below the barrier at E = 0.01 eV (green line), at the barrier E = 0.02 eV (black line), at the Fermi level E = 0.05 eV (blue line), and above the barrier and Fermi level at E = 0.075 eV (purple line). The location of the first nanoinclusion (NI), which extends for 3 nm, is denoted. (c) The current flow at two points in the structure: at the centre of a nanoinclusion (blue line, position shown by dotted-blue line in (b) at L ~ 40 nm) and in the pristine matrix (black line, position shown by dotted-black line in (b) at L ~ 46 nm). The barrier height is shown by the dashed-black line and Fermi level by the dashed-red line.

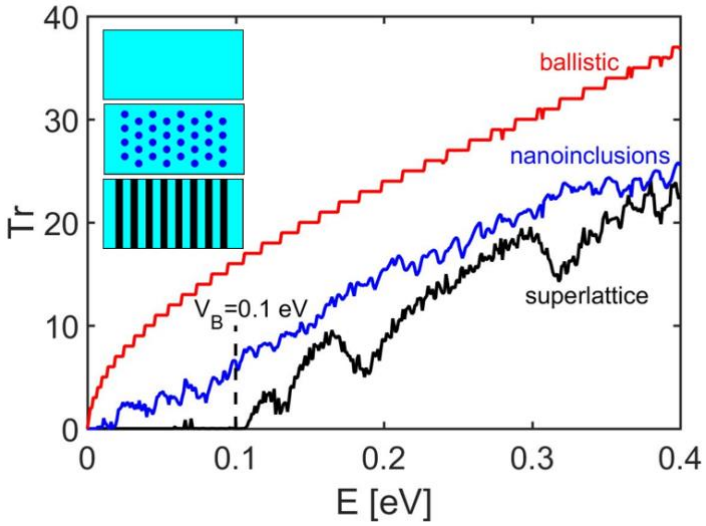

Fig. 3.7: The transmission versus energy for an L = 60 nm ballistic coherent channel (no phonon scattering) for the following cases as shown in the insets: i) pristine material without nanoinclusions (red line), ii) material with an 8×4 hexagonal array of nanoinclusions (blue line) with V_B = 0.1 eV, and iii) a superlattice material (black line) with V_B = 0.1 eV. The barrier height V_B is marked by a dashed-black line. It can be seen that the superlattice is effective at cutting out the contribution of low energy electrons (achieving an increase in the Seebeck coefficient) whereas the nanoinclusions act to reduce the transmission uniformly in the entire energy region.

At higher energies, however, the current does not return to the ballistic value in either the nanoinclusion or the superlattice case, in contrast to what is normally assumed. This might explain why improvements in the power factor from superlattices have yet to be realized, as the conductivity falls further than expected with increasing barrier height. Note that this is an effect that originates from the large mismatch between the number of bands in the matrix material and the barrier, and due to the large degree of quantum interferences. Thus, we expect this to be stronger in 2D, compared to 1D where only one (or fewer) subbands exist in all regions of the structure, for example. We also note that simplified models that consider simple step-function-like transmissions (or even simple 1D transmissions) would provide larger conductance and overestimate the performance. However, in the case where incoherent scattering is stronger, this effect would be reduced.

As a comparison between the *PF* improvements in the two geometries, however, in a superlattice, the power factor can be optimized by placing the Fermi

level high into the conduction band (achieving good conductance). The introduction of the barriers increases the Seebeck coefficient by using barriers ~k_BT above E_F, and finally power factor improvements of the order of ~10-20% can be achieved [106]. In the case of channels with nanoinclusions, on the other hand, as shown in Fig. 3.2c, due to the limited increase in S achieved with nanoinclusions, a somewhat lower power factor enhancement is produced. For non-degenerate conditions (E_F = -0.025 eV and E_F = 0 eV) the conductance drops faster than the Seebeck coefficient rises, and the nanoinclusions have no beneficial effect on the power factor. For degenerate conditions (E_F = 0.025 eV, E_F = 0.05 eV and E_F = 0.075 eV) there is an initial benefit, but in principle, power factor enhancements beyond the pristine structure (with V_B = 0 eV and E_F = 0 eV), are not achieved.

3.4.3 Random variations in nanoinclusion parameters

In this work we exclusively considered structures in which the nanoinclusion geometry, diameter, and density were set in a very specific way, i.e. regular hexagonal arrays of fixed diameter. In reality the nanostructuring in nanocomposite materials takes random forms. The specific location of nanoinclusions, their size, the barrier height and even their density cannot be controlled precisely. Even the position of the Fermi level E_F, which is set by the doping cannot be controlled precisely. In superlattices, for example, it has been shown that variations in the lengths of the various regions do not affect the power factor significantly, however what is detrimental are variations in the barrier heights (that degrade the conductivity) and extremely thin, easy to tunnel barriers (which degrade the Seebeck coefficient) [101], [102]. Although in this chapter we do not perform a full investigation of the influence of statistical variations of the different structure parameters, from the results in Fig. 3.2, Fig. 3.3, and Fig. 3.5, we can extract some expectations on the effect of variations. If we concentrate at the low V_B regions, where the power factor does not suffer, the results in Fig. 3.3 indicate that variability in the nanoinclusion density does not affect the power factor, which indicates that variability in the geometry and positions of the nanoinclusions will also not affect the power factor. Interestingly, the results seem tolerant to significant changes in V_B, which indicates that moderate barrier height variations will also not affect the power factor either, in contrast to the superlattice case. In superlattices variability in the barrier heights is crucial because carriers need

to go through each individual barrier, and the height degrades the conductivity exponentially, whereas in the NI case carriers can actually flow around the nanoinclusions and avoid large barriers. From Fig. 3.5 we can also observe that quantum tunnelling is not as important either, as the energy filtering capabilities of nanoinclusions are limited anyway (in the case of superlattices energy filtering is strong, and tunnelling by making the barriers transparent takes it away). From Fig. 3.2 we can see that the only significant variation that can affect the power factor of the nanocomposite at the low V_B region is the position of the Fermi level E_F, which, however, is the case in all materials, nanostructured or not. Another important variability case that is beneficial to the power factor is the variation in the lattice thermal conductivity between the different materials that form the nanocomposite. In superlattices, for example, a lower lattice thermal conductivity in the barrier regions which have a higher local Seebeck coefficient, results in a larger overall increase in the Seebeck coefficient [33], [61]. We have not investigated this effect here, however, it might be the case that such an effect might not be utilized strongly for NIs as their filtering capabilities are weaker.

3.4.3 Diffusive to ballistic scattering conditions

The structures studied up to this point have used a mean-free-path (mfp) for scattering of mfp = 15 nm and channel length L = 60 nm, which resulted in transport being diffusive within the channel. In reality, different materials can have different mfps, and materials with very light effective masses could even be ballistic in the relatively short channel we simulate. Thus, to cover these cases, in Fig. 3.8 we investigate the main outcomes when channels with different transport regimes are considered: i) ballistic transport (black lines), ii) a channel of larger mfp of 30 nm (blue lines), and iii) a channel with smaller effective mass (green lines). In Fig. 3.8a, 3.9b and 3.9c we show the conductance, Seebeck coefficient and power factor, respectively for the 8×4 hexagonal array of nanoinclusions of diameter d = 3 nm and E_F = 0.05 eV. With red lines we show the corresponding results with mfp = 15 nm and m* = m_0 (same as the red lines in Fig. 3.2 and Fig. 3.3).

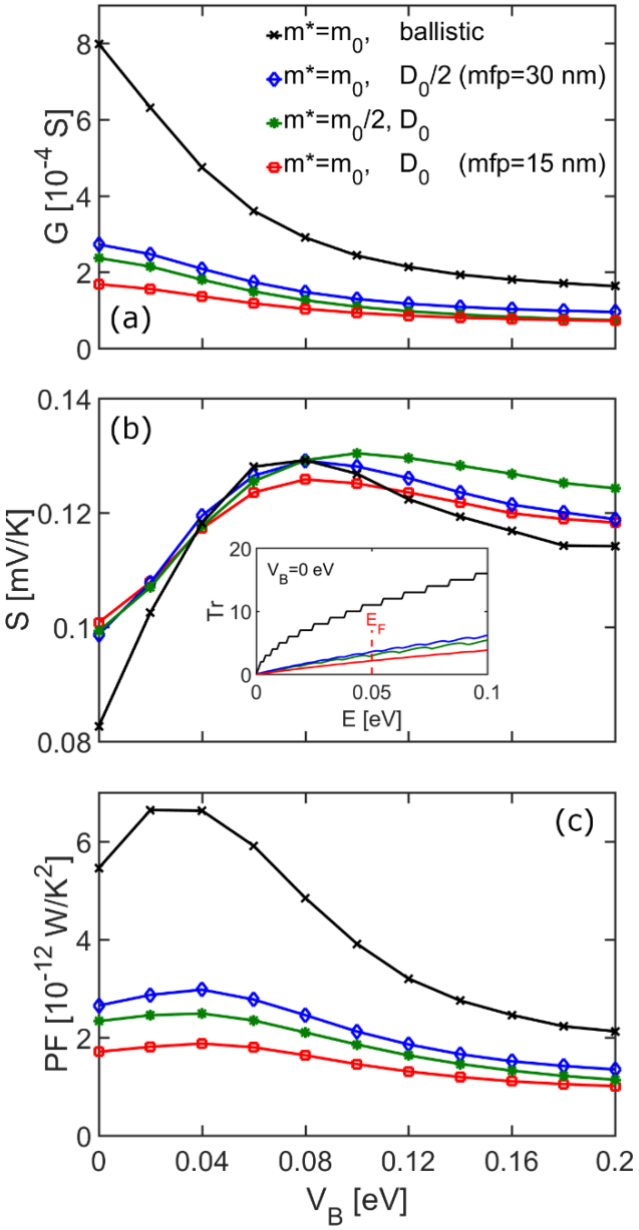

Fig. 3.8: The thermoelectric coefficients of L = 60 nm channels with an 8×4 array of nanoinclusions versus nanoinclusion barrier height, V_B, for four different simulation conditions: Ballistic transport (black lines), mean-free-path mfp = 30 nm and m* = m_0 (blue lines), mean-free-path mfp = 15 nm and m* = 0.5m_0 (green lines), and mean-free-path mfp = 15 nm and m* = m_0 (red lines – same as in Fig. 3.2 and Fig. 3.3). (a) The conductance. (b) The Seebeck coefficient. (c) The power factor defined as GS^2. Inset of (b): The transmission probability versus energy in the four cases for V_B=0 eV.

It can be seen that variations in both the mean-free-path and the effective mass have some effect on G especially for low V_B, but their importance is reduced for larger barrier heights. The effect on S, on the other hand is negligible for low V_B because the energy of the current flow does not change at first order with mfp or effective mass. Consequently the PF is benefitted by ~50% when doubling the mfp's or halving the channel material effective mass, which is expected. Importantly, qualitatively the trend for both cases is very similar to what was seen before. This consistency in the behaviour can also be seen from the transmission shown in the inset of Fig. 3.8b. This shows that the transmission features vary only marginally between the three cases, with the lighter mass and larger mfp channels having a somewhat larger transmission. These results appear to show that the qualitative trends presented previously are robust to variations in mean-free-path and effective mass, suggesting that our conclusions could be applicable to a wide variety of material cases.

In the ballistic case (black lines), while G and the PF increase significantly compared to the diffusive case, it should be emphasized that even here all three parameters follow the trends previously outlined. The fact that S is lower for low V_B has to do with the shape of the transmission (black line in the inset of Fig. 3.8b), rising faster at lower energies, contributing a greater number of lower energy electrons to the current flow than seen in the diffusive channels.

3.4.4 Approximations and omissions

Finally, in this work, for computational simplicity, we have applied the NEGF formalism to short channel 2D nanoribbon structures of sizes W = 30 nm and L = 60nm embedded with hexagonally placed nanoinclusions and showed how it is a very powerful method that captures most of the important details for the assessment of the power factor. In reality, most of the experimentally realized structures are in 3D, which would have made our simulations computationally prohibitive. However, qualitatively, we believe our conclusions still apply to 3D structures as well. In fact, Ref. [102] considered the influence of random variations in the placement of barriers in superlattices, and found that it makes no difference in the power factor; thus we expect the main conclusions to qualitatively carry over from a regular set of structures to a more randomized colloidal placement with only an average separation as well. Furthermore, extrapolating from our findings, we expect that the influence of

nanoinclusions on energy filtering in 3D would be even smaller since many more paths exist for the carriers to flow around the nanoinclusions.

In addition, a certain number of approximations have been made that we would like to elaborate on. First, the nanoinclusions were treated in a very simplified way, just by raising the potential barrier locally. Although this at first order can mimic a nanoinclusion, in reality material deformations exist in the vicinity of the inclusion, strain fields are built, and the effective mass and band details vary, which could have some quantitative influence on our results. Another omission is that in this work we have only considered electron-acoustic phonon scattering (in addition to the electron scattering on nanoinclusions). Optical phonon scattering provides energy relaxation and it is important for optimizing energy filtering in superlattices where electrons absorb phonons to flow over potential barriers and emit phonons in order to relax into the wells [61], [102]. In this case for nanocomposites, however, where most of the charge flows around the nanoinclusions, we omit optical phonons. The inclusion of optical phonons requires an additional computational complexity, which we relax in the interest of being able to simulate larger geometries that more elucidate the effect of nanoinclusions. Electron-ionized impurity scattering is an important mechanism, especially in degenerately doped materials, which can also result in a different energy dependence of the transmission function. In general, although ionized impurity scattering results in significantly lower power factors to begin with, the stronger energy variation in the transmission provides larger opportunities for relative power factor improvements [112], thus, we expect that if that was included in our calculations the power factors would be qualitatively lower, but the increase nanoinclusions could provide would have been somewhat higher. In the case of energy filtering over a barrier in a superlattice, for example, we have previously shown that under ionized impurity scattering power factor improvements could reach up to 30%-40% [33], [112], whereas the relative improvement is half of that when only electron-phonon scattering is considered in the calculations.

Finally, we also need to mention that the perfect barrier shape we employ is just an approximation for ease in limiting the number of simulations to be performed and for focusing on the effects of geometry and density. In reality, in the vicinity of the heterojunction there will be potential variations that will affect the shape of the barrier, which as was shown in Refs. [101], [102], could be important in determining the *PF*. These potential variations are determined by the junction details, but also by

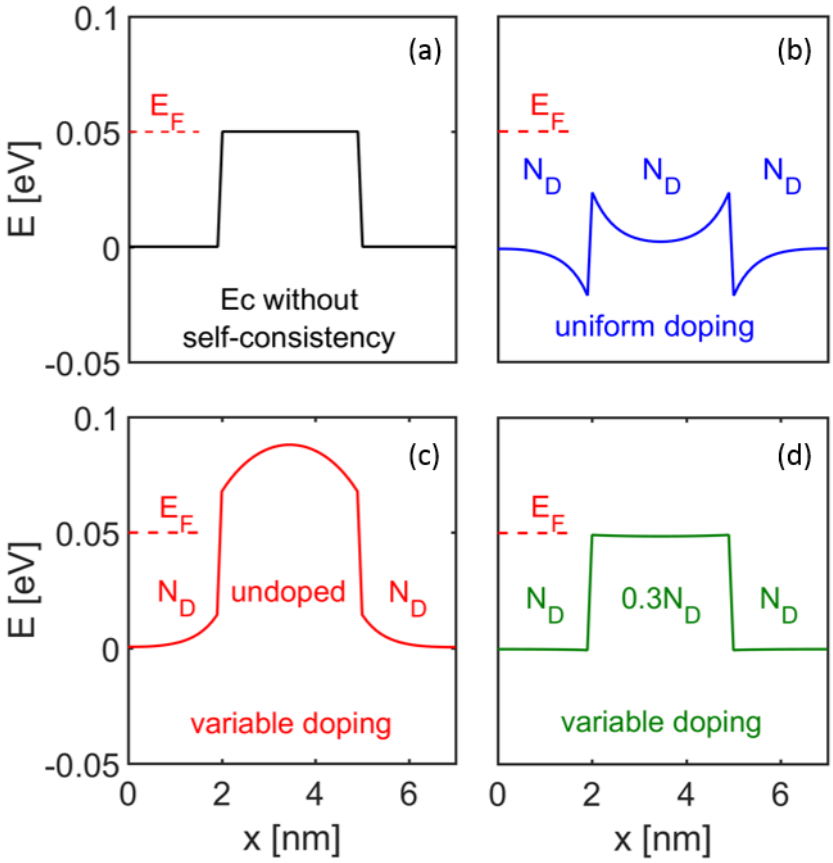

Fig. 3.9: The shape of the barrier around the nanoinclusion for different cases using 1D self-consistent calculations. (a) The perfectly square barrier as used in the simulations. (b) The barrier shape when uniform doping is applied in all domains – Schottky barriers are formed around the nanoinclusion. (c) The barrier shape around the nanoinclusion when only the matrix material is doped, whereas the nanoinclusion remains undoped. (d) A case with variable doping where the doping in the nanoinclusion is reduced to 30% of that in the matrix material. In the latter case the barrier profile looks very similar to the one simulated.

the doping of the different regions and could only be captured accurately through self-consistent calculations, which we do not consider in this work.

Figure 3.9 illustrates various cases of how the barrier shape will look once self-consistent electrostatics is considered (in this case through 1D simulation). For these figures we couple the 1D Poisson equation:

$$\frac{d^2}{dx^2}U(x) = -\frac{\rho(x)}{\varepsilon} \tag{3.1}$$

where x is the position in the transport direction, U is the electric potential, ρ is the charge density, and ε is the permittivity of the medium, with the expression for the charge density:

$$\rho(x) = \int_{U(x)}^{\infty} g(x,E)\, f(E) dE \tag{3.2}$$

where the potential in the channel, $U(x)$ is given from the Poisson equation. The new value for the charge density is then inserted back into the Poisson equation to produce a new potential profile and in this way Eqs. (3.1) and (3.2) are iterated self-consistently until convergence is achieved. Note that the density of states, g, also becomes x-dependent as the potential profile also defines where the band, and therefore the density of states, begins.

In Fig. 3.9a we show the perfectly square barrier we use in the simulations as inserted in the Hamiltonian 'by hand'. In Fig. 3.9b we show how the barrier will look like when uniform doping (N_D = 1.37 × 10_{20}/cm_3 places the E_F at E_F = 0.05eV) is applied in all domains – in that case Schottky barriers are formed around the nanoinclusion. Figure 3.9c shows how the barrier around the nanoinclusion looks like when only the matrix material is doped, whereas the nanoinclusion remains undoped. Finally, Fig. 3.9d shows a case with variable doping where the doping in the nanoinclusion is reduced to 30% of that in the matrix material. In the latter case the barrier profile looks very similar to the one simulated. In each case, the barrier is of course different, and will impact the results. The important point here, however, is that through electrostatic and charging effects a different 'effective barrier' is produced and this is what we consider.

3.5 Conclusions

In conclusion, using the fully quantum mechanical non-equilibrium Green's function method, we calculated the thermoelectric power factor of 2D nanoribbon channels with embedded nanoinclusions modelled as potential barriers. We explain why this method is most relevant, as it captures all geometry details, important quantum mechanical effects such as tunnelling and subband quantization, as well as relevant transport regimes from diffusive to ballistic, and coherent to incoherent. These are all important features that affect transport through such structures and need to be captured for an accurate understanding of their thermoelectric properties as we

showed in the results throughout the chapter. Thus, this work avoids approximations in geometry and in essential transport features that could limit the proper design and optimization of nanostructured thermoelectrics. An important message of the chapter is that we showed that, unfortunately, the addition of nanoinclusions does not utilize energy filtering effectively, and cannot provide higher power factors compared to an optimized structure without nanoinclusions (in the optimal pristine material case the Fermi level is placed around the conduction band edge). The introduction of nanoinclusions reduces the conductance, but does not provide the corresponding increase in the Seebeck coefficient. However, under degenerate conditions, where the Fermi level is placed into the conduction band, moderate increases in the power factor can be achieved of the order of 5-10% if the nanoinclusion barrier heights are between the Fermi level E_F and the conduction band E_C. Importantly, however, we showed that in that case, the mild power factor improvements are independent of the nanoinclusion density, as long as the nanoinclusions are large enough to prevent quantum tunnelling. This indicates that larger densities of relatively thick nanoinclusions can be utilized to effectively reduce the lattice thermal conductivity without degradation in the power factor. For larger barrier heights, a non-intuitive simultaneous drop in the conductance and Seebeck coefficient is observed, which degrades the power factor significantly. Our results reveal that the filtering behaviour of materials with nanoinclusions are different compared to the filtering behaviour of cross-plane superlattices. Our conclusions would be useful in the design of advanced nanostructured thermoelectric materials.

IV. Thermoelectric power factor in nanostructured materials with randomized nanoinclusions

4.1 Introduction

In chapter 3 we demonstrated the possibility for nanoinclusions in ordered systems to provide small enhancements in the power factor. In real systems, such structures are disordered and far from the idealized systems we simulated. Therefore in this chapter we extend the results presented in the previous chapter by taking structures close to the optimal and investigating the effect of random variations in the positions, diameter and the heights of the barrier. In figure 4.1 we show the *PF* versus barrier height of an 8×4 hexagonal array of NIs in a 2D channel matrix for two different scattering regimes; namely, ballistic (black-cross line) and acoustic phonon scattering (red-square line) regime. With the brackets we indicate the regions of interest, that is when $V_B \sim k_B T$ -$2k_B T$ above the band edge. In these regions the *PF* shows only a minor change as the barrier height is varied.

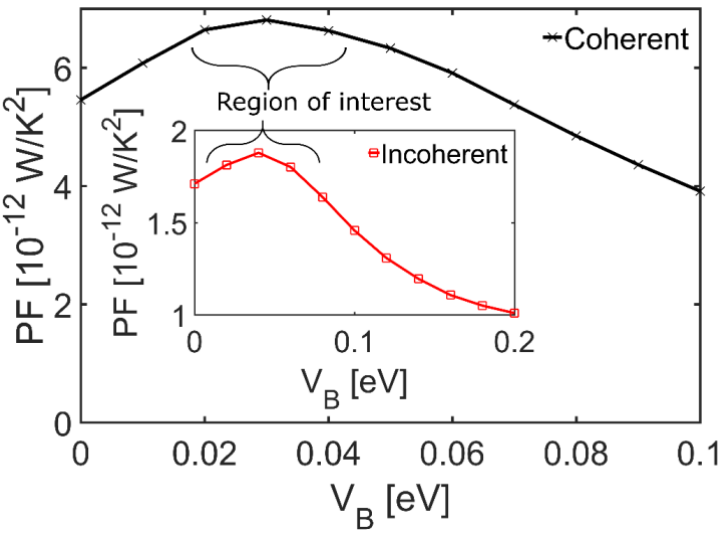

Fig. 4.1: The *PF* of a matrix material containing an 8×4 hexagonal array of nanoinclusions vs nanoinclusion barrier height for two scattering regimes: Ballistic (coherent) transport (black-cross line), and acoustic phonon scattering transport (red-square line).

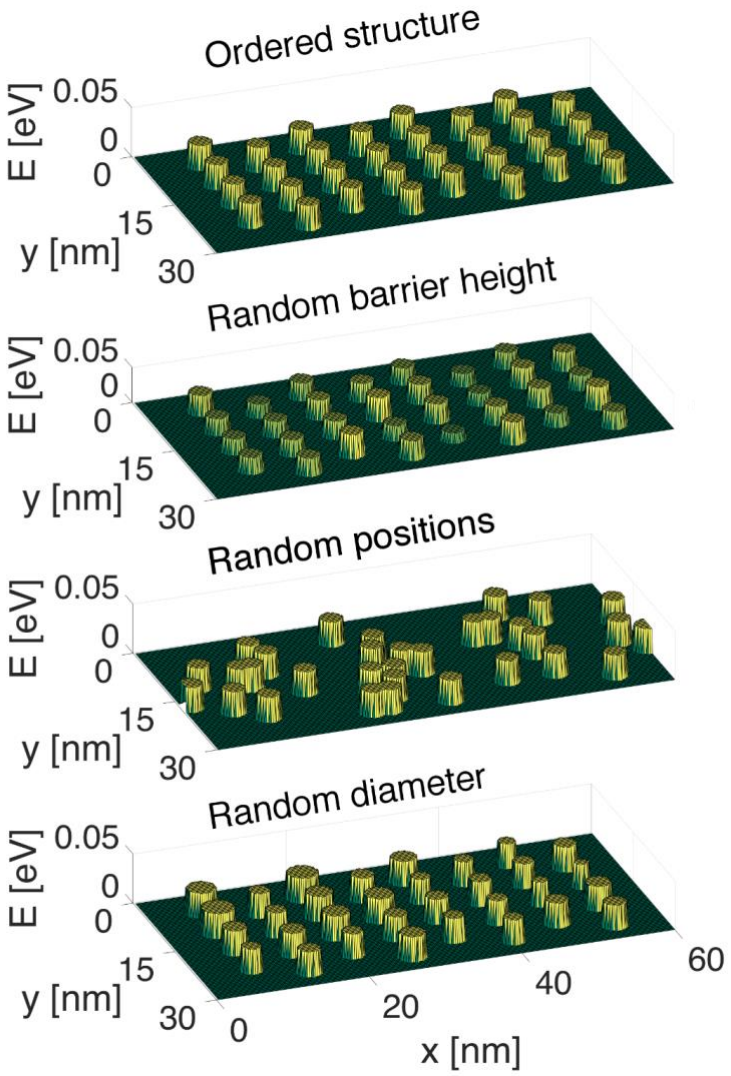

Fig. 4.2: Examples of the materials with embedded NI geometries we consider: (a) the ordered structure consisting of 8×4 hexagonal array of NIs of barrier height V_B = 0.025 eV and diameter d = 3 nm. (b) An 8×4 hexagonal array of NIs with random barrier height and diameter d = 3 nm. (c) A random distribution of 32 NIs of barrier height V_B = 0.025 eV and diameter d = 3 nm. (d) An 8×4 hexagonal array of NIs of barrier height V_B = 0.025 eV and random diameter.

The purpose of this chapter is to extend our previous work aiming to verify the tolerance of the *PF* to such types of variations and randomness in nanocomposite materials. The NIs are modelled as potential barriers of cylindrical shape (see Figure 4.2). In particular, we investigate the effect of randomness of the NIs on the *PF*; namely, the positions, diameter, and heights of the barriers are varied according to a Gaussian probability distribution. Such random variations, which reflect the

imperfections in nanocomposite materials, are inherently present in any real, experimental system and their effects have to be taken into account. We find that materials with NIs, once doped in highly degenerate levels and the barriers are one or two k_BT above the band edge, are robust to variations in the NI barrier height, the NI diameter, and their geometry. Our results could prove useful in the design of nanocomposite materials that provide *PF* robustness.

The rest of this chapter is organized as follows. In Section 4.2 we present the results and our analysis and we conclude with a summary in Section 4.3.

4.2 Results

As in chapter 3 we employ the NEGF method described in chapter 2 to calculate the electronic transport properties of 2D systems embedded with nanoinclusions. The 2D channel that we consider is of length L = 60nm and width W = 30nm (see Figure 4.2).The e-ph scattering strength is set at D_0 = 0:0026 eV^2. The conduction band is set at E_C = 0 eV and the Fermi level is placed at E_F = 0:05 eV.
We begin with an investigation into the effect of variations in a ballistic channel. In Figure 4.3 we show the thermoelectric coefficients, conductance G (Fig. 4.3a), Seebeck coefficient S (Fig. 4.3b), and $PF = GS^2$ (Fig. 4.3c) of a ballistic channel with an 8×4 hexagonal array of NIs as two different parameters are varied: the barrier diameter d (blue lines), and the barrier height V_B (red lines). The leftmost points, for zero variation, are the values for the ordered channel which includes an 8×4 hexagonal array of NIs with fixed d = 3 nm and V_B = 0:025 eV as shown in Fig. 4.2a. We consider variations up to 30% in the parameters (and use averaged data from at least 10 simulations for each point). It can be seen that variation in barrier height has negligible effect on G and S, and due to the adverse interdependence of G and S, the minor effect that is seen cancels out leaving no significant change in the *PF* even at 30% variation. Likewise, variation in the NI diameter, although slightly more consequential than barrier height, shows little impact on the thermoelectric coefficients. [Interestingly a small positive effect on the *PF* is seen, although this is probably due to the statistical variation in diameter leading to a small increase in overall density, increasing the small energy filtering effect of the barriers].

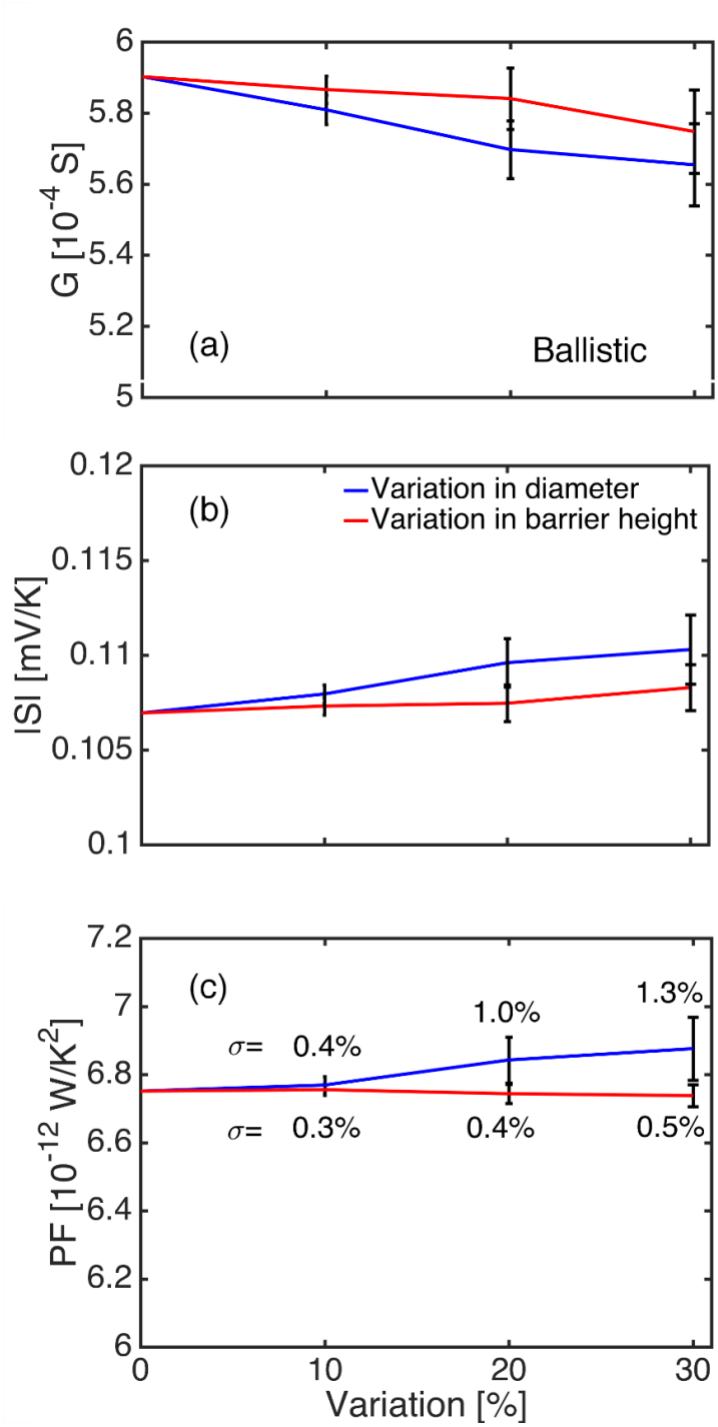

Fig. 4.3: The effect of variations of the NI diameter and barrier height on the thermoelectric coefficients. (a) The electrical conductance, (b) the Seebeck coefficient, (c) the power factor, versus the percentage variation from the nominal values. Variations in the radius (blue lines) and barrier height (red lines) are shown. Each data point is the average of at least 10 simulations and the error bars indicate the standard deviation of the results (shown by the labels).

The next investigation we perform is to explore the effect of variations in the geometry of the channel. We again simulate a ballistic channel with a total of 32 cylindrical barriers of height V_B = 0.025 eV and diameter d = 3 nm. In this case each of the NIs is randomly placed in the channel as shown in Fig. 4.2c rather than in an ordered hexagonal fashion. The NIs are treated as a region in the matrix material with a different band energy. From the electronic point of view, these are regions which build potential barriers in the matrix material. One could be more flexible as to define a different effective mass as well in those regions, as well as built-in potentials due to charge fluctuations which could lead to Schottky barriers, etc., but this is beyond the scope of this work. Other than that, NEGF is a real space technique, where transport is described quantum mechanically and the details of the geometry, accurately. To be able to treat real materials, one could employ details of the bandstructures (effective masses, degeneracies, mean-free-paths, phonon energies), possibly extracted from Density Functional Theory (DFT) calculations, but again this is beyond the scope of this work.

In Figure 4.4 we show the histograms of the conductance G (Fig. 4.4a), Seebeck coefficient S (Fig. 4.4b), and $PF = GS^2$ (Fig. 4.4c) of 40 random geometries and a Gaussian fit calculated from the results. It can be seen that, although the standard deviation values are slightly higher than the previous cases considered, most values fall within just a few percent of the mean.

In order to achieve a complete picture of the transport through disordered nanocomposites, we now consider the effect of variations on a channel in the acoustic phonon scattering regime. In Figure 4.5 we show the thermoelectric conductance G (Fig. 4.5a), Seebeck coefficient S (Fig. 4.5b), and $PF = GS^2$ (Fig. 4.5c) of a channel with an 8×4 hexagonal array of NIs as two different parameters are varied: the barrier diameter d (blue lines), and the barrier height V_B (red points).

Similarly to the ballistic case (compare with Figure 5) variation in the diameters of the NIs produces only small changes in G and S, which cancel out in the PF leaving it relatively unchanged. In the same way, small variations in the barrier height have no significant impact on the PF. Here we only simulated variations at the 30% level for the barriers since it will provide the largest variation in the PF of the percentages that we have considered.

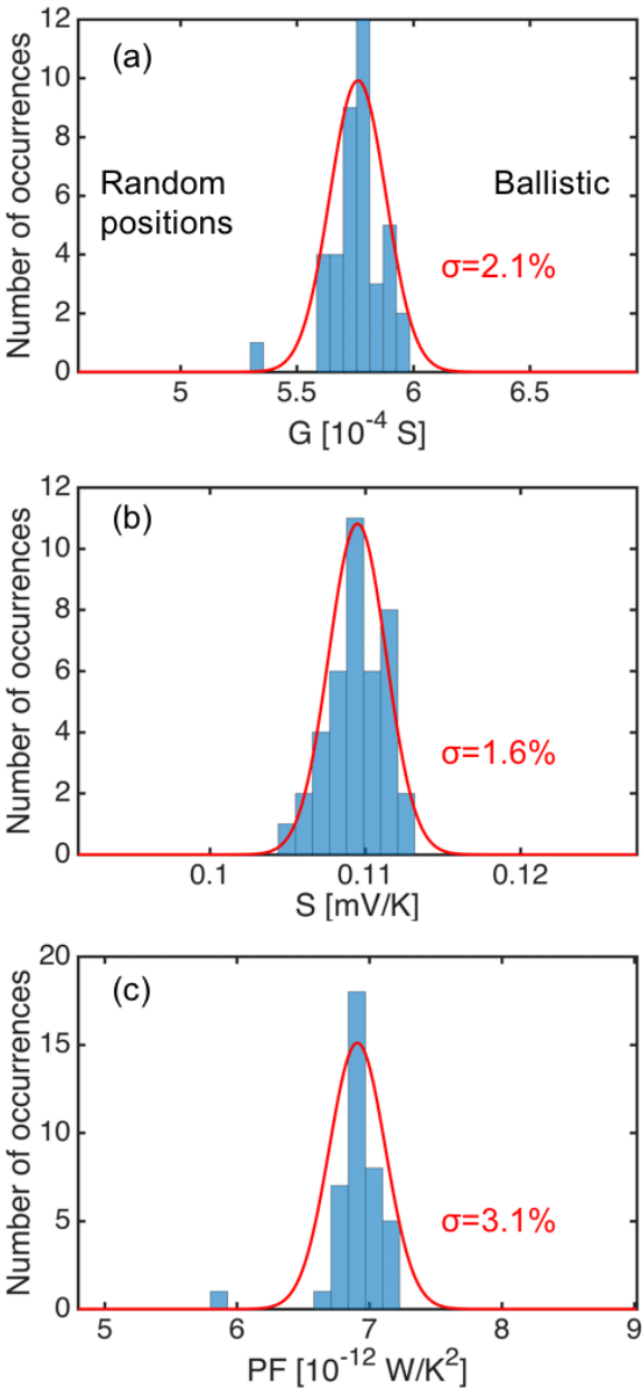

Fig. 4.4: Histograms of the values of (a) the conductance G, (b) the Seebeck coefficient S, and (c) the $PF = GS^2$ for geometries with randomized pore positions under ballistic transport conditions.

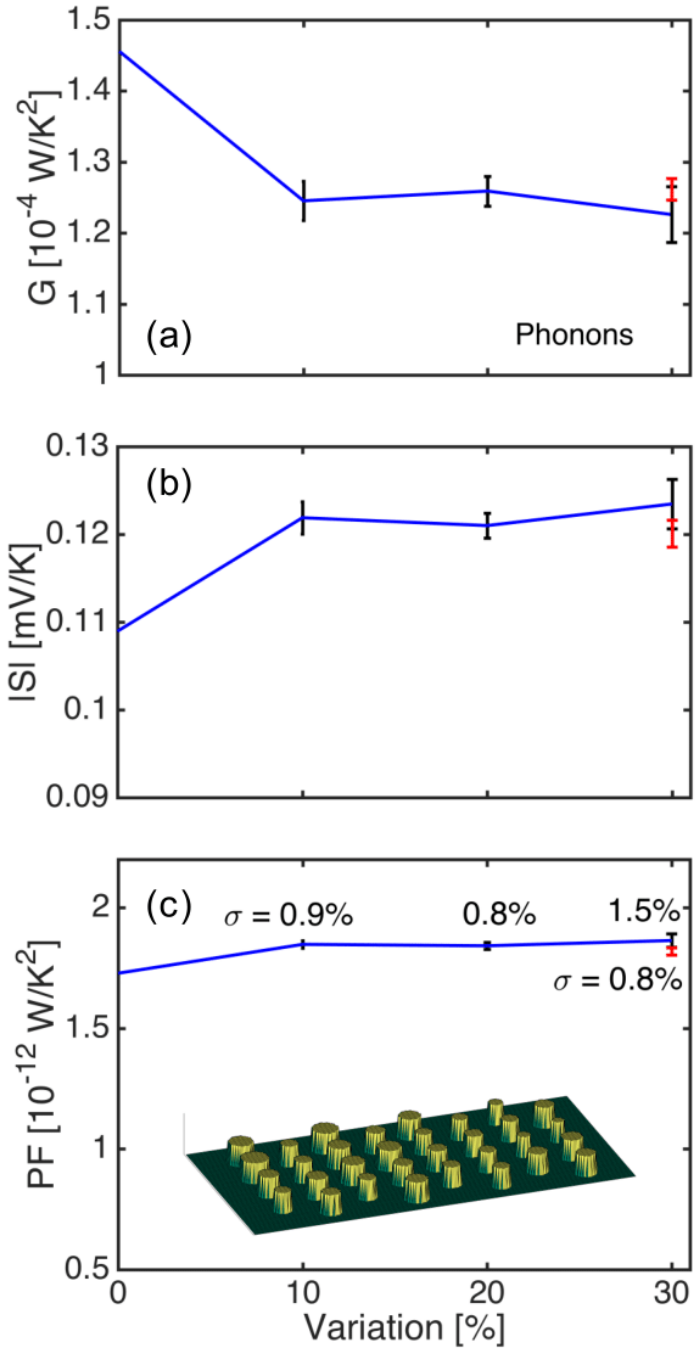

Fig. 4.5: The effect of variations in the diameter (blue lines) and barrier height (red points) on the thermoelectric coefficients. (a) The conductance, (b) the Seebeck coefficient, (c) the *PF*. In the inset of (c) we show an example geometry with a 30% variation in diameter. In (c) we also show the standard deviations in our values of the *PF*.

It is of interest at this point to compare our above results to previous works on variations in superlattices [101], [102]. It was previously shown that the thermoelectric transport in superlattices is highly sensitive to variations in the barrier heights. This is because in superlattices each electron must pass through each individual barrier region, providing a strong energy filtering effect. The height of each barrier degrades the conductivity exponentially, meaning variations away from the optimal structure can have a significant impact on the power factor. In the NI case, however, electrons can flow around the NIs. In fact, most of the current of the flow is through the matrix material (see chapter 3) which is not affected by variations in the barrier height. Variations in the NI structure therefore do not have a large effect on the electron transport and the power factor is similarly unaffected.

4.3.1 Approximations and simplifications

We would like to comment on certain approximations/simplifications that we have made in this work. First, even though a local potential barrier is a legitimate way to model a NI to first order, in real materials there may be deformations in the vicinity of a NI, which can produce strain fields that lead to modified effective mass and band details. In addition, we ignored self-consistent charging effects that could alter the shape of the barrier, although this was discussed in chapter 3. Further, we considered only ballistic transport and phonon scattering, and neglected ionized impurity scattering, which could suppress the *PF*s quantitatively [33], but qualitatively would not change the results on the effects of variations.

Finally, we mention that the treatment of phonons in this chapter is simplified and is adjusted to provide a certain reasonable mean-free-path (already quite complicated computationally within a fully quantum mechanical formalism, however). The details of the phonon spectrum are even neglected, however, in any case in this study we are after qualitative conclusions for the power factor in the presence of variations, which seems to be minimal anyway and even smaller when phonon scattering gets stronger. Also, we do not consider a specific material, but keep the study as generic as possible, focusing qualitatively on the geometrical influences on transport. A more detailed el-ph model is possible, but computationally expensive, possibly prohibitive for the size of structures we consider here. Previous works [117] have considered full phonon dispersions to construct the self-energies that enter the

Greens function, but those studies were limited to nanowire channels of only up to 3 nm in diameter.

We also point out that transport in the type of structures that we consider here is not much dependent on the effective mass as shown in chapter 3. When it comes to extending this study to realistic, complex bandstructure materials, atomistic techniques (tight-binding, DFT) can be used to provide effective parameters, since coupling atomistic methods to NEGF is accompanied by an enormous computational cost it would however limit the size of the structure that we simulate.

4.4 Conclusions

In conclusion, using the fully quantum mechanical non-equilibrium Greens function method, we investigated the effect of random variations in the parameters of a 2D nanocomposite channel on the thermoelectric coefficients: conductance, Seebeck coefficient, and power factor. We showed that, unlike superlattices, materials with NIs are robust to variations in the barrier height. We also showed this robustness holds for variations in the NI diameter and NI geometry. Our findings suggest a design regime for nanocomposites that should provide power factor robustness while achieving reductions in the lattice thermal conductivity. In particular, we showed a design regime for which the density and geometry can be optimized for maximum phonon scattering and maximum reduction in thermal conductivity while preserving the power factor, producing high *ZT*.

V. Quantum transport simulations for the thermoelectric power factor in 2D nanocomposites

5.1 Introduction

In chapter 3 we studied the impact of nanoinclusions of finite barrier height on the power factor; we now extend that work and compare it to the influence of voids which can be considered infinite potential barriers.

As discussed in chapter 3, nanoinclusions are highly effective at reducing κ beyond bulk values [6], [35]–[38], [50]. Many of the best thermal conductivity results have come, however, from nanoporous materials (see Fig. 5.1) [66]. While this impact on thermal conductivity is well studied [30], [64], [65], it is not so clear from previous results what impact there is on the power factor in such geometries.

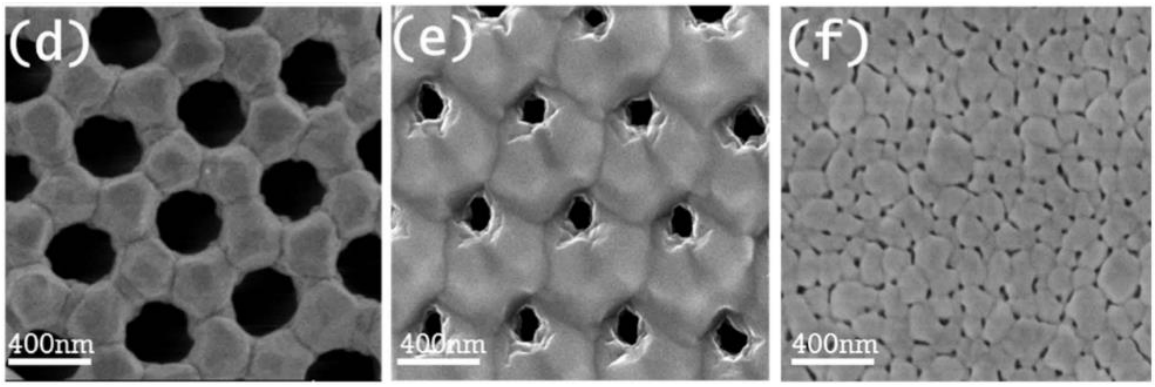

Fig. 5.1: SEM images of $Si_{0.8}Ge_{0.2}$ nano-meshed films reproduced from Ref. [66].

In this work we use the fully quantum mechanical non-equilibrium Green's function (NEGF) simulation method to calculate the electronic and thermoelectric transport properties of 2D geometries embedded with nanoinclusions and voids. We show that nanoinclusions can have a positive impact on the Seebeck coefficient, and that consequently the power factor is not severely degraded by reductions in the conductance. In the ballistic regime, we show that the power factor is independent of nanoinclusion/void density, while in the phonon scattering case increasing density has a detrimental effect on the power factor.

Our simulation method is outlined in Section 2. In Section 3 we present and discuss our results before drawing our conclusions in Section 4.

5.2 Approach

The NEGF theory is described in chapter 2. The system is treated as a 2D channel within the effective mass approximation, using a uniform $m^* = m_0$ throughout the channel, where m_0 is the rest mass of the electron. The nanoinclusions are modelled as potential barriers of cylindrical shape within the matrix material as shown in the schematic of Fig. 5.1. The system size is of width W = 30 nm and length L = 60 nm.

We assume room temperature T = 300 K throughout the chapter. The value of D_0 is chosen such that the conductance of an L = 15 nm long pristine channel is found to be 50% of the ballistic value. This effectively amounts to fixing a mean-free-path of 15 nm for the system as described in chapter 3. Thus, with such a mean-free-path, the L = 60 nm channel length we consider is large enough to result in diffusive transport in the material we simulate. The conduction band is set at E_C = 0.00 eV and the Fermi level is placed at E_F = 0.05 eV.

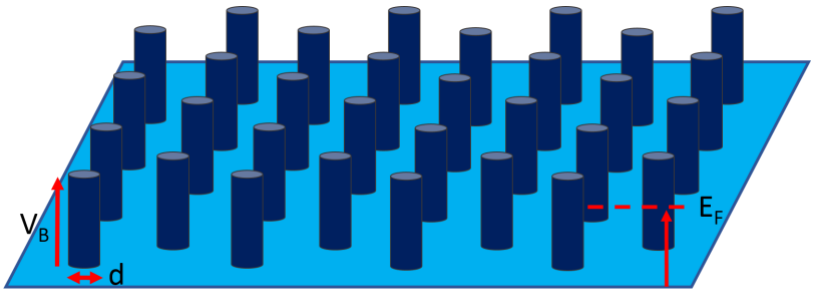

Fig. 5.1: A schematic of a typical geometry we consider. V_B is the barrier height, d the nanoinclusion diameter, and E_F the Fermi level.

5.3 Results

Once the calibration is completed we proceed to consider geometries which include circular nanoinclusions of different barrier heights, V_B, voids, different NI/void densities, and different NI/void diameters. The channel width was kept at W = 30 nm, and the length at L = 60 nm in all cases.

5.3.1 Influence of barrier height V_B and density under ballistic conditions

We first consider the ballistic (coherent) scattering regime. The thermoelectric coefficients *G*, *S* and *PF*, are shown in Fig. 5.2 versus barrier height V_B for four simulated geometries as shown in the insets of Fig. 5.2c. The four simulated geometries are: i) a 2×4 array (green lines), ii) a 4×4 array (black lines), iii) a 6×4 array (blue lines), and iv) an 8×4 array (red lines), and the Fermi level is placed at E_F = 0.05 eV (dashed-red line in Fig. 5.2c). Figure 5.2a shows that, as expected, *G* decreases both with increasing V_B, and with increasing NI/void density. Increasing NI/void density leads to an increase in the Seebeck (shown in Fig. 5.2b) although in the void case the situation becomes more complicated as coherent resonance effects come into play. The result of the improvement in *S* is that the power factor (shown in Fig. 5.2c) increases from the pristine channel value at a barrier height V_B = 0.05 eV, before falling again.

5.3.2 Influence of barrier height V_B and density under phonon scattering

The second investigation we perform is on the influences of: i) the nanoinclusion barrier height, V_B (including voids – with effective infinite barrier height) and ii) the density of nanoinclusion/voids, on the thermoelectric coefficients in the acoustic phonon scattering regime. Fig. 5.3 shows the thermoelectric coefficients conductance *G*, Seebeck coefficient *S*, and power factor GS^2 versus V_B for four different geometries of increasing density. The four simulated geometries are again: i) a 2×4 array (green lines), ii) a 4×4 array (black lines), iii) a 6×4 array (blue lines), and iv) an 8×4 array (red lines). The Fermi level is placed at E_F = 0.05 eV (dashed-red line in Fig. 5.3c). From Fig. 5.3a we can see that, as before, as the barrier height is increased *G* falls, while *G* also falls as the density of the nanoinclusions/voids is increased. *S* shows an initial increase as low energy carriers are filtered out before falling and saturating at an in-between value. Since the Seebeck coefficient $S \propto \langle E - E_F \rangle$ S $\propto <$ E-E_F $>$ (i.e. *S* is proportional to the average energy of the current flow) this saturation appears to suggest that after $V_B \sim 2k_BT$ above E_F, electrons of all energies contributing to the current are affected relatively equally and we show this later. The continued decrease in *G* however (comparing V_B = 0.1 eV to the voids in Fig. 5.3a) indicates that there is a further reduction in flow, but that this occurs relatively evenly across the energy range. Fig. 5.3c shows the results of these effects on the power factor. The initial introduction of a barrier has a reasonably limited effect

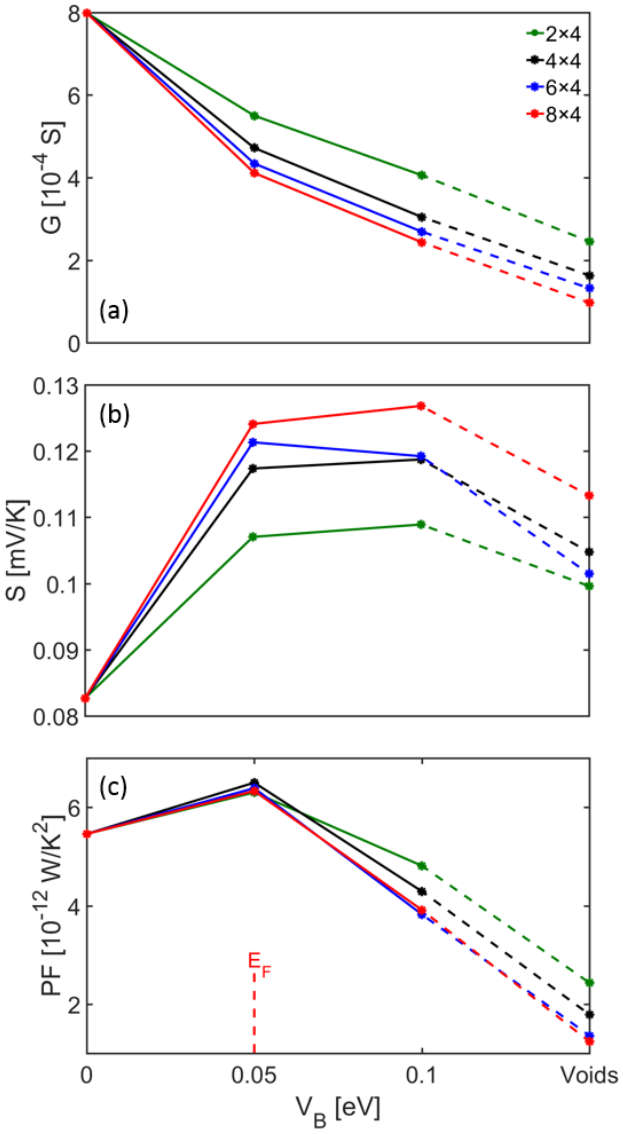

Fig. 5.2: The thermoelectric coefficients of an L = 60 nm channel with E_F = 0.05 eV (dashed-red line) and ballistic transport conditions versus nanoinclusion barrier height, V_B. The conductance. (b) The Seebeck coefficient. (c) The power factor defined as GS^2. Hexagonal arrays of four different nanoinclusion and void densities are considered as shown in the inset of (Fig. 5.2c): 2×4 array (green lines), 4×4 array (black lines), 6×4 array (blue lines), and 8×4 array (red lines).

on the power factor (only a 15% reduction even at the largest NI density) while a further increase of $2k_BT$ in the barrier height produces a more significant reduction (a further 26% at the largest NI density). Interestingly this fall is larger than that from V_B ~ 0.1 eV to voids (a further 17% at the largest NI density) reflecting the fact that the

majority of the electron flow occurs within $2k_BT$ of E_F. Due to the detrimental impact of the NI/voids on *G*, the *PF* also degrades as the NI/void density is increased, and there is no increase at $V_B = 0.05$ eV as was seen in the ballistic case.

5.3.3 Influence of density and void diameter

The next investigation we perform is to illustrate the effects that density and void diameter have on the thermoelectric coefficients. Fig. 5.4 shows the thermoelectric coefficients *G*, *S* and *PF*, versus void density for two void diameters: i) $d = 3$ nm (red lines), and ii) $d = 1.5$ nm (black lines). An example geometry for each void diameter is shown in the inset of Fig. 4c. The Fermi level is placed at $E_F = 0.05$ eV, and acoustic phonon scattering is included. As expected, an increase in the void density reduces *G* and increases *S*. At higher densities resonances and interference effects have an additional detrimental impact on *G* for the small diameter (since the average distance between the voids becomes smaller than the mean-free-path) and produce an equivalent increase in *S*. The overall effect on the *PF* is a reduction as expected from Fig. 5.3. What is important to note, however, is that this reduction is independent of the void diameter, even at higher densities where quantum effects become important.

5.3.4 Features of the electron flow

Finally, to better understand the electronic transport through the geometries we have considered we show in Fig. 5.5 the transmission and the current as they vary in energy. In Fig. 5.5a we show the transmission for four different scattering cases: i) the pristine channel in the coherent ballistic regime (blue 'staircase' line), ii) the pristine channel with acoustic phonon scattering (red line), iii) a channel with an 8×4 array of $d = 3$ nm voids in the coherent ballistic regime (light blue line), iv) a channel with an 8×4 array of $d = 3$ nm voids and acoustic phonon scattering (light red line). The ballistic transmission of the pristine channel shows the expected staircase shape, with an increment every time a new subband is reached in energy. When voids are inserted into the geometry the transmission is reduced significantly as well as showing resonance features. Those resonances are smoothened out when phonon scattering is included, and the transmission is reduced even more when voids are added in addition to phonon scattering.

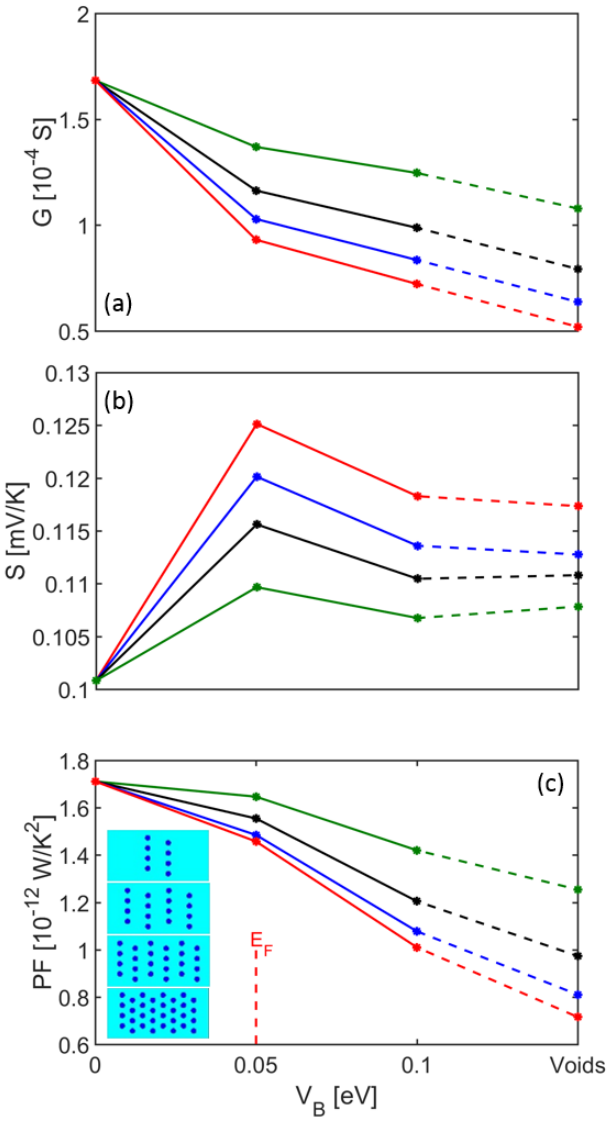

Fig. 5.3: The thermoelectric coefficients of an L = 60 nm channel with E_F = 0.05 eV (dashed-red line) and acoustic phonon scattering transport conditions versus nanoinclusion barrier height, V_B. The conductance. (b) The Seebeck coefficient. (c) The power factor defined as GS^2. Hexagonal arrays of four different nanoinclusion and void densities are considered as shown in the inset of (c): 2×4 array (green lines), 4×4 array (black lines), 6×4 array (blue lines), and 8×4 array (red lines).

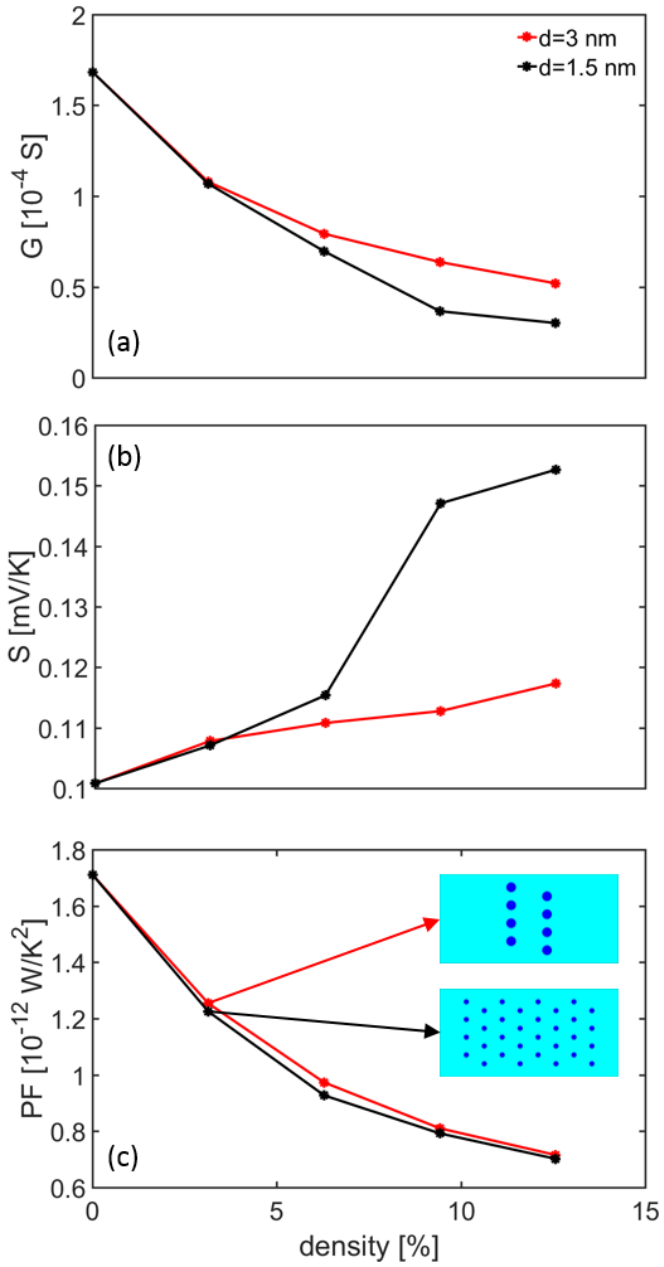

Fig. 5.4: The thermoelectric coefficients of an L = 60 nm channel with E_F = 0.05 eV and acoustic phonon scattering transport conditions versus void density. (a) The conductance. (b) The Seebeck coefficient. (c) The power factor defined as GS^2. Two different diameters of voids are considered: i) d = 3 nm (red lines), ii) d = 1.5 nm (black lines). An example geometry for each void diameter is shown in the inset of (c).

In Fig. 5.5b we plot the energy-weighted current in the transport direction versus energy for two acoustic phonon scattering different cases: i) a channel with an 8×4 array of d = 3 nm nanoinclusions with barrier height V_B = 0.1 eV (black line), ii)

a channel with an 8×4 array of d = 3 nm voids (blue line). It can be seen that changing from nanoinclusions of barrier height V_B = 0.1 eV to voids affects electrons of all energies similarly (including those with energies below V_B = 0.1 eV). This explains the lack of any change in S as we go from nanoinclusions of barrier height V_B = 0.1 eV to voids as shown in Fig. 3b. Because all electron energies are affected to a similar degree, the average energy of the current flow does not change and hence, since $S \propto \langle E - E_F \rangle$ S $\propto <$ E-E_F $>$, neither does S.

At this point, we would like to comment on the possible consequence of our results for the figure of merit ZT. While we have not performed thermal conductivity calculations on the structures we consider (this will require elaborate Molecular Dynamics (MD) or Monte Carlo (MC) simulations), we now qualitatively combine our power factor results with thermal conductivity results found in the literature. In Ref. [118], Dunham *et* al. claim from experiments and MC simulations that small void diameters (~4 nm) in Si channels, similar to those we consider, can result in thermal conductivity reductions of an order of magnitude compared to the bulk. In another work, Lee *et* al. showed from MD simulations that small diameter voids can produce reductions from the bulk value of Si by up to two orders of magnitude [32]. Likewise, MD simulations of nanoporous SiGe have shown thermal conductivity reductions of over an order of magnitude [119]. If we combine this with the halving of the power factor shown in Fig. 4c, we can extract a rough estimate of at least 5x increase in ZT. In the case of nanoinclusions, one would expect that the thermal conductivity reduction is not as strong compared to the case of nanovoids, however, in a number of examples where nanoinclusions are formed within matrix materials it is still found that thermal conductivity can be reduced by an order of magnitude [28], [120]. Since in this case we see little change in the power factor (see Fig. 5.3c), we would expect that ZT could see up to an order of magnitude improvement.

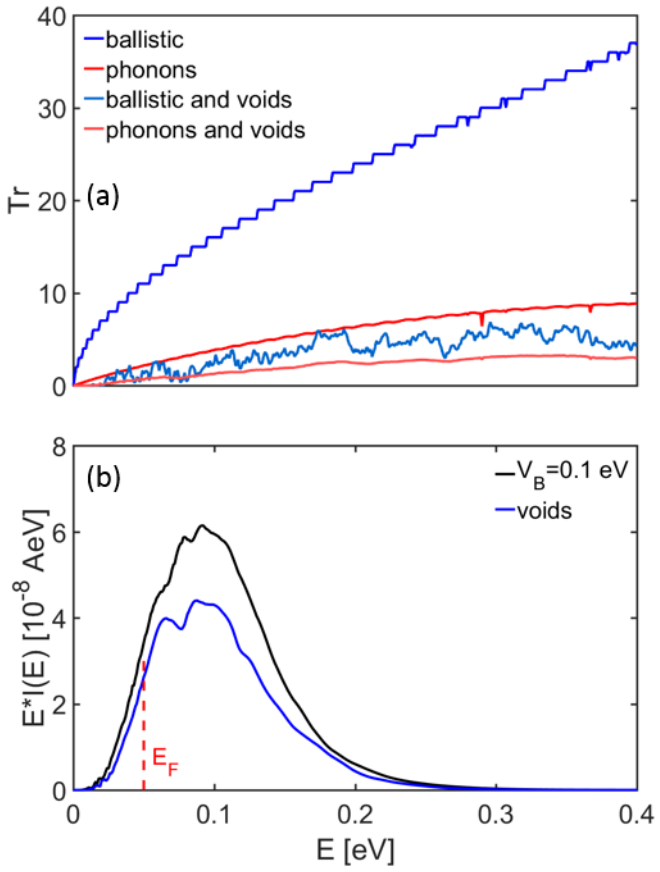

Fig. 5.5: (a) The transmission versus energy for an L = 60 nm channel in four different cases: i) a pristine channel under ballistic conditions (blue line), ii) a pristine channel under acoustic phonon scattering conditions (red line), iii) a channel with an 8×4 hexagonal array of voids under ballistic conditions (light-blue line), iv) a channel with an 8×4 hexagonal array of voids under acoustic phonon scattering conditions. (b) The energy-weighted current flow in the transport direction versus energy under acoustic phonon scattering conditions for two cases: i) a channel with an 8×4 hexagonal array of nanoinclusions of barrier height V_B = 0.1 eV (green line), ii) a channel with an 8×4 hexagonal array of voids (blue line).

5.4 Conclusions

Using the fully quantum mechanical non-equilibrium Green's function method, we calculated the electronic and thermoelectric coefficients of 2D channels embedded with nanoinclusions and voids. We found that while nanoinclusions and voids can have a positive impact on the Seebeck coefficient, the overall effect on the power factor is limited. We show that the power factor is resilient to variations in

nanoinclusion/void density at all barrier heights in the ballistic regime, while under acoustic phonon scattering, the power factor is resilient to variable nanoinclusion/void density only at low barrier heights. We also show that the effect of voids on the power factor is dependent primarily on void density, and independent of void diameter.

VI. Doping optimization for the power factor of bipolar thermoelectric materials

6.1 Introduction

Many of the most important TE materials are narrow bandgap semiconductors [121]. These narrow bandgaps (e.g. PbTe ~ 0.3 eV [122], Bi_2Te_3 ~ 0.2 eV [123], SnSe ~ 0.39 eV [53]) mean the materials suffer from bipolar effects at high operating temperatures. The bipolar effect occurs when both electrons and holes contribute to charge transport. When this happens: i) κ_e increases due to contributions from both electrons and holes, ii) an additional thermal conductivity term, the bipolar thermal conductivity, κ_{bi}, is introduced (a result of electron-hole recombination at the contacts) [124], which also introduces large increases in the Lorenz number [83] iii) the Seebeck coefficient drops as both electrons and holes contribute to it with opposite signs, and iv) the Fermi level moves towards the midgap in order to conserve carrier concentration, (although it does not fall as quickly as in the unipolar case). The thermal conductivity from i) and ii) degrades thermoelectric performance through the denominator of *ZT*, whereas iii) degrades performance through the numerator.

The optimal thermoelectric performance (for both the peak *PF* and peak *ZT*) depends heavily on the carrier concentration [125], and this optimal is known to be temperature dependent, i.e. the performance peaks at different doping concentrations for different temperatures [126]. However, although it is known that for unipolar materials the optimized doping increases as $T^{3/2}$ [82], the optimization of the carrier concentration for bipolar systems is not yet clarified.

While various strategies have been suggested to reduce the bipolar effect in order to regain high performance, such as using heterostructure designs [116], [127], band engineering to widen the bandgap [128], [129], grain boundaries with barriers for minority carriers [8], in this chapter we show that considering proper doping optimization by taking into account the bipolar effects could also allow for performance improvements.

For this we use Boltzmann transport theory and a two-band model (conduction and valence band) to examine the impact of the bipolar effect on the thermoelectric

transport coefficients (σ, S, and the PF), as well as its effect on the optimal carrier concentration and doping. We show that the typical models and trends employed in the literature for optimal doping concentrations for maximizing the power factor and ZT for a unipolar material are no longer valid in bipolar materials. We show that optimizing the carrier concentration for the operating (higher) temperatures can provide significant increases in the power factor and ZT compared to maintaining a low temperature optimized carrier concentration.

6.2 Approach

To calculate the thermoelectric coefficients we use the linearized Boltzmann transport formalism as described in chapter 2. In this method the electrical conductivity (σ), the Seebeck coefficient (S) and the electronic thermal conductivity (κ_e) are given by [86]–[88]

$$\sigma = q_0^2 \int_{-\infty}^{\infty} dE \left(-\frac{\partial f}{\partial E} \right) \Xi(E) \tag{6.1}$$

$$S = \frac{q_0 k_B}{\sigma} \int_{-\infty}^{\infty} dE \left(-\frac{\partial f}{\partial E} \right) \Xi(E) \left(\frac{E - E_F}{k_B T} \right) \tag{6.2}$$

$$\kappa_e = k_B^2 T \int dE \left(-\frac{\partial f}{\partial E} \right) \Xi(E) \left(\frac{E - E_F}{k_B T} \right)^2 - \sigma S^2 T \tag{6.3}$$

The quantity $\Xi(E)$ is called the transport distribution function and is defined as

$$\Xi(E) = v^2(E)\tau(E)g(E) \tag{6.4}$$

where v is the bandstructure velocity, τ is the relaxation time and g is the density of states. Here we use the 3D density of states under an isotropic parabolic band approximation:

$$g(E) = \frac{m^{*3/2}}{\pi^2 \hbar^3} \sqrt{2(E - E_{C/V})} \tag{6.5}$$

where $E_{C/V}$ is the conduction/valence band edge.

Acoustic-phonon deformation potential (ADP) scattering is considered under a relaxation time approximation, according to

$$\frac{1}{\tau} = \frac{\pi D_A^2 k_B T}{\hbar c_l} g(E) \tag{6.6}$$

where we use D_A = 5 eV for the acoustic deformation potential as in typical semiconductors, and c_l=1.908×10$_{11}$ kgm$_{-1}$s$_{-2}$ is the elastic constant [85].

Ionized impurity scattering (IIS) is included according to the Brooks-Herring model:

$$\tau = \frac{16\sqrt{2m^*}\pi\varepsilon_r^2\varepsilon_0^2}{N_I q^4}[\ln(1+\gamma^2) - \frac{\gamma^2}{1+\gamma^2}]^{-1} E^{3/2} \tag{6.7}$$

where ε_r is the relative permittivity, ε_0 is the permittivity of free space, N_I is the density of impurities and $\gamma^2 \equiv 8m^* E L_D^2/\hbar^2$ where

$$L_D = \sqrt{\frac{\varepsilon_r\varepsilon_0 k_B T}{q_0^2 N_I}} \tag{6.8}$$

is the Debye screening length [85].

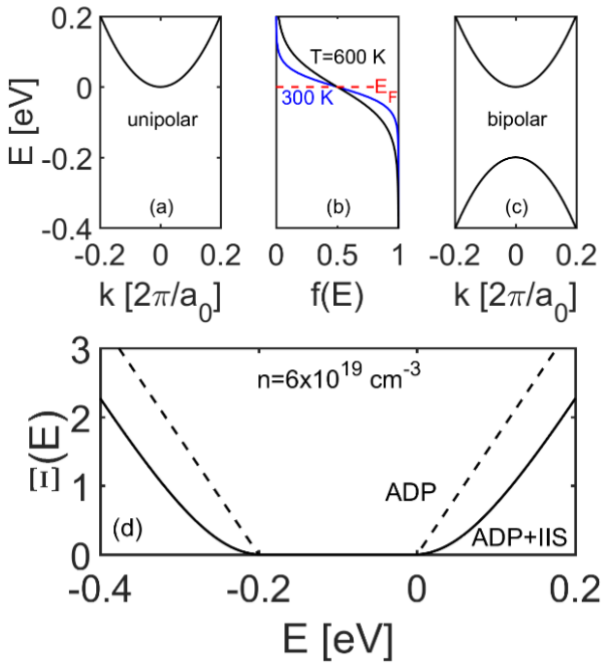

Fig. 6.1: (a) The unipolar case: a single parabolic conduction band with effective mass $m_C = m_0$ and conduction band edge E_C = 0 eV, (b) the Fermi distribution at T = 300 K (blue line) and T = 600 K (black line) with E_F = 0 eV (red-dashed line), and (c) the bipolar case: a single parabolic conduction band with effective mass $m_C = m_0$ and E_C = 0 eV and a single parabolic valence band with effective mass $m_V = m_0$ and E_V = -0.2 eV. In (d) we show the transport distribution function verses energy for the bipolar material for two different scattering regimes: acoustic phonon scattering (dashed line), and acoustic phonon scattering and ionized impurity scattering for an impurity density of n = 6×10$_{19}$ cm$_{-3}$ (solid line).

6.3 Results

Most thermoelectric materials have complex bandstructures and even more complex scattering mechanisms, however, in this study we only employ the single band effective mass approximation, which can give us simple first order guidance towards doping optimization in bipolar materials, putting aside complexities that arise from multi-band features.

We begin by 'scanning' the Fermi level, E_F, across the unipolar and the bipolar bandstructure materials in order to identify the optimal values of the power factors and *ZT* and the optimal positioning of the Fermi level (meaning that we compute the thermoelectric coefficients for a series of E_F values, each E_F corresponding to a specific doping concentration). We first consider the case in which transport is limited by acoustic phonon scattering (ADP) and then include ionized impurity scattering in addition (ADP+IIS). As we will show, the observations are different in the two cases.

In Fig. 6.2a and b we show the *PF* versus E_F for (a) the unipolar case, and (b) the bipolar case under ADP limited scattering at four different temperatures: T = 300 K (blue lines), T = 400 K (green lines), T = 500 K (red lines), T = 600 K (black lines). In the unipolar case it can be seen that the *PF* peaks just above the band edge (at approximately E_C= 0 eV) as previously suggested in earlier studies [130]. The Fermi level value at which this occurs increases linearly with temperature (a small shift only is evident here since the transition happens around 0 eV), but the peak *PF* remains constant. This behaviour will be discussed in more detail later. In the bipolar case (Fig. 6.2b) the *PF* peak for both bands moves even further into the band with increasing temperature. A small decrease is also unavoidable as the increasing contribution of holes from the valence band reduces *S*. Importantly, however, the *PF* peaks in both cases are spread over increasingly wider E_F values with increasing temperature (the black lines are broader compared to the blue lines), meaning that the power factor is somewhat more resilient to changes in carrier concentration at higher temperatures. In Fig. 6.2c we show *ZT* versus E_F for the bipolar case only (considering only κ_e, with κ_l = 0 for brevity, but which allows us to observe the peaks limiting case at very low κ_l versus the limit of large κ_l, which follows the power factor trend). We do not show the unipolar case since, because $\kappa_e \propto \sigma$ in the non-degenerate limit, the quantity

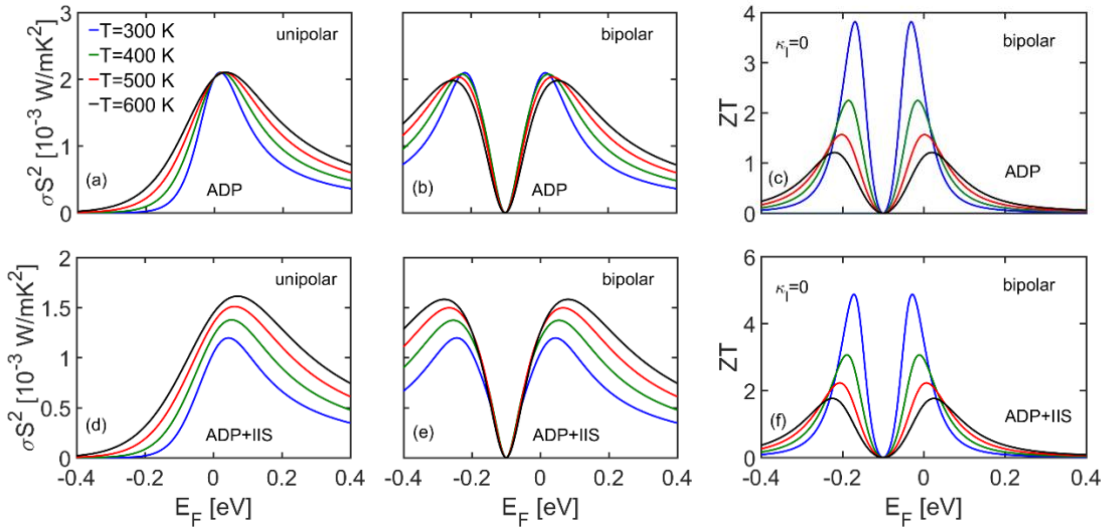

Fig. 6.2: The power factor versus Fermi level at four different temperatures: 300 K (blue lines), 400 K (green lines), 500 K (red lines), 600K (black lines) for (a) a single parabolic conduction band with E_C = 0 eV and m_C = m_0, under acoustic phonon scattering conditions (ADP), (b) a bipolar system with one parabolic conduction band with E_C = 0 eV and m_C = m_0, and one parabolic valence band with E_V = -0.2 eV and m_V = m_0 under acoustic phonon scattering conditions, (d) a single parabolic conduction band with E_C = 0 eV and m_C = m_0, under acoustic phonon and ionized impurity scattering conditions (ADP+IIS), and (e) a bipolar system with one parabolic conduction band with E_C = 0 eV and m_C = m_0, and one parabolic valence band with E_V = -0.2 eV and m_V = m_0 under acoustic phonon and ionized impurity scattering conditions. In (c) and (f) we show ZT (with κ_l = 0) versus Fermi level for the same four temperatures, and for ADP, and ADP+IIS conditions, respectively.

$ZT = \frac{\sigma S^2}{\kappa_e}$ diverges at low carrier concentrations, following the rise in S. In the bipolar case the peak occurs closer to the midgap than when the PF only is considered, although it also then rises more quickly with temperature as discussed later.

Although we considered ADP scattering alone, the high carrier concentration in TE materials is achieved by impurity doping, which introduces a strong, possibly dominant scattering mechanism in common semiconductors. Therefore, in Figs. 6.2d-f we further show the same three Fermi 'scans' in the presence of *both* acoustic phonon scattering and ionized impurity scattering (indicated as ADP+IIS). The introduction

of an additional scattering mechanism reduces the power factor. However, as the temperature rises, in the ADP+IIS case the peak power factor value now increases with temperature in both the unipolar and bipolar cases. In the case of optimizing *ZT*, the peaks again occur closer to the midgap (as in the ADP limited results), however the peak values are now higher in value. This is because, as seen in the transport distribution function shown in Fig. 6.1d, the introduction of the IIS affects low energy electron more heavily than higher energy electrons. Since the Seebeck coefficient is proportional to the average energy of the current flow as $S \propto \langle E \rangle - E_F$ this results in an increase in the Seebeck coefficient (comparing at a fixed E_F). In addition, this also results in a widening of the 'effective transport bandgap' (although these states are available they contribute significantly less to transport). This then results in a decrease in the bipolar effect giving an additional increase to *S* as well as a reduction in κ_e. Hence the values of *ZT* increase with the addition of IIS.

6.3.1 Temperature dependent properties

To show the behaviour of the power factor as the temperature rises, we next take the bandstructures we consider with carrier concentration optimized at $T = 300$ K and examine how the thermoelectric coefficients change when that carrier concentration is kept fixed at the $T = 300$ K optimal value. This is in order to replicate the constant doping concentrations found in experimental set-ups. Figure 6.3 shows σ, *S* and *PF* versus *T* for the unipolar (red lines) and bipolar (black lines) bandstructures for the cases of acoustic phonon scattering only (ADP, dashed lines) and acoustic phonon plus ionized impurity scattering (ADP+IIS, solid lines). Note that the optimal carrier concentration is different in the case of ADP and ADP+IIS situations, $n = 3\times10^{19}$ cm^{-3} and $n = 6\times10^{19}$ cm^{-3}, respectively. As the temperature increases and the Fermi distribution broadens, E_F drops in order to satisfy charge neutrality. The E_F decrease is limited in the bipolar case due to the increasing contribution of holes to the total carrier concentration, which counteract the downshift of the E_F. The electrical conductivity decreases with temperature for two reasons: i) the acoustic phonon scattering strength is proportional to *T* (see Eq. (6.6)), ii) E_F moves towards the midgap meaning lower velocity states are participating to transport. In the unipolar case (red lines), the Seebeck coefficient shows an increase with *T* since it is proportional to the

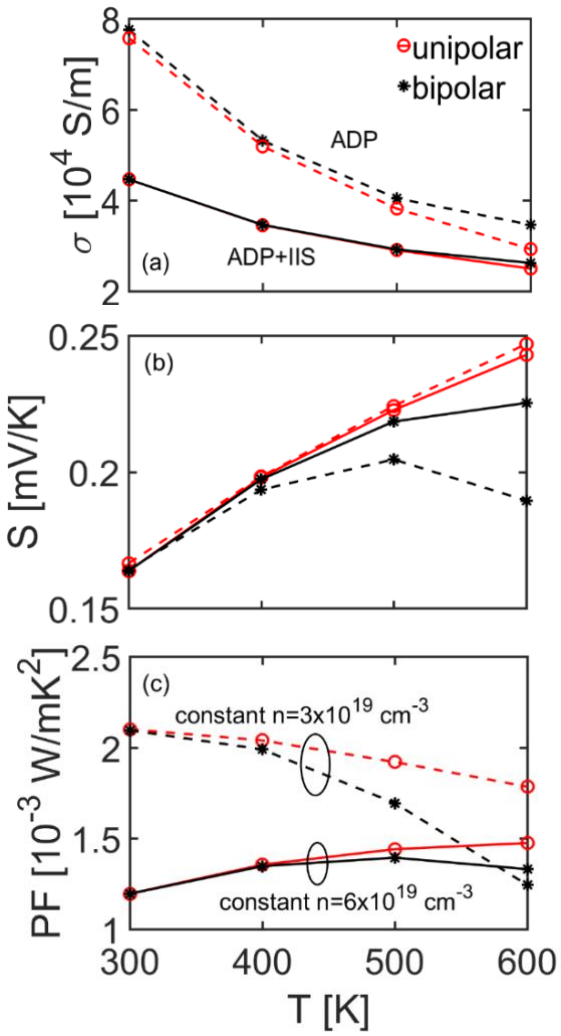

Fig. 6.3: The (a) electrical conductivity, (b) Seebeck coefficient, and (c) power factor versus temperature at constant carrier concentration for two bandstructures: a single parabolic conduction band of mass $m_c = m_0$, (red lines), and a bipolar system with one conduction and one valence band with masses $m_c = m_0$, $m_v = m_0$ (black lines), and bandgap E_g = 0.2 eV. Results are shown for acoustic phonon scattering, ADP, only (dashed lines), and for acoustic phonon and ionized impurity scattering, ADP+IIS (solid lines).

difference between the average energy of the current and the Fermi level, $S \propto \langle E \rangle - E_F$. The quantity $\langle E \rangle - E_F$ increases in the unipolar case due to the significant drop in E_F with T. In the bipolar case, however, the Seebeck coefficient increases to a lesser extent compared to the unipolar case (and even eventually begins decreasing) due to the increase in holes which contribute to S with opposite sign to the

electrons. The resultant effect on the power factor from these behaviours is: i) in the unipolar ADP case (red dashed line), a decrease of ~15% from 300 K to 600 K is observed, ii) in the bipolar ADP case (black dashed line), despite the smaller reduction in σ at 600 K from the extra contribution to current that the valence band provides, there is an overall degradation in the power factor by ~40% which is much more significant than in the unipolar case.

With the introduction of IIS for both unipolar and bipolar channels, σ naturally drops due to the extra scattering rate. However, as expected, at higher temperatures this drop is not as substantial as in the ADP case as the IIS scattering typically weakens with temperature. This is due to the broadening of the Fermi distribution (see Fig. 6.1b) and the occupation of higher energy states with larger wavevectors which are less impacted by IIS. This can again be seen from the IIS stronger impact on the transport distribution function at lower energies in Fig. 6.1d. The improvement in σ from the valence band contribution in the ADP case in the bipolar channel (comparing red-dashed to black-dashed lines in Fig. 6.3a) is now also missing in the ADP+IIS lines due to the widening of the 'effective transport bandgap' that IIS causes as explained earlier, and effectively makes the material 'look' more unipolar (Fig. 6.2d).

When it comes to the Seebeck coefficient in Fig. 6.3b and the introduction of IIS, bipolar transport no longer has such a strong effect on S with increasing temperatures, due to this widening of the 'effective transport bandgap' due to IIS, unlike in the ADP-limited case (black-solid versus black-dashed line in Fig. 6.3b). The result of these effects on the PF, therefore, is a significant reduction at low temperatures compared to the ADP-limited case, but an increase with temperature (Fig. 6.3c). The increase is a consequence of the smaller relative reduction in σ and the continuous rising of S.

Figure 6.3 showed and explained why the power factor drops (in the ADP case) or increases less that its optimal value if the carrier concentration (controlled by doping) remains at the T = 300 K optimal levels. We now show that the power factor can be improved by a careful optimization of the carrier concentration at higher temperature operations. In Fig. 6.4a we show the optimal PF of the unipolar (red lines) and bipolar (black lines) bandstructures for the cases of ADP scattering only (dashed lines) and ADP+IIS (solid lines), i.e. the peaks of the Fermi scans seen in Fig. 6.2.

For ADP scattering only, whereas the unipolar system previously saw a reduction of ~15%, by optimizing the doping with temperature the power factor now remains constant (Fig. 6.4a – red-dashed line). In the bipolar case the dramatic fall in the power factor due to the Seebeck reduction (as seen previously in Fig. 6.3b, black-dashed line) is mitigated by increasing the Fermi level. Consequently the power factor, although still slightly decreasing with temperature, is now ~60% higher at 600 K than in the un-optimized case from Fig. 6.3c (un-optimized values from Fig. 6.3c shown by the square markers at 600 K in red (unipolar) and black (bipolar).

The Fermi level required to produce these optimal values rises linearly with temperature in the unipolar system (red-dashed line in Fig. 6.4b). This behaviour was earlier identified by Ioffe in Ref. [82] where it was shown that the optimal reduced Fermi level $\eta_{F,opt} = (E_F - E_C)/k_B T = r$, where r is an exponent that depends on the electron scattering mechanism. Since r is a constant, this gives $E_F \propto T$. In our case of acoustic phonon scattering $r = 0$, so we would expect the power factor to peak at the band edge. However, Ioffe's derivation assumes Boltzmann statistics for the carrier distribution and, indeed, running our calculations under that assumption reproduces such a result (not shown). However, using the more accurate for degenerate doping conditions Fermi-Dirac distribution, we find that in the case of acoustic phonon scattering $\eta_{F,opt} \approx 2/3$. In the bipolar system the linear behaviour seen in the unipolar case no longer holds, and the optimum Fermi level rises quicker than linearly (black-dashed line in Fig. 6.3b). This is in order to avoid the detrimental impact of the bipolar effect that the valence band introduces.

In Fig. 6.4c we also show the optimal carrier concentration required to set E_F at the optimal position. As has been previously identified in the literature [82], [131], the optimal carrier concentration in a unipolar system increases as $n_{opt} \propto T^{3/2}$ (red-dashed line). Again, however, in the bipolar system (black-dashed line) the unipolar behaviour no longer holds, and the required carrier concentration rises more quickly in order to produce the higher Fermi levels seen in Fig. 6.4b, following an approximate $T^{1.8}$ trend. Indeed, at T = 600 K the optimal bipolar carrier concentration is 30% higher than the optimal unipolar carrier concentration.

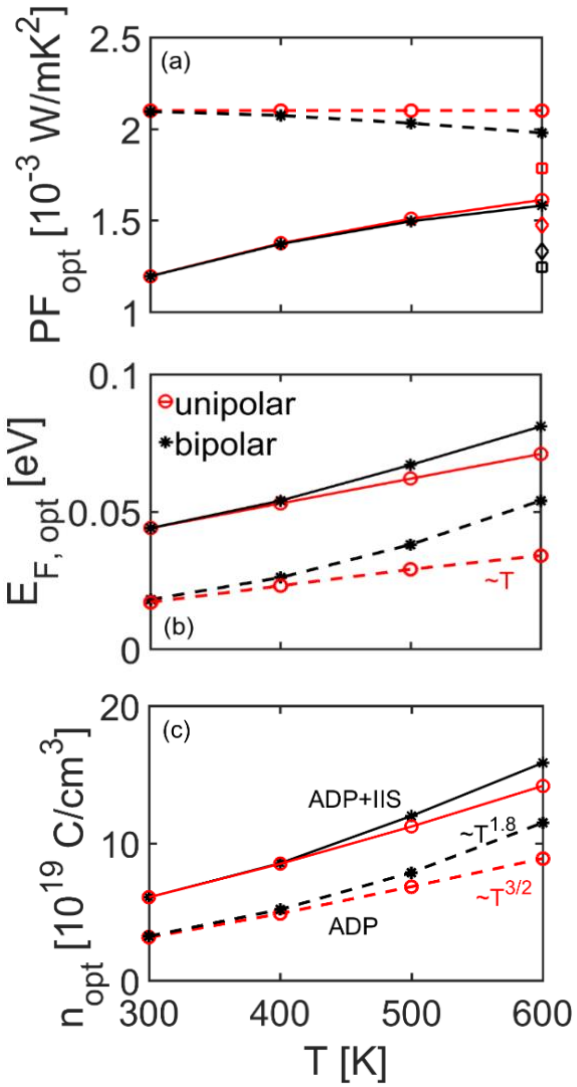

Fig. 6.4: The optimal values of (a) the power factor, (b) Fermi level, and (c) carrier concentration versus temperature for two bandstructures: a single parabolic conduction band of mass $m_c = m_0$, (red lines), and a bipolar system with one conduction and one valence band with masses $m_c = m_0$, $m_v = m_0$ (black lines), and bandgap $E_g = 0.2$ eV. Results are shown for acoustic phonon scattering only, ADP (dashed lines), and for acoustic phonon and ionized impurity scattering, ADP+IIS (solid lines).

When IIS is included, the power factor values are lower as explained previously, but increase with increasing temperature due to the occupation of higher energy states which scatter less under IIS. Benefits compared to the un-optimized values (diamond markers in Fig. 6.4a) are not as great as in the ADP only case, but still significant – 10% for the unipolar bandstructure and 20% for the bipolar

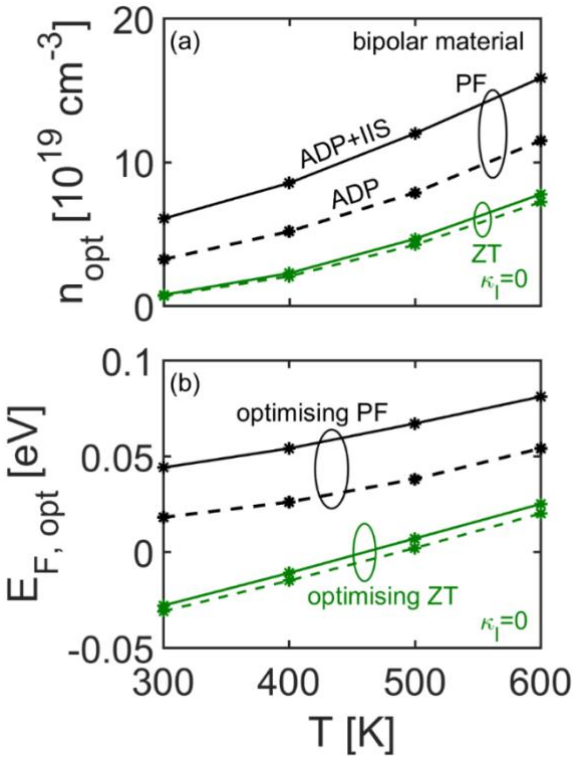

Fig. 6.5: The optimal values of (a) carrier concentration and (b) the Fermi level versus temperature for a bipolar bandstructure to maximize the power factor (black lines) and *ZT* (green lines) in the case of acoustic phonon scattering only, ADP (dashed lines) and acoustic phonon and ionized impurity scattering, ADP+IIS (solid lines).

bandstructure (solid lines in Fig. 6.4a). The Fermi level and carrier concentration values needed to achieve these power factor values are higher than in the ADP only case. For practical purposes, therefore, to achieve an optimized power factor in the bipolar case at T = 600 K in the material we consider of bandgap E_g=0.2 eV, the doping concentration needs to be by 160% higher compared to the value that provides optimized *PF* at T = 300K. That value is by 10% higher compared to the one that achieves the optimal T = 600 K *PF* in the unipolar case. Note that in the case of the ADP+IIS transport conditions, the optimal doping density is higher, due again to the widening of the 'effective transport bandgap' seen in Fig. 6.1d. Also note that these values are to be altered in the case of a different bandgap, i.e. the relevance of these values are shifted to lower/higher temperatures as the bandgap decreases/increases.

Finally, due to the influence of the thermal conductivity in the denominator of *ZT*, which has its own temperature dependence, *ZT* does not peak at the same E_F or carrier concentration as the *PF*. Therefore, in Fig. 6.5 we compare the optimal carrier

concentration and Fermi levels when optimizing for the power factor (same black lines as in Fig. 6.4b and c) and optimizing for *ZT* (green lines). This comparison here is shown only for the bipolar material since the unipolar material does not show a peak as explained previously. For the calculation of *ZT* we consider only the electronic properties (i.e. we take $\kappa_l = 0$, as the behaviour of κ_l is material dependent and more complex). Since $\kappa_e \propto \sigma$ through the Lorenz number, κ_e is reduced with falling E_F and, therefore, the peaks in *ZT* occur at significantly lower density and E_F than when just optimizing for the *PF*. As the temperature is increased, however, the optimal values (in both ADP and ADP+IIS cases) rise at a quicker pace than when optimizing for *PF*. This is because as the temperature increases the impact of the bipolar effect kicks in and κ_{bi} increasingly pushes the peak away from the midgap. The introduction of IIS, however**,** when optimizing for *ZT* has much less influence than in when optimizing for the *PF*. This is again due to κ_e being proportional to σ. As can be seen in Fig. 6.3, the introduction of IIS primarily affects σ. When optimizing for *ZT*, this impact is then cancelled out by the same impact on κ_e.

Of course in a real material $\kappa_l \neq 0$ and the optimal *ZT* values will lie somewhere between the *PF*-optimized and our $\kappa_l = 0$ *ZT*-optimized values. In particular, it is interesting to note that the smaller the value of κ_l in the material with respect to the κ_e, the closer it is to the $\kappa_l = 0$ *ZT*-optimized case, and therefore the less it needs to be doped to reach its optimal *ZT*, which can prove helpful for TE materials, as doping at extremely high values can prove difficult in many cases.

Finally, we would like to state that in this work we employed a simple two-band parabolic model to obtain first order optimization strategies for doping in bipolar TE materials. In reality, material bandstructures are typically more complex than the simple two-band parabolic model we assume here. Real material bandstructures can have a variety of band gaps, effective masses, band degeneracies, band non-parabolicity, and multiple valence and/or conduction bands. Many of these bandstructure features can also vary with temperature, and detailed studies on each material are essential for proper optimization. In this study however, it was our aim to demonstrate to first order the important, yet overlooked, impact of the bipolar effect on the doping optimization.

6.4 Conclusions

Using the Boltzmann transport formalism we have calculated the thermoelectric transport coefficients for unipolar and bipolar systems and presented a study on the optimal doping conditions for the power factor and *ZT* figure of merit. We have shown that if the carrier concentration is not properly optimized at the temperature of operation, but room temperature optimal doping is considered, the power factor can underperform by 15% in the unipolar systems, and 40% in the bipolar system under ADP scattering, and 10% in the unipolar systems, and 20% in the bipolar system under ADP+IIS scattering. Consequently, significant enhancements in the *PF* (~40%) can be achieved through doping optimization. Furthermore we have identified that in a bipolar system the optimal carrier concentration indicates an approximately $T^{1.8}$ trend, larger compared to the $T^{3/2}$ trend in unipolar materials, a result of the additional degradation due to bipolar transport. In our simulations, the optimal carrier concentration at T = 600 K in a material with bandgap E_g = 0.2 eV (e.g. approximately that of Bi_2Te_3) then becomes 30% larger than expected from the unipolar calculation. We believe that our findings will be useful in the optimal design of bipolar thermoelectric materials.

VII. Effectiveness of nanoinclusions for reducing bipolar effects in thermoelectric materials

7.1 Introduction

As discussed in chapter 6, many traditional and contemporary TE materials suffer from narrow bandgaps making them susceptible to bipolar effects at high operating temperatures. In order to reduce the bipolar effect, minority carriers need to be blocked, e.g. using heterostructure designs [116], [127], band engineering to widen the bandgap [128], [129], grain boundaries with barriers for minority carriers [8], etc.

One of the most commonly employed methods for the reduction in the lattice thermal conductivity, κ_l, on the other hand, has been the use of nanoinclusions (NIs) [6], [35]–[37], [50], [60], which could be experimentally easier to realize compared to heterostructures. As discussed in chapters 3-5, NIs are highly effective at reducing the lattice thermal conductivity κ_l arising due to phonon transport. At high temperatures, however, κ_l is typically reduced naturally due to enhanced phonon-phonon scattering. In the most widely used thermoelectric materials it is the emergence of the κ_{bi}, a term that arises from electronic transport, which adds a significant contribution to the total thermal conductivity and degrades performance. Since NIs also influence the electronic transport, it seems pertinent to ask whether they can also reduce the bipolar effect, and whether in that way it is possible to achieve simultaneous reductions in κ_l, $\kappa_{el,tot}$, and κ_{bi}. To accurately examine this, however, advanced simulations are needed, which capture all geometrical complexities (non-uniform structures, mixing low-dimensional NIs with higher-dimensional bulk regions), as well as all transport physics at the nanoscale (quantum reflections, interferences, quantization, quantum tunnelling etc.) [132].

To explore this possibility we simulate structures where the NIs introduce barriers on the valence band without introducing barriers on the conduction band. Experimentally this can be achieved through careful selection of the conduction and valence band offsets (as suggested in Ref. [53]) and, if needed, through further band engineering via e.g. alloying.

In this chapter we use the quantum mechanical non-equilibrium Green's function (NEGF) formalism, including electron-phonon interactions, which can accurately capture the important details specified above, to calculate the thermoelectric transport coefficients of bipolar systems embedded with nanoinclusions. We identify the conditions for which the bipolar effect is most significant, and those for which nanoinclusions are most effective at reducing it. We then employ literature thermal conductivity data for a series of materials to estimate the overall improvement in the *ZT*. The chapter is organized as follows: In Section II we explain the simulation method we employ and describe the geometries we consider. In Section III we present and discuss our results, and finally in IV we conclude.

7.2 Approach

We employ the NEGF formalism as outlined in chapter 2 to compute electronic transport, including interactions of electrons with acoustic phonons (acoustic phonon scattering). The simulated system is a 2D channel described using the effective mass approximation. The effective mass is considered uniform throughout the channel, including for the nanoinclusions, although this mass is altered to consider non-symmetric conduction and valence bands. The nanoinclusions are modelled as cylindrical potential energy barriers in the valence band as shown in Fig. 7.1. We consider barrier heights of V_B = 0.2 eV and barrier diameters of d = 3 nm. The system dimensions we simulate are width W = 30 nm and length L = 60 nm. Acoustic phonon scattering is considered and the strength of the electron-phonon coupling is such that an electronic mean-free-path (MFP) of 15 nm at T = 300 K is achieved, meaning we have diffusive transport in the channel. Note that from scattering theory, we know that the rate is proportional to the temperature as: $1/\tau = \pi D_A^2 k_B T g(E)/\hbar c_l$ where D_A is the acoustic deformation potential, k_B is the Boltzmann constant, $g(E)$ is the density of states, $\hbar$ is the reduced Planck constant, and c_l is the material's elastic constant [85]. Thus, our calibrated MFP of 15 nm only holds at T = 300 K and will decrease linearly with increasing temperature in the simulations we consider below. In all cases, however, the distance between NIs, as shown in Fig. 7.1, is similar to our nominal electron-phonon scattering MFP at room temperature. We select this on purpose so that NIs have a significant influence on the transport properties.

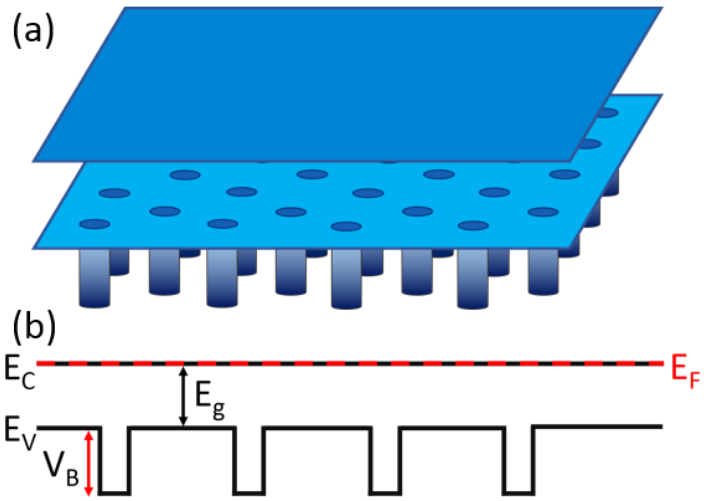

Fig. 7.1: (a) A schematic of the potential energy in the 2D channel considered. Nanoinclusions are modelled as cylindrical potential barriers for the minority carriers in the valence band, but do not affect the majority carriers in the conduction band. (b) A 1D schematic identifying the key parameters of the system: the conduction band minimum, E_C; the valence band maximum, E_V; the bandgap, E_g; the nanoinclusion barrier height, V_B; and the Fermi level, E_F, which here is aligned with the E_C.

For each case considered, the conduction and valence bands are simulated separately (i.e. we simulate a single band in NEGF) and then combined as described below. The total electrical conductivity, total Seebeck coefficient, total electronic thermal conductivity, individual band electronic thermal conductivities, and bipolar thermal conductivity, are evaluated by [83], [116]:

$$\sigma = \sigma_e + \sigma_h \tag{7.1}$$

$$S = \frac{\sigma_e S_e + \sigma_h S_h}{\sigma_e + \sigma_h} \tag{7.2}$$

$$\kappa_{el,tot} = \kappa_{el,e} + \kappa_{el,h} + \kappa_{bi} \tag{7.3}$$

$$\kappa_{el,e/h} = \frac{1}{q^2 T}\int \sigma(E)(E - E_F)^2 dE - \sigma_{e/h} S_{e/h}{}^2 T \tag{7.4}$$

$$\kappa_{bi} = \frac{\sigma_e \sigma_h}{\sigma_e + \sigma_h}(S_e - S_h)^2 T \tag{7.5}$$

where the subscripts ‘e’ and ‘h’ indicate the contributions from electrons and holes respectively, q is the elementary charge, E is energy, and E_F is the Fermi level. Note that S_e and S_h have opposite signs and therefore the total Seebeck coefficient, S, is

reduced when both bands contribute to the transport (thereby taking into account electron-hole recombinations), normally also reducing the power factor despite any gains in σ. Similarly, κ_{bi} is maximized when both bands contribute to carrier transport, often when the Fermi level is placed in the midgap. It should also be noted that κ_{bi} is a conductivity-limited quantity, and is primarily determined by the conductivity of the minority carrier (the smaller of the two as seen by the right term in Eq. (7.5)) [100]. This can be seen from its physical origin of electron-hole recombinations in the contacts [124]. Increasing an already large flow of electrons will not increase electron-hole recombinations if there are no further holes to recombine with, but an increase in hole flow would produce a similar increase in the electron-hole recombination rate. Note, also, that although the conductivities σ and κ are used in the equations above, due to the 2D nature and finite channel length of our NEGF simulations, we extract the conductances, G and K, and it is understood in the analysis that follows that σ and κ, and G and K can be used interchangeably.

We consider a matrix material with bandgap E_g = 0.2 eV, similar to that of Bi_2Te_3 for example. We place the Fermi level in alignment with the conduction band edge as this will provide optimal power factors, at least in a unipolar material [130]. We then insert a dense network of nanoinclusions as in Fig. 7.1 by the introduction of potential barriers in the valence band, but allow perfect band alignment in the conduction band (a successful power factor and ZT improvement strategy outlined in Ref. [53] for the case of SrTe inclusions in PbTe**)**. Just by looking at Eqs. (7.1)-(7.5), it is obvious that the higher the hole conductivity, then: i) the higher the overall electronic conductivity, ii) the lower the overall Seebeck coefficient, and iii) the higher the bipolar conductivity. We therefore would like to answer the question: how effective are nanoinclusion induced barriers in the valence band at reducing bipolar effects? In addition, in the light of the complexity in the bandstructures of new generation TE materials: under what bandstructure conditions is the use of such nanostructuring most effective?

7.3 Results and Discussion

To see the effect of bandstructure in a simplified manner, we begin our investigation by considering the influence of different effective masses, lighter and heavier (which provide different electronic mean-free-paths and conductivities) and

the influence of valence band nanostructuring on the bipolar and electronic thermal conductivity. Figures 7.2a-b show the four bandstructures we consider with effective masses as follows: $m_c = m_0$, $m_v = m_0$ (green-cross lines); $m_c = m_0$, $m_v = 0.5m_0$ (red-square lines); $m_c = 0.5m_0$, $m_v = m_0$ (blue-star lines); $m_c = 0.5m_0$, $m_v = 0.5m_0$ (black-circle lines), where m_c is the conduction band effective mass, m_v is the valence band effective mass, and m_0 is the electron rest mass. In each case the Fermi level coincides with the conduction band minimum, i.e. $E_F = 0$ eV (red-dashed line in Fig. 7.2a). Our intent here is to explore the qualitative effect of conduction/valence band symmetry and asymmetry in bipolar transport, i.e. with respect to different combinations of light/heavy effective masses.

In Fig. 7.2c-d, we show the bipolar electronic thermal conductivity, κ_{bi}, versus temperature for each bandstructure. In each case we consider structures without NIs (solid lines) and with NIs (dashed lines), which introduce barriers in the valence band. For all bandstructure examples κ_{bi} increases with temperature, as expected, due to the broadening of the Fermi distribution that begins to pick up carriers from the valence band. The largest bipolar effect can be seen in the high conduction cases when the effective masses are smaller. Particularly important is the influence of a light valence band (red and black solid lines). This is because (as shown earlier by Eq. (7.5)) the conduction of the minority band, which has a significantly smaller value, is dominant in determining κ_{bi}. Upon nanostructuring (dashed lines), the relative reduction in κ_{bi} however, is also larger in the case where the masses are smaller and will be discussed in more detail later.

In Fig. 7.2e-f we show the corresponding total electronic thermal conductivities, $\kappa_{el,tot}$. Again all bandstructures show an increase in $\kappa_{el,tot}$ with temperature. At low temperatures $\kappa_{el,tot}$ is dominated by $\kappa_{el,e}$, the contribution from the conduction band, since we are close to degenerate carrier concentration conditions (E_F is at E_C). At higher temperatures, however, the contribution of κ_{bi} becomes important, fuelled mostly from light valence bands, which add more significantly to minority carrier transport. Thus, in the light band case of Fig. 7.2e (black line) a larger increase in $\kappa_{el,tot}$ is observed. Likewise, in the cases of asymmetric masses between the conduction and valence band in Fig. 7.2f, although the *heavy*-conduction-*light*-valence bandstructure (red-solid line) starts lower compared to the *light*-conduction-*heavy*-valence bandstructure case (blue-solid line), at higher temperatures the two merge. With the introduction of NIs, both the κ_{bi} and $\kappa_{el,tot}$ are reduced (dashed lines in Fig.

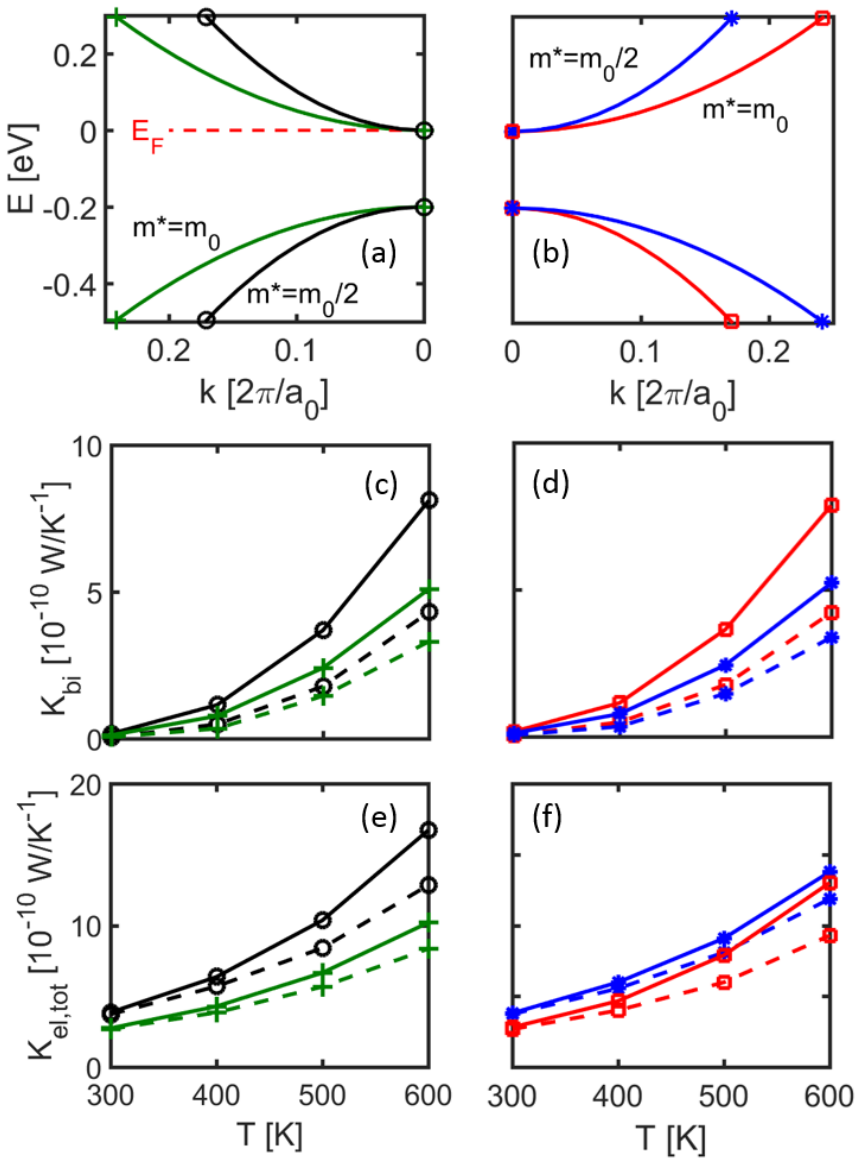

Fig. 7.2: (a) The symmetrical bandstructures: $m_c = m_0$, $m_v = m_0$ (green-cross lines); and $m_c = 0.5m_0$, $m_v = 0.5m_0$ (black-circle lines). (b) The asymmetrical bandstructures: $m_c = m_0$, $m_v = 0.5m_0$ (red-square lines); and $m_c = 0.5m_0$, $m_v = m_0$ (blue-star lines). (c) The bipolar thermal conductivity versus temperature for the symmetrical bandstructures. (d) The bipolar thermal conductivity versus temperature for the asymmetrical bandstructures. (e) The total electronic thermal conductivity versus temperature for the symmetrical bandstructures. (f) The total electronic thermal conductivity versus temperature for the asymmetrical bandstructures. Results are shown for structures with (dashed lines) and without (solid lines) nanoinclusions.

7.2), but the light valence mass cases are reduced much more, something we discuss below in more detail.

We now proceed in similarly analyzing the effect of the different band masses and of valence band nanostructuring on the rest of the thermoelectric coefficients: the conductance, G, the Seebeck coefficient, S, and the power factor, PF defined as GS^2, versus temperature (shown in Fig. 7.3). We use the same four bandstructures shown in Fig. 7.2a-b. Since we are close to degenerate carrier concentration conditions, G is dominated in all cases by the effective mass of the conduction band (meaning the NIs on the valence band have little influence on G) and shows a small increase with temperature (Fig. 7.3a-b). Note that we use a fixed Fermi level (E_F = 0 eV), so the increase in phonon scattering that would normally reduce conductance with increasing temperature is offset by an increase in the carrier concentration due to the broadening of the Fermi distribution. The Seebeck coefficient, however, slowly decreases with temperature since the valence band (which has opposite Seebeck sign) exponentially increases its contribution to transport (Fig. 7.3c-d). The reason the influence of temperature is more significant on S, is that although σ_e dominates σ_h, $\sigma_e S_e$ is relatively less dominant over $\sigma_h S_h$ as seen in Fig. 7.4, which shows that the ratios of G_e/G_h are significantly higher compared to the ratios of $G_e S_e/G_h S_h$. Therefore, from Eq. (7.1) and Eq. (7.2) it can be seen that the valence band has more influence on the total Seebeck than on the total conductance. Consequently, the introduction of NIs (dashed lines) on the valence band limits the contribution to transport and S is somewhat recovered (compare the dashed to the solid lines in Fig. 7.3c-d). These effects can be seen in the power factors in Fig. 7.3e-f as well, where the power factors partially recover with the introduction of NIs due to this recovery of S.

We now quantify the changes we observe in κ_{bi}, $\kappa_{el,tot}$, and the PF due to the introduction of NIs on the valence band for the four bandstructures shown in Fig. 7.2a-b. Figure 7.5 shows the percentage changes in these quantities with temperature. In Fig. 7.5a, for the κ_{bi}, it can be seen that at 300 K an initial reduction in κ_{bi} close to 80% is observed for the light valence band mass materials (red/black lines), and around 60% for the heavier mass ones. The percentage generally decreases with temperature, indicating that NIs are less effective in reducing κ_{bi} as the temperature increases. The reason for this can be seen from the NEGF resolved transmissions of the valence band (alone), the quantities we use to extract the valence band TE coefficients, which we

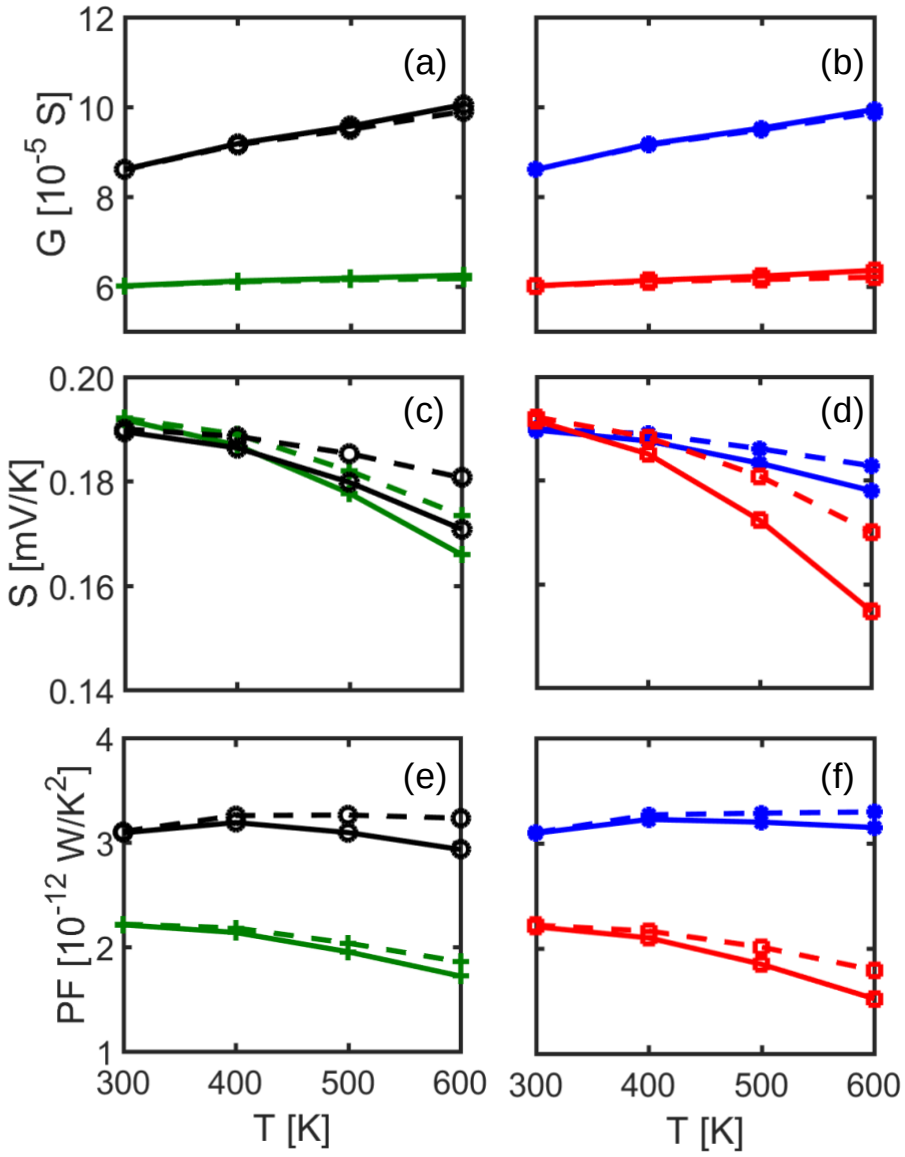

Fig. 7.3: The conductance, G, Seebeck coefficient, S, and power factor, $PF = GS^2$, versus temperature, T, for the four bandstructures shown in Fig. 2(a-b): $m_c = m_0$, $m_v = m_0$ (green-cross lines); $m_c = m_0$, $m_v = 0.5m_0$ (red-square lines); $m_c = 0.5m_0$, $m_v = m_0$ (blue-star lines); $m_c = 0.5m_0$, $m_v = 0.5m_0$ (black-circle lines). Results are shown for structures with (dashed lines) and without (solid lines) nanoinclusions.

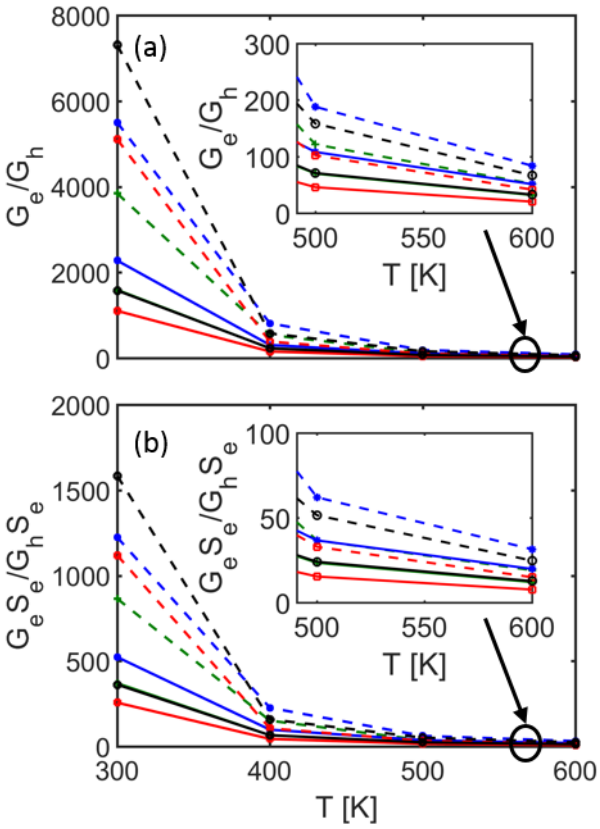

Fig. 7.4: (a) The ratio of the conduction band conductance, G_e, and the valence band conductance, G_h versus temperature. (b) the ratio G_eS_e/G_hS_h versus temperature. Results are for the four bandstructures shown in Fig. 2(a-b): $m_c = m_0$, $m_v = m_0$ (green-cross lines); $m_c = m_0$, $m_v = 0.5m_0$ (red-square lines); $m_c = 0.5m_0$, $m_v = m_0$ (blue-star lines); $m_c = 0.5m_0$, $m_v = 0.5m_0$ (black-circle lines), and for structures with (dashed lines) and without (solid lines) nanoinclusions.

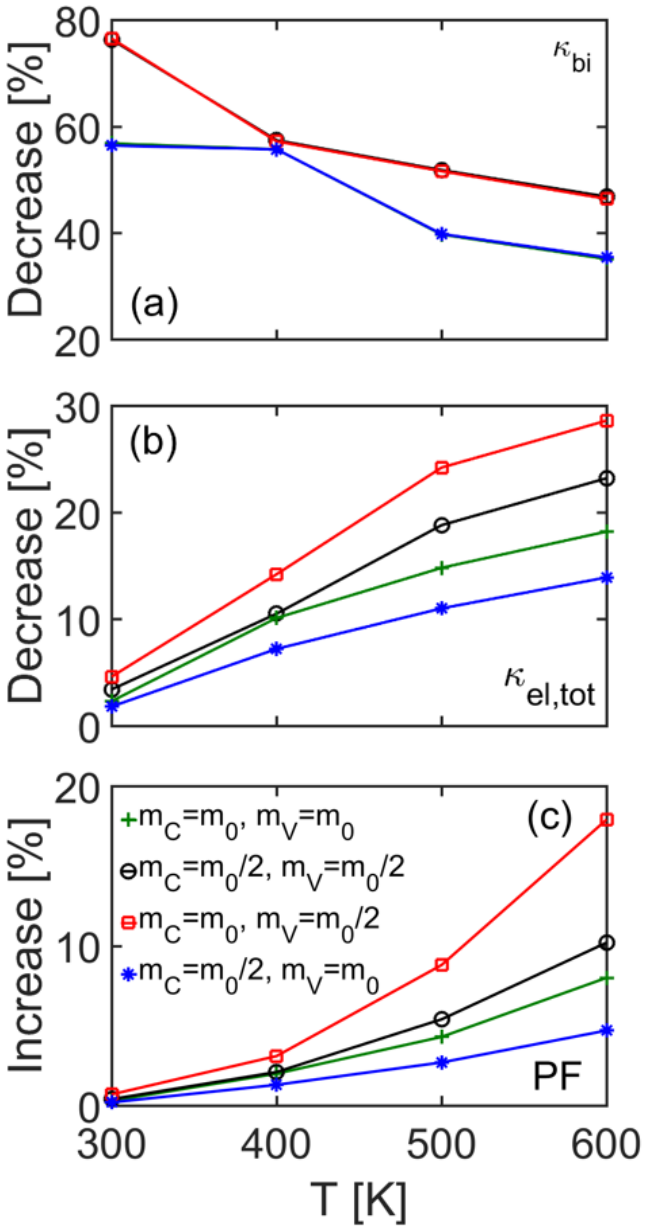

Fig. 7.5: (a) The percentage decrease in the bipolar thermal conductivity κ_{bi} due to the introduction of nanoinclusions on the valence band versus temperature for the four bandstructures shown in Fig. 2(a-b): $m_c = m_0$, $m_v = m_0$ (green-cross lines); $m_c = m_0$, $m_v = 0.5m_0$ (red-square lines); $m_c = 0.5m_0$, $m_v = m_0$ (blue-star lines); $m_c = 0.5m_0$, $m_v = 0.5m_0$ (black-circle lines), (b) The percentage decrease in the total electronic thermal conductivity $\kappa_{el,tot}$ versus temperature. (c) The percentage increase in power factor $PF = GS^2$ versus temperature.

show in Fig. 7.6. Note that the energy values are relative to the valence band edge (although plotted on the positive x-axis) and increase in value moving into the band. While the transmission of the pristine valence band reduces with increasing temperature due to the increasing phonon scattering rate previously mentioned (solid lines), the transmission of the structure with NIs remains largely unchanged with increasing temperature. This suggests that the scattering mechanism introduced by the NIs (in combination with phonon scattering) is somewhat less dependent on temperature at first order. As the temperature increases, the electron-phonon scattering limited transmission (solid lines) and the transmission of the valence band with NIs plus phonon scattering (dashed lines) begin to converge. This means the introduction of the NIs has a smaller effect on the valence band conductance at higher temperatures. The reduction of the percentage decrease in κ_{bi} can also be accounted for by κ_{bi} being dominated by the minority carrier conductivity, σ_h, as explained earlier. At lower temperatures σ_h is small compared to σ_e, and therefore dominates κ_{bi} (i.e. the right term in Eq. (7.5) changes more for smaller σ_h values). At higher temperatures σ_h begins to approach σ_e and so the reduction in σ_h from the NIs does not have as large a relative impact on κ_{bi}. However, this is only a relative effect - the absolute value of the κ_{bi} reduction at high T is much larger.

Despite this relative reduction in the influence of the NIs on $\kappa_{bi,}$ the overall impact on $\kappa_{el,tot}$ increases with temperature as shown in Fig. 7.5b. At lower temperatures $\kappa_{el,tot}$ is dominated by the conduction band $\kappa_{el,e}$ so reducing κ_{bi} does not have a significant impact. At larger temperatures, however, κ_{bi} becomes more significant (and becomes an increased proportion of $\kappa_{el,tot}$) and reducing it therefore has a larger impact on $\kappa_{el,tot}$. This effect is, however, counteracted by the NIs falling impact on κ_{bi} shown in Fig. 7.5a, and therefore the decrease begins to saturate at higher temperatures. Likewise, in Fig. 7.5c we see that the *PF* is also increasingly improved by the introduction of NIs with temperature in all bandstructure cases, an effect attributed to the increase in *S*. In a similar case to $\kappa_{el,tot}$, the valence band contribution to *S* becomes increasingly more significant at higher temperatures, and thus the influence of the NIs in reducing S_h increases likewise. The relative increase in the *PF* versus temperature between the pristine materials and those with NIs is continuously increasing (reaching even up to ~20% at 600 K), without any signs of saturation up to the temperatures we consider (in contrast to κ_{bi} and $\kappa_{el,tot}$). We stress that *PF* improvement value of 20% are quite significant for TE materials, which usually

experience only incremental changes upon the introduction of new concepts. The continuous improvement with temperature is because, as seen in Fig. 4, the quantity $\sigma_e S_e$ in Eq. (7.2) (for the overall Seebeck coefficient) becomes less dominant over $\sigma_h S_h$ as the temperature increases. This maintains the influence of the valence band (and consequently NIs) at higher temperatures for the overall Seebeck coefficient and the *PF*. Note the multiple effects at play here: κ_{bi} is determined primarily by the valence band due to Eq. (7.5) being multiplicative, but its influence decreases with temperature due to two reinforcing effects: i) σ_h begins to approach σ_e so the valence band (and the NIs) becomes less influential, and ii) the electron-phonon scattering increases (as acoustic phonon scattering rate is ~T), which makes the NIs relatively less influential as a scatterer. The *PF* on the other hand is determined primarily by the conduction band since Eqs. (7.1) and (7.2) are additive, and its influence increases with temperature according to two competing effects: i) σ_h begins to approach σ_e and $\sigma_h S_h$ is begins to approach $\sigma_e S_e$ so the valence band (and the NIs) become more influential, and ii) as before, the electron-phonon scattering increases, which makes the NIs become less influential. For the temperatures that we have considered, the first of these effects is dominant and the *PF* benefits due to the NIs increase with increasing temperature without saturating, but it could be possible that there is an upper limit at higher temperatures.

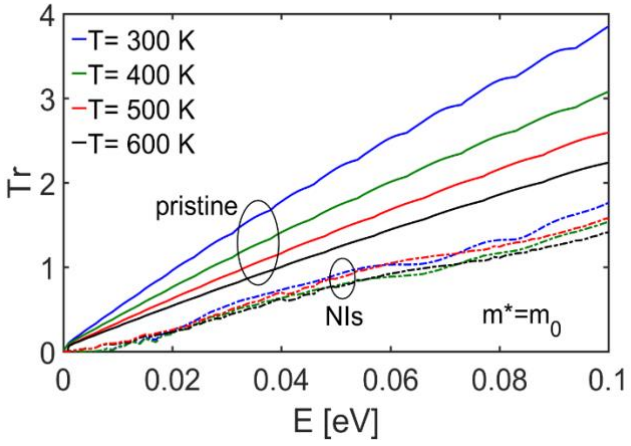

Fig. 7.6: The transmission versus energy of the $m_v = m_0$ valence band shown in Fig. 2(a) at four temperatures: 300 K (blue lines), 400 K (green lines), 500 K (red lines), 600 K (black lines); and for with (dashed-dotted lines) and without (solid lines) nanoinclusions. Note that the energy values are relative to the valence band edge and increase in value moving into the band.

An important observation here, is that the highest overall *PF* improvement is not found in the case where the band masses (especially that of the valence band) are low, i.e. their conductivity is high. The highest benefits on the *PF* of nanostructuring the valence band to reduce the bipolar effect come in the case where the valence/conduction band effective masses are asymmetric, with the valence mass larger than the conduction mass. In this case, with a factor of 2 asymmetry in the masses, the *PF* improvements at 600 K are nearly double compared to the symmetric low masses case. Despite the fact that the reduction in κ_{bi} is dominated by the valence band conductivity (black/red lines and green/blue lines of same valence band conductivity overlap in Fig. 7.5a), in the *PF* case, the more comparable to $\sigma_e S_e$ the term $\sigma_h S_h$ is, the largest the relative benefits as $\sigma_h S_h$ is decreased as seen in Eq. (7.2). A conduction band with lower conductivity, will have a lower $\sigma_e S_e$, which will be closer in value to $\sigma_h S_h$, which is typically low anyway. This leads to the non-intuitive observation that it is not only materials with a light mass and long MFP minority band that are benefitted by nanostructuring, but materials with highly asymmetric heavy-conduction and light-valence bands can experience even higher relative *PF* improvements when bipolar conduction is degraded. The larger benefit from this asymmetry holds for the electronic thermal conductivity components (compare red versus black lines in Fig. 7.5b), but even more importantly for the *PF* (compare red versus black lines in Fig. 7.5c). This also leads to the encouraging result that bipolar materials with rather lower power factors to begin with due to lower majority band conductivity, could have decent chances in recovering from bipolar effect degradation, provided the minority carriers have longer mean-free-paths.

An interesting point we wish to elucidate here a bit further, is the reason that the lighter valence band masses produce the largest reductions in κ_{bi} and $\kappa_{el,tot}$ as well as the largest increases in *PF* in the presence of NIs. This can be intuitively understood from simple scattering considerations, where the total MFP for minority carriers in the valence band with NIs can be obtained using Matthiessen's rule:

$$\frac{1}{\lambda_{tot}} = \frac{1}{\lambda_{ph}} + \frac{1}{\lambda_{NI}} \tag{7.6}$$

where λ_{tot} is the MFP of the system, λ_{ph} is the MFP due to phonon scattering only, λ_{NI} is the effective distance between NIs that the carriers travel before they scatter, and we have assumed that the electron velocity is the same between all cases. To extract

an analytical estimate of the MFP due to NIs alone, we determine the number of collision (scattering) events, N_{coll}, per unit length (along the transport direction). The inverse of the number of interface scattering events per unit length provides an effective scattering distance λ_{NI} between the pores ($\lambda_{NI} = 1/N_{coll}$) [133]. Using $\lambda_{NI} = 2d/3\varphi$, as defined in Ref. [133] where φ is NI density (~12 % in our system), we find λ_{NI} = 16 nm, which is similar to the spacing of our NIs in the simulator as expected. This MFP is comparable to the phonon scattering MFP in the nominal, heavier band case we consider with $m_v = m_0$ (~ 15 nm) that we have calibrated to in our simulator. In the light band case, however, with $m_v = 0.5m_0$, λ_{ph} is doubled since the carrier velocities are higher ($\nu \propto m^{-1/2}$) and the phonon scattering times are longer ($\tau \propto m^{-D/2}$ where D is dimensionality, in our case D=1 as our structures are narrow enough to be composed of individual 1D subbands) [85]. Thus, $\lambda_{light\_mass} \propto \nu\tau \propto m^{-1/2}\, m^{-D/2} = m^{-1} \propto 2\lambda_{heavy\_mass}$. Therefore, from Eq. (7.6), the NIs are more influential in the light band case in achieving larger relative reduction in minority carrier transport, i.e., λ_{tot} = 7.7 nm in the heavier band case (halved), while it falls by two thirds from λ_{ph} = 30 nm to λ_{tot} = 10 nm in the lighter band case. Thus, in order to achieve maximum benefits, NIs should be placed on the order of the MFP of the material's minority carriers, or even more densely.

Such expectations are evident in our NEGF simulations in the transmission functions, and further details are captured as well. The transmission of the valence bands with masses: $m_v = m_0$ (green lines) and $m_v = 0.5m_0$ (black lines) for the cases without (solid lines) and with (dashed-dotted lines) NIs shown in Fig. 7.7. Again, the energy values are relative to the valence band edge (although plotted on the positive x-axis) and increase in value moving into the band. It can be seen that at lower electron energies the lighter mass (black lines) is more affected by the introduction of NIs leading to a greater reduction in the hole conductance – in fact it seems that the NIs dominate the transmission of both heavy and light bands, somewhat more than expected. For example, at lower energies we see a deviation from Matthiessen's rule with the transmission in the presence of NIs being the same for short and longer electron MFPs. This is possibly due to coherent/wave effects at such nanoscale features that are captured within the use of NEGF, and/or because NEGF captures the geometry of the channel more accurately than simple analytical models. Note that the doubling of λ_{ph} in the light band case is also captured by our NEGF simulations.

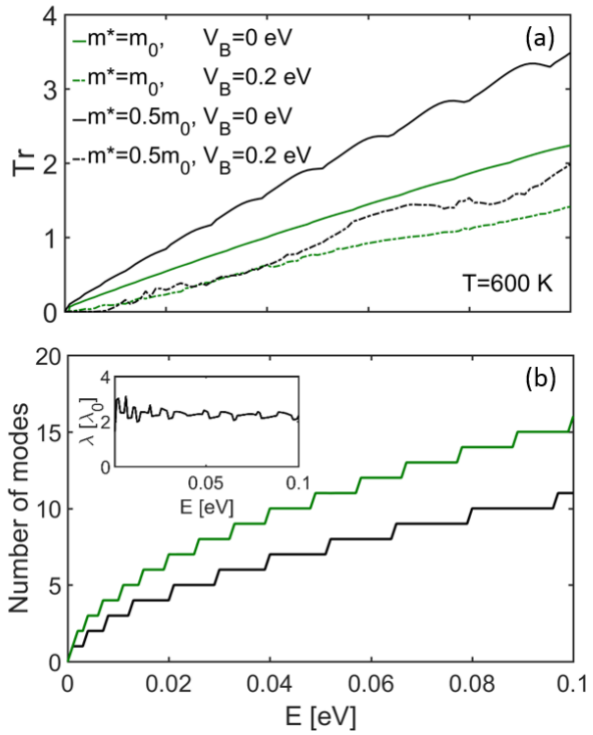

Fig. 7.7: (a) The transmission versus energy of the two valence bands shown in Fig. 2(a): $m_v = m_0$ (green lines); and $m_v = 0.5m_0$ (black lines). Results are shown for structures with (dashed-dotted lines) and without (solid lines) nanoinclusions. Note that the energy values are relative to the valence band edge and increase in value moving into the band. (b) The number of modes versus energy of those two valence bands. Inset: the mean-free-path of the light band as a proportion of the heavy band mean-free-path versus energy.

This can be observed by plotting the number of modes versus energy for the two valences bands of masses $m_v = m_0$ (green line) and $m_v = 0.5m_0$ (black line) in Fig. 7.7b. Using the relation $T(E) = M(E)\langle\lambda(E)\rangle / L$ it can be seen that the ratio of the MFPs of the two systems is equal to their individual $T(E)/M(E)$ ratio [134]. This is just the ratio of the dashed-dotted lines in Fig. 7.7a to the ones in Fig. 7.7b, which is shown in the inset of Fig. 7.7b, indicating that the light mass material has indeed double the MFP (i.e. ~ 30 nm). Combining our results from Figs. 7.6 and 7.7 we can see that the NIs appear to dominate the transmission for both masses and at all temperatures, resulting in very similar transmissions in all cases.

We now consider the effect that introducing NIs has on the overall figure of merit *ZT*. For this, we combine the electronic transport results given above with lattice thermal conductivity results taken from the literature. Reductions in κ_l can vary

considerably depending on a wide variety of factors, including the material type, NI material, temperature, and the density of NIs. As it is very difficult to perform a comparison upon all these parameters, here we extract an average value across all parameters using experimental results found in the literature as shown in Fig. 7.8. That average is an overall 58 % reduction in κ_l, across materials, temperatures, and densities, and we use this to provide an indication of *ZT* improvements. Due to the 2D nature of our simulations, we calculate electrical conductance and electronic thermal conductance which are dimensionally incompatible with the lattice thermal conductivity taken from the literature. An initial *ZT* value is therefore calculated by utilizing experimental results for σ, S, κ_e, and κ_l from the literature (specifically, since our bandgap is most similar to Bi_2Te_3 we take a representative set of values taken from Ref. [40] at 500 K) and then we consider the relative change that our simulations will impose on literature data of pristine structures. Therefore, the improved *ZT* is then computed as:

$$ZT = \frac{\left(\frac{G_{NI}}{G_{pristine}}\right)\sigma_{lit}\left(\frac{S_{NI}}{S_{pristine}}\right)^2 S_{lit}^2}{\left(\frac{K_{e-NI}}{K_{e-pristine}}\right)\kappa_{e-lit} + \left(\frac{\kappa_{l-NI}}{\kappa_{l-pristine}}\right)\kappa_{l-lit}} \tag{7.7}$$

where σ_{lit} etc. are taken from Ref. [40], and the ratios $\frac{G_{NI}}{G_{pristine}}$ etc. are taken from this work in the case of G, S and K_e, and from Fig. 7.8 for κ_l. For the G, S and K_e ratios we take the results of our simulations for the bandstructure $m_c = 0.5m_0$, $m_v = 0.5m_0$ (black lines in Fig. 7.5) and for the κ_l ratio we take a constant 0.42 (i.e. a 58% reduction) across all temperatures. Note that the bandstructure of Bi_2Te_3 is highly anisotropic, thus, what we provide is just a rough indication on how *ZT* in the case of Bi_2Te_3 will benefit in the presence of nanoinclusions [135].

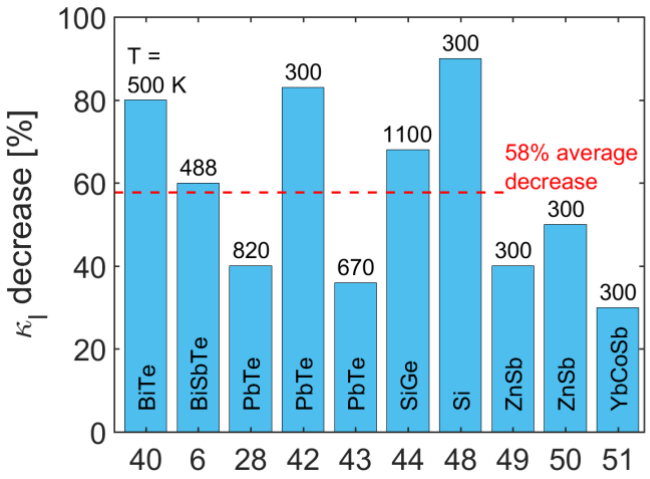

Fig. 7.8: The percentage decrease in lattice thermal conductivity due to the introduction of nanoinclusions in a selection of materials at various temperatures taken from the literature. Reference numbers are given on the x axis, and the bulk material and temperature at which the reduction was recorded are given within the graph.

In Fig. 7.9 we show the percentage increase in ZT due to the introduction of nanoinclusions, for the nominal material we consider with bandstructure $m_c = 0.5m_0$, $m_v = 0.5m_0$ assuming a constant 58% decrease in κ_l (black line). At 300 K the majority of the ZT increase comes from the reduction in κ_l, however as T increases the improvement increases to almost double due to the NIs impact on the bipolar effect and the electronic properties of the material. With the red star we denote the improvement in ZT calculated using the 80% reduction in κ_l at 500 K reported in Ref. [40]. Since we take our initial values from here this represents the closest possible estimation to a potential improvement in ZT in a real material (namely Bi_2Te_3). This gives us a highly significant 148% increase in ZT. It is expected that this could become even higher as the temperature increases beyond our simulated temperatures due to the NIs increasing impact on the PF and κ_e. In addition, a recent work suggests that wavevector-dependent scattering processes, such as boundary scattering (on crystalline boundaries in that case) could also have an increasing impact on κ_l as temperature increases [136].

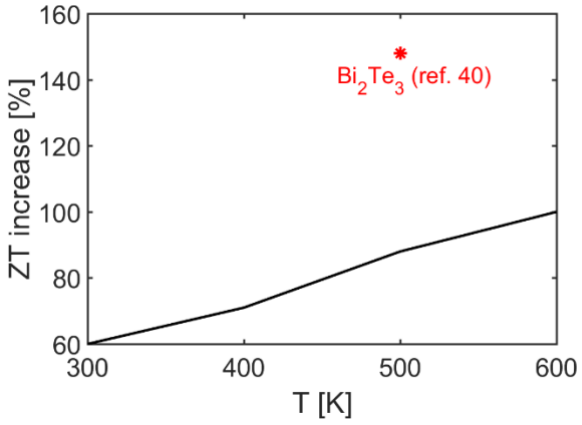

Fig. 7.9: The percentage increase in ZT due to the introduction of NIs versus temperature assuming a constant 58% reduction in κ_l (black line) and in addition for the Bi_2Te_3 taking the more representative values at 500 K from Ref. [40] (red star).

Finally, we note that in this study there are a number of approximations we have made that we would like to elaborate on. Real material bandstructures include a wide variety of effective masses, band gaps, degeneracies, non-parabolicity and multiple valence and/or conduction bands, band changes upon spin-orbit coupling consideration, etc., and these features can also be temperature dependent. In this study however, we only aim to show to first-order the generic potential for NIs to reduce the bipolar effect in narrow bandgap semiconductors, and we assumed a bandgap value comparable to Bi_2Te_3 to relate to common TE materials. Examining further bandstructure details would require a tremendous amount of simulations and is out of the scope of this work. However, to investigate the resilience of our results to changes in the NI barrier height, in Fig. 7.10 we show (a) the percentage decrease in κ_{bi}, (b) the percentage decrease in $\kappa_{el,tot}$, and (c) the percentage increase in PF for a bandstructure with masses $m_c = m_0$, $m_v = m_0$, and bandgap of $E_g = 0.2$ eV, with NIs of barrier height $V_B = 0.2$ eV (green-cross lines – same as green-cross lines in Fig. 7.5), and a bandstructure with the same parameters except NIs barrier heights of $V_B = 1$ eV (green-dashed lines). It can be seen that this causes some additional decrease in $\kappa_{el,tot}$, and increase in PF. However, despite the five-time increase in NI barrier height, these additional benefits are only modest. This suggests that any NI material that causes a barrier height of at least $V_B = 0.2$ eV and above, is already enough to limit the hole flow, and that variations in this variable will not have a significant impact on our results.

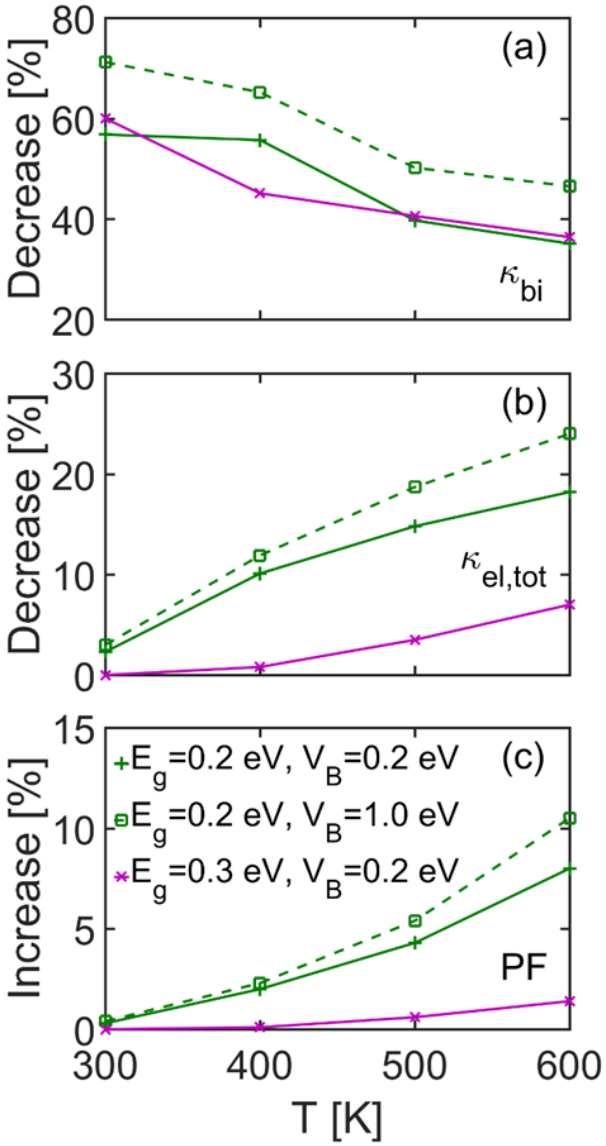

Fig. 7.10: (a) The percentage decrease in the bipolar thermal conductivity κ_{bi} due to the introduction of nanoinclusions on the valence band versus temperature for three bandstructures: $m_c = m_0$, $m_v = m_0$ (green-cross lines) with E_g = 0.2 eV and nanoinclusions of height V_B = 0.2 eV (the same lines as shown in Fig. 5), a bandstructure with masses the same as the green-cross line ($m_c = m_0$, $m_v = m_0$), but with an increased bandgap of E_g = 0.3 eV (purple-cross lines), and a bandstructure with masses the same as the green-cross line ($m_c = m_0$, $m_v = m_0$), but nanoinclusions of height V_B = 1 eV (green-dashed lines). (b) The percentage decrease in the total electronic thermal conductivity $\kappa_{el,tot}$ versus temperature. (c) The percentage increase in power factor $PF = GS^2$ versus temperature.

In order to also observe the influence of a larger bandgap, we also consider an additional bandstructure with masses the same as the green-cross line ($m_c = m_0$, $m_v = m_0$) and NIs of height $V_B = 0.2$ eV, but with an increased bandgap of $E_g = 0.3$ eV (purple cross lines in Fig. 10). This bandgap value is similar to that of PbTe – another important thermoelectric material, for example. It can be seen by comparing the green-cross lines ($E_g = 0.2$ eV) and the purple-cross lines ($E_g = 0.3$ eV) that the NIs have lesser impact at larger bandgaps, although it should be noted that the bipolar effect only becomes significant at higher temperatures in the case of larger bandgap materials. Thus, the same qualitative features and performance improvements will be expected, but at higher temperatures.

Finally, we also note that we have assumed perfect band alignment between the matrix material and the NIs in the conduction band as a best case scenario. In reality, there will always be some scattering added for the conduction band as well when NIs are introduced into the matrix material and this could limit thermoelectric performance benefits at high NI densities, by limiting the overall G.

7.4 Conclusions

In conclusion, in this chapter, using non-equilibrium Green's function simulations for electronic transport, we have demonstrated the ability of nanoinclusions, an important component in the design of advanced thermoelectric materials, to reduce the bipolar effect in narrow bandgap materials. By placing nanoinclusions separated on the order of the mean-free-path of the minority carrier, or even more densely, we showed and quantified how this leads to reductions in the electronic thermal conductivity, but also increases in thermoelectric power factor. These benefits are most pronounced in materials in which the mean-free-path of the minority carriers is large to begin with, either due to low effective masses or low scattering rates. Importantly, however, we showed that in the case of materials with light minority carrier mass (and long mean-free-path) in combination with heavy majority masses, the benefits are even higher, especially for the power factor. In the latter case in particular, the benefits in the power factor are much larger compared to when both majority and minority bands are light. Benefits from nanoinclusions on the power factor also seem more and more significant as temperature increases while benefits on the total electronic thermal conductivity also increase with temperature,

but begin to saturate at some point (although the effect of NIs in reducing the bipolar thermal conductivity is lessened with increasing temperature). Finally, we showed that nanoinclusion barriers of a few hundred meV are enough to provide sufficient benefits, whereas higher barriers do not obscure minority carrier transport to a significantly greater degree.

VIII. Electron transport Monte Carlo simulations

8.1 Introduction

The Monte Carlo (MC) method refers to a wide range of sampling techniques with applications as diverse as computational biology, astrophysics, and finance. The underlying principle is to use repeated random sampling to obtain numerical approximations to problems. These approximations can, by the law of large numbers, be made as accurate as required. In this section we outline the theory behind electron transport Monte Carlo simulations.

8.2 Theory

Electron transport MC simulations are semi-classical in nature in that the electron scattering rates are computed using the quantum mechanical Fermi's Golden Rule, but the motion in between scattering events is classical particle-like motion. The MC simulator we discuss here is a 2D single-electron method as opposed to the more commonly employed ensemble MC method. The advantage of the single-electron method is in its bookkeeping: tracking the movement of only one electron at a time reduces memory requirements.

The simulation begins with the injection of an electron from the contact. Initial energies are random and taken according to the density of states weighted by the Fermi distribution:

$$f(E) = \frac{1}{e^{(E-E_F)/k_B T} + 1} \tag{8.1}$$

Although we simulate a 2D system we use a 3D density of states:

$$g(E) = \frac{m^*}{\pi^2 \hbar^3} \sqrt{2m^*(E - E_C)} \tag{8.2}$$

The electron then travels through the material undergoing 'free-flight' until a scattering event occurs. The electron's energy is updated at each discretization in space in order to check for any interactions with the channel potential (such as a potential barrier (see Fig. 8.1)). If an electron does not have enough energy to continue its path then it is replaced at its previous discretization point and continues on a new path

according to either specular or diffusive reflections. In this work we use specular reflections only. Quantum tunnelling is not considered, however it is possible to include this effect by incorporating information from quantum formalisms such as NEGF.

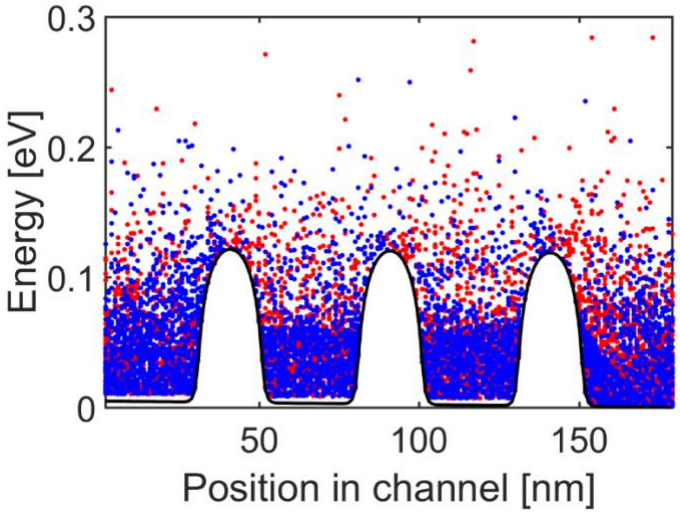

Fig. 8.1: A snapshot of electrons travelling in a channel with three potential barriers taken from a 1D ensemble MC simulation. Red dots represent right-moving electrons and blue dots left-moving electrons.

At the end of the free-flight the electron then undergoes a scattering event. Electrons can be scattered by numerous sources. In this chapter we consider acoustic phonon scattering and ionized impurity scattering, for which the rates are given by:

$$\frac{1}{\tau_{\text{acou}}} = \frac{\pi D_{\text{A}}^2 k_{\text{B}} T}{\hbar c_l} g(E) \tag{8.3}$$

$$\frac{1}{\tau_{\text{IIS}}} = \frac{N_{\text{I}} q^4}{16\sqrt{2m^*}\pi\varepsilon_0^2\varepsilon_r^2}\left[\ln(1+\gamma^2) - \frac{\gamma^2}{1+\gamma^2}\right] E^{-3/2} \tag{8.4}$$

The IIS rate above is taken from a theory due to Brooks and Herring [85] which assumes a screened Coulomb potential. Alternate expressions also exist for the unscreened case:

$$\frac{1}{\tau_{\text{IIS}}} = \frac{N_{\text{I}} q^4}{16\sqrt{2m^*}\pi\varepsilon_0^2\varepsilon_r^2}\left[\ln(1+\gamma_{\text{CW}}^2)\right] E^{-3/2} \tag{8.5}$$

after a theory due to Conwell and Weisskopf, and the strongly screened case [85]:

$$\frac{1}{\tau_{\text{IIS}}} = \frac{\pi N_{\text{I}}}{\hbar}\left(\frac{q^2 L_D^2}{\varepsilon_0 \varepsilon_r}\right)^2 g(E) \tag{8.6}$$

According to Matthiesen's rule, the total scattering time is then given by:

$$\frac{1}{\tau_{\text{tot}}} = \frac{1}{\tau_{\text{acou}}} + \frac{1}{\tau_{\text{IIS}}} \tag{8.7}$$

This quantity is energy dependent as shown in Fig. 8.2.

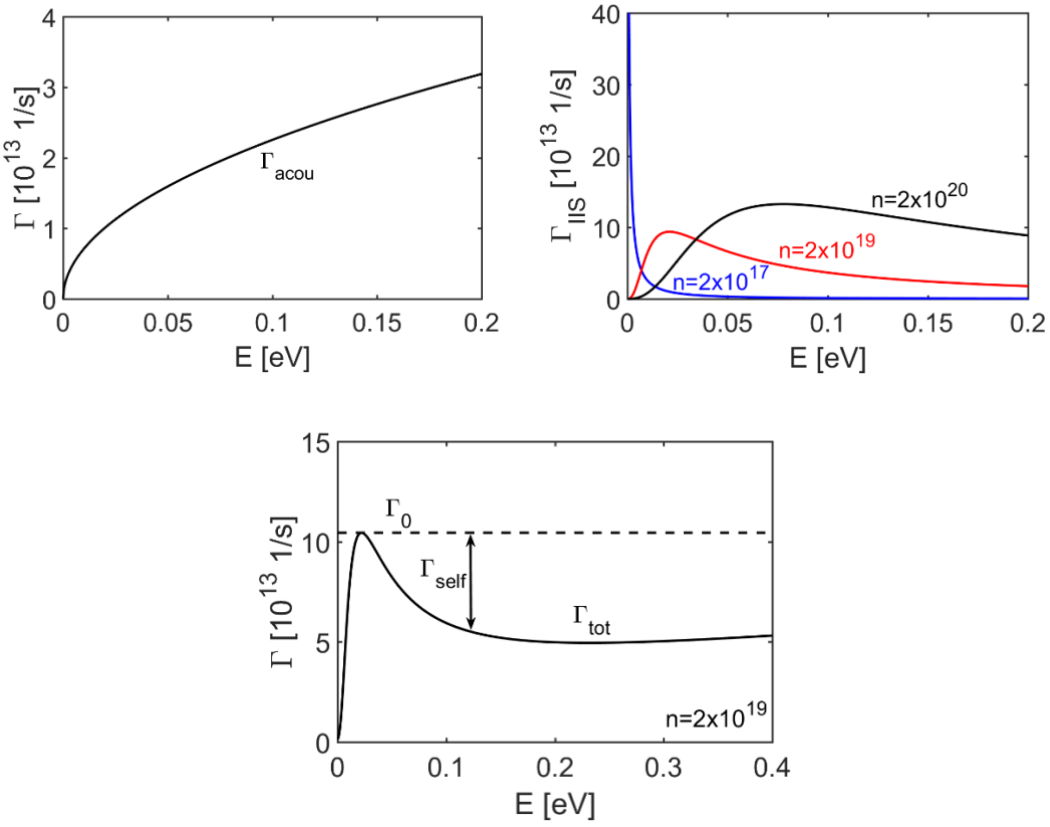

Fig. 8.2: (a) The scattering rates versus energy of acoustic phonon scattering. (b) The scattering rate versus energy of ionized impurity scattering at three different dopant densities: $n = 2\times10^{17}$ cm^{-3} (blue line), $n = 2\times10^{19}$ cm^{-3} (red line), $n = 2\times10^{20}$ cm^{-3} (black line). (c) The total scattering rate Γ_{tot} versus energy. With the black-dashed line we also show the constant scattering rate Γ_0 and with the arrow the self-scattering rate Γ_{self}.

For computational efficiency, a constant scattering rate Γ_0 is used for calculating the electrons time of free flight (see Fig. 8.2c). This is taken to be equal to

the maximum scattering rate across the energies considered[3]. This approximation simplifies the drawing of the electrons random time of free flight down to a simple expression:

$$t = -\frac{1}{\Gamma_0}\ln(r) \tag{8.8}$$

After travelling for time t the electron energy is updated and the 'correct' (energy-dependent) scattering rate is calculated using the updated energy. Since by definition this rate will be less than Γ_0, the difference between them is accounted for by a fictitious scattering rate, Γ_{self}. The probability of each scattering event is then simply its proportion of Γ_0. The type of scattering event undergone is therefore decided by the drawing of another random number. If the chosen scattering event is the fictitious self-scattering then no change is made to the electrons momentum and it continues its free-flight. Else, the electron's state is updated to reflect the relevant scattering event. After undergoing scattering the electron is given a new random trajectory, and in the case of optical phonon scattering, the energy is also updated. Acoustic phonon scattering is assumed to be elastic.

If an electron successfully reaches the opposite contact from which it entered then its total time of flight is recorded. An electron flux can then be defined as:

$$\frac{q_{ij}}{< t_{ij} >} \tag{8.9}$$

where q_{ij} is the number of electrons that make it from side i to side j, and $<t_{ij}>$ is the average time taken.

The contribution of each simulated electron must then be scaled to account for the true number of electrons in the system. The charge on each so-called 'superelectron' is therefore defined by:

$$Q_{super} = \frac{N_{device}}{N_{sim}} \tag{8.10}$$

where N_{sim} is the number of simulated electrons and N_{device} is the number of charges in the device which can be simply calculated from the density of states and Fermi distribution as:

[3] Note that this approximation can cause computational problems in cases where the scattering rate shows divergent behaviour, such as the low doping density IIS rate (blue line in Fig. 8.2b) or the van Hove singularity in the 1D density of states. In such a case, since Γ_0 is equal to the maximum value of Γ_{tot}, Γ_0 can be excessively large and is dominated by Γ_{self} for the majority of energies.

$$N_{\text{device}} = V \int_{E_C}^{\infty} g(E) f(E) dE \tag{8.11}$$

where V is the volume of the system being simulated. Since our system is 2D we assume a small thickness (10 nm).

Note that due to the small systems we are interested in and the relatively large number of electrons we can simulate due to our use of the single-electron method our values for Q_{super} are actually often less than 1. In particular, the systems we investigate below have values of $N_{\text{device}} \sim 10_4$, while we run these simulations with $N_{\text{sim}} = 10_7$, giving a typical value of $Q_{\text{super}} \sim 10_{-3}$.

Consequently the current through the system can then be defined as:

$$I = Q_{\text{super}} \left(\frac{q_{12}}{\tau_{12}} - \frac{q_{21}}{\tau_{21}} \right) \tag{8.12}$$

8.3 Results

8.3.1 Validation

We begin with a validation of some of the properties of the MC simulator that has been constructed.

The backscattering coefficient, R, which is defined as the proportion of electrons which return to the contact from which they were injected can be related to the mean-free-path and length of the channel by [90]:

$$R = \frac{L}{\lambda_0 + L} \tag{8.13}$$

where L is the length of the channel and λ_0 is the mean-free-path (mfp). By a simple rearrangement, this means we can calculate the mean-free-path in terms of L and R:

$$\frac{1}{R} = \frac{\lambda_0}{L} + 1 \tag{8.14}$$

i.e. λ_0 is the gradient when plotting $1/R$ versus $1/L$.

In Fig. 8.3 we show results for $1/R$ versus $1/L$ for acoustic phonon limited backscattering for two different deformation potentials: (a) D_A = 5 eV and (b) D_A = 10 eV. The channel width was W = 100 nm and each point (blue circles) is a simulation of 10 million electrons. With the black-dashed line we show a linear fit. From Fig. 8.3a we can see that an acoustic deformation potential of D_A = 5 eV results in a mean-free-path of 47 nm, and that the results lie along the linear fit with little noise. From Fig. 8.3b it can be seen that after doubling the deformation potential the mfp falls by

a factor of 4 to 12 nm as expected since $\Gamma_{acou} \propto D_A^2$. Yet again the results lie along the linear fit with little noise.

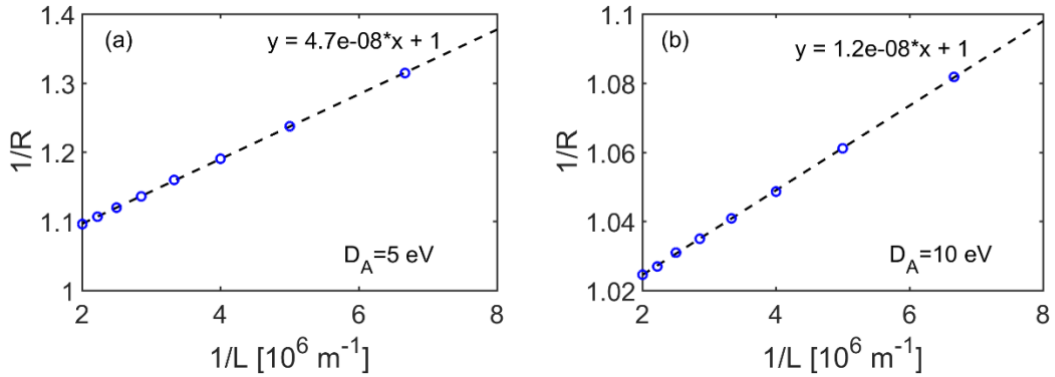

Fig. 8.3: MC simulation results for 1/*R* versus 1/*L* (blue-circles) for (a) acoustic deformation potential D_A = 5 eV, (b) acoustic deformation potential D_A = 10 eV. With the black-dashed lines we show a linear fit.

Next, in Fig. 8.4, we present results for mobility versus carrier concentration results for a pristine channel of length *L* = 150 nm and width *W* = 100 nm for two different scattering regimes: acoustic phonon scattering with D_A = 10 eV (black-dotted line), and acoustic phonon scattering plus ionized impurity scattering (black-solid line). Since we simulate a 2D system we need to scale our results to the bulk experimental values reported in Ref. [137]. We scale our results such that, in the acoustic phonon scattering case, they converge at low carrier concentration to a value of 450 cm^2/Vs. This limiting value also applies to the case of acoustic phonon scattering plus ionized impurity scattering, but is reached at much lower carrier concentration values than we simulate. Good qualitative agreement is found between our results and the expected dependencies (seen for example in Ref. [33]).

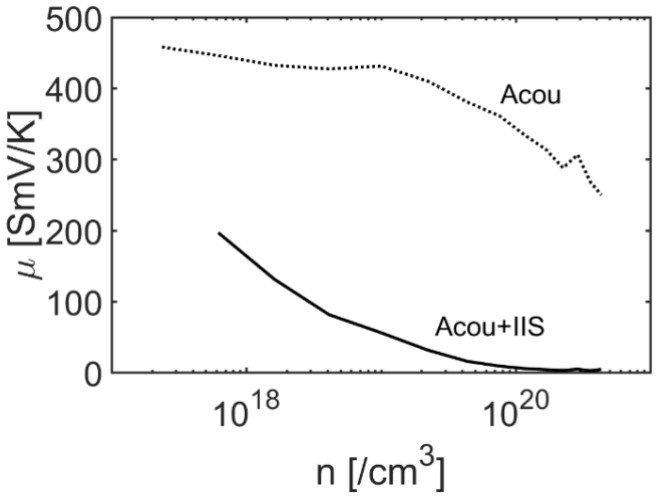

Fig.8.4: Electron mobility versus carrier concentration for two scattering regimes: acoustic phonon scattering (black-dotted line) and acoustic phonon scattering plus ionized impurity scattering (black-solid line).

8.3.2 "Clean filtering"

In chapter 1 we discussed the benefits to the power factor that can arise from energy filtering and modulation doping. In this section we suggest a new concept, "clean filtering", arising from these two techniques.

We begin by noting that modulation doping (doping some regions of a material and leaving others undoped) naturally gives rise to potential barriers. In Fig. 8.5 we show results from self-consistent Poisson calculations of the potential barriers caused by leaving varying lengths of a 1D channel undoped while doping the remainder with a constant $N_D = 10_{19}$ cm$_{-3}$. With the dashed lines we show the doped (lower value) and undoped (higher value) regions and with the solid lines we show the resultant potential within the channel for undoped regions of 10 nm (red lines), 20 nm (blue lines) and 30 nm (black lines). It can clearly be seen that increasing the length of the undoped region not only increases the width of the resulting potential barrier, but also increases its height. In this way, potential barriers of the desired height can be arbitrarily produced by calculating the appropriate undoped length.

Barrier profiles such as those in Fig. 8.5 are commonly achieved via superlattice structures obtained by varying the material used in each region, either by alloying or by alternating materials [138]. However, by achieving these barriers purely through modulation doping, it is predicted that the benefit from the energy filtering effect on the Seebeck can be gained while simultaneously maintaining (or even

enhancing) the conductivity. This is because although the barrier will reduce the number of electrons that contribute to the current, the electrons that still contribute will do so with a much higher mobility in the undoped region (compare black-dashed lines and black-solid lines in Fig. 8.5).

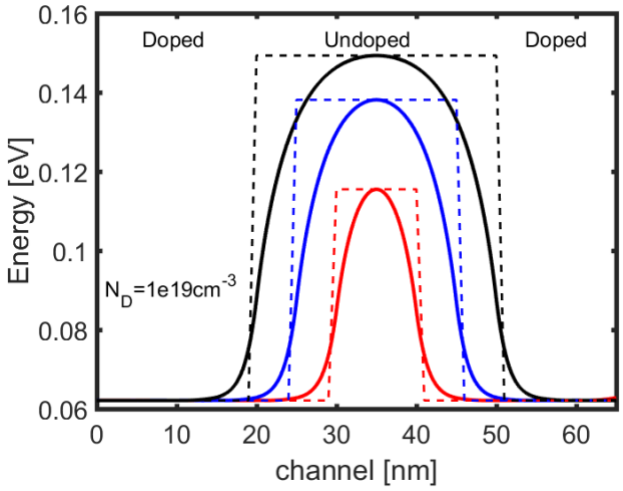

Fig. 8.5: The potential in a channel resulting from a undoped region within regions of constant doping $N_D=10^{19}$ cm^{-3}. With the dashed lines we show the doped (lower value) and undoped (higher value) regions and with the solid lines we show the resultant potential within the channel for undoped regions of 10 nm (red lines), 20 nm (blue lines) and 30 nm (black lines).

To demonstrate this concept we simulate three related systems as shown in Fig. 8.6. First, as a baseline we simulate a pristine channel with a flat potential to represent a system without any nanostructuring present. The channel is of L = 180 nm and width W = 100 nm, and we include acoustic phonon scattering with deformation potential D_A = 10 eV, as well as ionized impurity scattering with a dopant density of N_D = 4×10^{19} cm^{-3}. We place the Fermi level into the band at E_F = 0.05 eV. While this will clearly have the highest conductance, such a system will also have high thermal conductivity and low Seebeck coefficient (particularly since we are in degenerate conditions). This gives a value for the conductance of G = 9.36×10^{-6} S. Next, using self-consistent Poisson calculations, we calculate the potential in the channel due to three undoped regions of 20 nm length. This is then added by hand onto the potential in case 1 in order to model the effect of nanostructuring (e.g. by superlattice). The conductance of the resulting system (shown in Fig. 8.6b) is then G = 1.78×10^{-6} S, a reduction of 80%. Finally, we simulate the same potential as in case 2 but include the

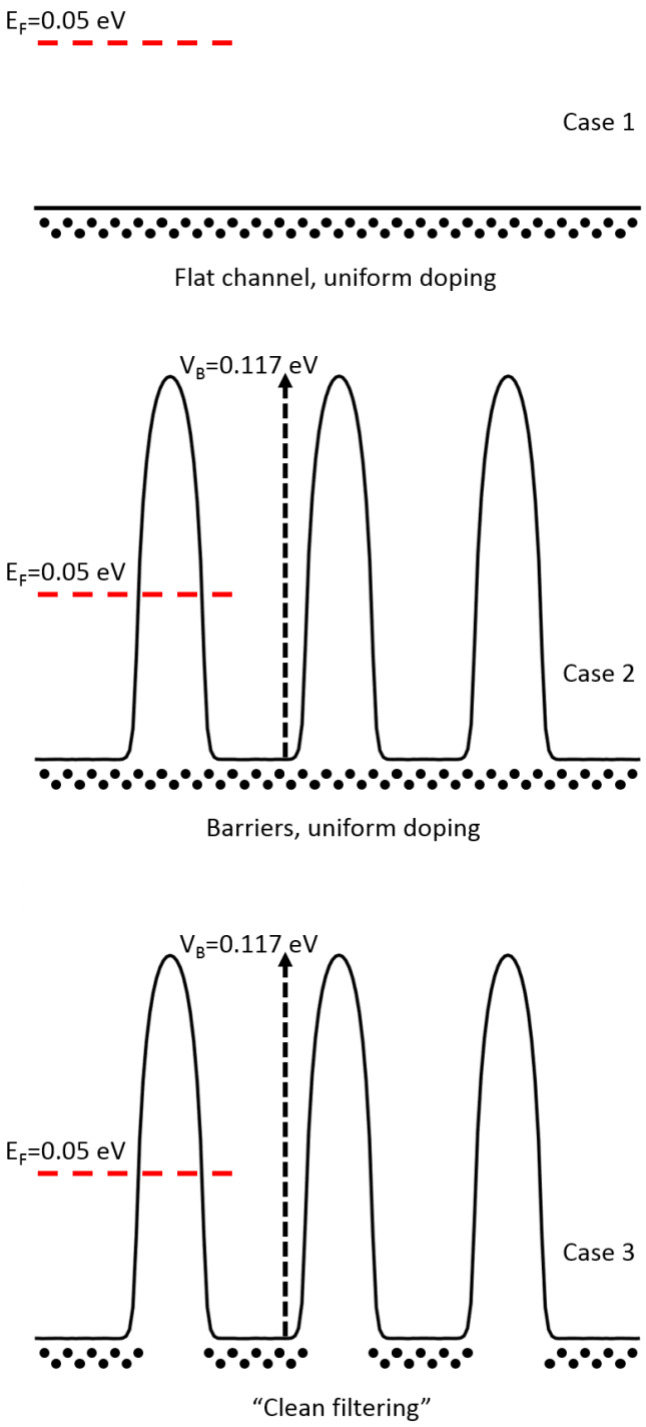

Fig. 8.6: Schematics of (a) a pristine, flat channel with uniform doping (case 1), (b) a series of three potential barriers of height V_B=0.118, with uniform doping throughout the channel (case 2), (c) a series of three potential barriers of height V_B=0.118, with dopants only located in the wells (case 3).

effect of the undoped regions (see Fig. 8.6c). In these regions the mobility of the electrons becomes phonon-limited only. Consequently we see a three-fold increase of the conductance up to $G = 5.92\times10^{-6}$ S compared to case 2. The important effect to note here is that, comparing case 1 to case 3, despite introducing a large barrier over $2k_BT$ above the Fermi level, by "cleaning" the barrier region of dopants we see a reduction in the conductance of just 40%.

Next we calculate an estimate for the improvement in the Seebeck coefficient due to the energy filtering mechanism introduced by the barriers. Since MC simulations require high-field conditions to drive the current it is not numerically practical to simulate temperature differences as seen in previous chapters. Instead we use the Seebeck coefficients dependence on the average energy of the current flow, $S = (\langle E \rangle - E_F)/qT$. In Fig. 8.7 we show the current versus energy for case 1 for 5 repetitions of 10 million electrons and with the black line we show the average of the 5 simulations. It can be seen that at low energies the current becomes negative. This is an artifact of the fact that we simulate high-field transport with a relatively large potential difference of $\Delta V = 0.005$ eV across a channel of just 180 nm in length. Consequently, at low energies, since the 3D density of states goes to zero at the band edge, injection of electrons from the left contact goes to zero, while the right contact remains non-zero. For the calculation of the average energy we therefore remove this artifact and consider only energies above that where the current becomes positive. In case 1 this gives us an average energy of $\langle E \rangle = 0.104$ eV, i.e. $\sim 2k_BT$ above the Fermi level as would approximately be expected, and a Seebeck coefficient of $S = 1.80\times10^{-4}$ V/K. In case 2 with the introduction of the barrier the average energy rises as expected to $\langle E \rangle = 0.151$ eV and consequently the Seebeck coefficient to $S = 3.37\times10^{-4}$ V/K. In case 3 with the introduction of the "clean" barriers the average energy increases again, although only slightly, to $\langle E \rangle = 0.153$ eV, giving $S = 3.44\times10^{-4}$ V/K. Again, it is particularly of use to compare case 1 to case 3. While the conductance fell by 40% with the introduction of the barriers this has been accompanied by an increase of the Seebeck coefficient of 90%, therefore resulting in a more than doubling of the power factor.

It should be noted that in a field where improvements are typically marginal an increase of this magnitude denotes a very significant result. It should also be noted that the increase of over two times in the power factor is for an arbitrarily chosen

system that hasn't undergone any optimization. It seems reasonable to suggest that even higher improvements can be found after careful optimization of parameters such as the barrier height, barrier width, barrier shape, the number of barriers, and in particular the position of the Fermi level. In addition, we have not included the effect of this strategy on the thermal conductivity and consequently *ZT*. Since typically $\kappa_e \propto \sigma$ (Wiedemann-Franz law), the reduction in *G* could well be compensated for by a similar decrease in κ_e. It also seems reasonable to suggest that the systems we present, with dopant free regions distributed within dopant rich regions, should also provide reductions in the lattice thermal conductivity. The enhancement in *ZT* in an optimized system could therefore be well over the factor of 2 we estimate here.

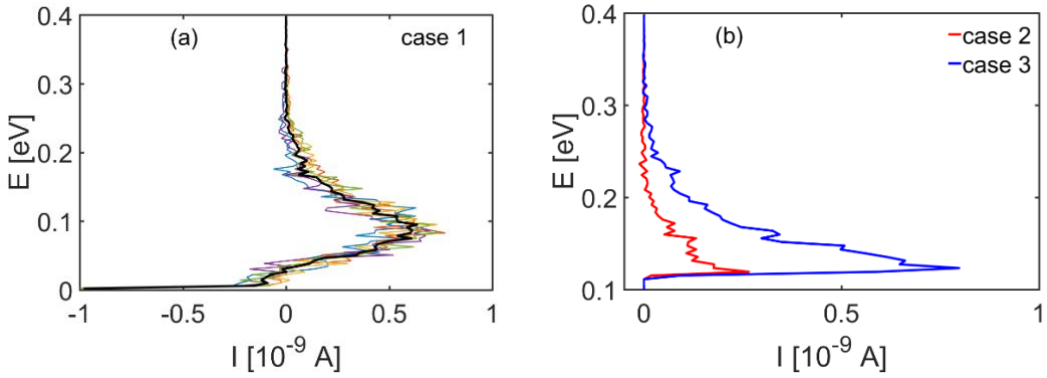

Fig. 8.7: (a) Current versus energy for a pristine channel under acoustic phonon and ionized impurity scattering conditions with $N_D = 4\times10^{19}$ cm^{-3} (case 1). We show the results for 5 simulations of 10 million electrons each, and with the black line we show the average. (b) Current versus energy for case 2 (red line) and case 3 (blue line). Results are the average of 10 simulations of 10 million electrons each.

8.4 Conclusions

In this chapter we presented the theory of the electron Monte Carlo method alongside details of the construction of a 2D electron Monte Carlo simulator. We presented results to validate our simulator against expected dependencies before outlining a new concept we term "clean filtering". Our results show that this approach effectively utilizes the energy filtering mechanism without the significant reductions in the conductance that normally follow. By introducing a barrier ~2.5k_BT above the Fermi level through the removal of dopants from regions in the channel we achieved

an increase in the Seebeck coefficient of 90% while seeing just a 40% reduction in the conductance. This resulted in a doubling of the power factor that could be improved still further by the optimization of the barrier and doping concentration.

IX. Conclusions and future work

9.1 Conclusions

In this thesis we presented a thorough investigation into the impact of nanostructures on the thermoelectric properties of materials using three different levels of computational complexity – from classical Boltzmann theory, to the semi-classical Monte Carlo, down to the fully quantum mechanical non-equilibrium Green's function.

The main results of the work are as follows:

1) The addition of nanoinclusions to a matrix material does not utilize energy filtering effectively, and cannot provide higher power factors compared to an optimized structure without nanoinclusions. The introduction of nanoinclusions reduces the conductance, but does not provide the corresponding increase in the Seebeck coefficient. However, under degenerate conditions, where the Fermi level is placed into the conduction band, moderate increases in the power factor can be achieved of the order of 5-10% if the nanoinclusion barrier heights are of a similar value to the Fermi level.
2) Importantly, the mild power factor improvements are independent of the nanoinclusion density, as long as the nanoinclusions are large enough to prevent quantum tunnelling. This indicates that larger densities of relatively thick nanoinclusions can be utilized to effectively reduce the lattice thermal conductivity without degradation in the power factor. We also showed that variations in the barrier heights, diameter and placement had limited impact on this power factor improvement, providing a design regime for nanocomposites that should give power factor robustness while achieving reductions in the lattice thermal conductivity. The impact of voids was shown to be of a similar nature to nanoinclusions, also demonstrating resilience to variations. In particular we showed that the effect of voids on the power factor is dependent primarily on void density,

and independent of void diameter, unlike the effect on the thermal conductivity.

3) If the carrier concentration of a thermoelectric material is not properly optimized at the temperature of operation, but room temperature optimal doping is instead considered, the power factor can underperform by up to 40% in a bipolar system. Consequently, significant enhancements in the *PF* (~40%) can be achieved through doping optimization. Furthermore we identified that in a bipolar system the optimal carrier concentration indicates an approximately $T^{1.8}$ trend, larger compared to the $T^{3/2}$ trend in unipolar materials, a result of the additional degradation due to bipolar transport.
4) The addition of nanoinclusions can also reduce the bipolar effect in narrow bandgap materials. Nanoinclusions separated on the order of the mean-free-path of the minority carrier, or even more densely, lead to reductions in the electronic thermal conductivity, but also increases in the thermoelectric power factor. Benefits were particularly significant in cases of materials with light minority carrier mass (and long mean-free-path) in combination with heavy majority masses as well as at higher temperatures. These nanoinclusion barriers need only be a few hundred meV in order to provide sufficient benefits.
5) A 2D Monte Carlo simulator was constructed and validated. A new power factor enhancement mechanism which we term "clean filtering" was then introduced. Using Monte Carlo simulations we showed this could provide a doubling of the power factor, even before any optimization of the relevant structure. This represents a highly significant result, potentially establishing a new direction for the development of high power factor thermoelectric materials.

9.2 Future work

There are a few potentially interesting lines of inquiry that could follow from this work:

1) Although chapters 6 and 7 discussed the electron thermal conductivity, this was not considered in chapters 3, 4, and 5. In order to get a more complete

picture of how nanoinclusions and voids impact the overall figure of merit *ZT*, the electron thermal conductivity could be extracted from these simulations. This allows the Lorenz number to be calculated and then combined with simulations for the lattice thermal conductivity (as done to a certain extent in chapter 5) or combined with experimental results from the literature (as in chapter 7) could provide further guidance as to the optimization of such structures for enhanced *ZT*.

2) Throughout this thesis/work, the bandstructures involved were taken to be isotropic and approximated by a constant effective mass throughout the system. However some interesting effects potentially come in to play when either of these assumptions is taken away. First, if anisotropy is considered then it becomes possible for the sign of the Seebeck coefficient to be direction dependent (i.e. at the same carrier concentration one has an n-type material in one transport direction, and a p-type material in another transport direction). This poses the question of how to optimize the power factor in such a bandstructure and what the necessary trade-offs are. Additionally, by having isotropy in one band type (e.g. the conductance band), but anisotropy in the other (e.g. the valence band), it potentially becomes possible to reduce the bipolar effect if the system is polycrystalline. By how much, and whether any sources of optimization exist are open questions. Secondly, if one removes the assumption of the effective mass remaining constant throughout the channel taken in chapter 3, then one can ask the question, is it possible to increase the conductivity (and maybe even, simultaneously, the Seebeck coefficient) by adjusting the mass of the nanoinclusion material to match *k* vectors and therefore limit reflections.

3) In chapter 9 we demonstrate the possibility of 'clean filtering' to provide power factor improvements, however no optimization of the concept was undertaken. To fully understand this phenomenon, it would be worthwhile to conduct a thorough investigation of the parameters involved, including the barrier height, the barrier width, the barrier shape, the Fermi level placement, and the various possible scattering regimes.

References

[1] V. Masson-Delmotte *et al.*, “Special Report on Global warming of 1.5°C,” 2018.

[2] C. Forman, I. K. Muritala, R. Pardemann, and B. Meyer, “Estimating the global waste heat potential,” *Renew. Sustain. Energy Rev.*, vol. 57, pp. 1568–1579, 2016.

[3] R. Freer and A. Powell, “Thermoelectric Roadmap,” 2018.

[4] K. F. Hsu *et al.*, “Cubic AgPb_{m}SbTe_{2+m} : Bulk Thermoelectric Materials with High Figure of Merit,” *Science (80-.).*, vol. 303, no. 5659, pp. 818–821, 2004.

[5] Y. Pei *et al.*, “Stabilizing the optimal carrier concentration for high thermoelectric efficiency,” *Adv. Mater.*, vol. 23, no. 47, pp. 5674–5678, 2011.

[6] K. Biswas *et al.*, “High-performance bulk thermoelectrics with all-scale hierarchical architectures,” *Nature*, vol. 489, no. 7416, pp. 414–418, 2012.

[7] T. Fu *et al.*, “Enhanced thermoelectric performance of PbTe bulk materials with figure of merit zT >2 by multi-functional alloying,” *J. Mater.*, vol. 2, no. 2, pp. 141–149, 2016.

[8] B. Poudel *et al.*, “High-Thermoelectric of Nanostructured Antimony Performance Bismuth Bulk Alloys Telluride,” *Science (80-.).*, vol. 320, no. May, pp. 634–638, 2008.

[9] W. Xie, X. Tang, Y. Yan, Q. Zhang, and T. M. Tritt, “Unique nanostructures and enhanced thermoelectric performance of melt-spun BiSbTe alloys,” *Appl. Phys. Lett.*, vol. 94, no. 10, 2009.

[10] S. Il Kim *et al.*, “Dense dislocation arrays embedded in grain boundaries for high-performance bulk thermoelectrics.,” *Science (80-.).*, vol. 348, no. 6230, pp. 109–114, 2015.

[11] L. D. Zhao *et al.*, “Ultralow thermal conductivity and high thermoelectric figure of merit in SnSe crystals,” *Nature*, vol. 508, no. 7496, pp. 373–377, 2014.

[12] H. Liu *et al.*, “Copper ion liquid-like thermoelectrics,” *Nat. Mater.*, vol. 11, no. 5, pp. 422–425, 2012.

[13] H. Liu *et al.*, “Ultrahigh thermoelectric performance by electron and phonon critical scattering in Cu 2 Se 1-x I x,” *Adv. Mater.*, vol. 25, no. 45, pp. 6607–6612, 2013.

[14] B. Zhong *et al.*, “High superionic conduction arang from aligned large lamellae and large figure of merit in bulk Cu1.94Al0.02Se,” *Appl. Phys. Lett.*, vol. 105, no. 12, pp. 0–4, 2014.

[15] A. A. Olvera *et al.*, “Partial indium solubility induces chemical stability and colossal thermoelectric figure of merit in Cu2Se,” *Energy Environ. Sci.*, vol. 10, no. 7, pp. 1668–1676, 2017.

[16] B. C. Sales, D. Mandrus, and R. K. Williams, “Filled Skutterudite Antimonides : A New Class of Thermoelectric Materials,” *Science (80-.).*, vol. 272, no. 5266, pp. 1325–1328, 1996.

[17] X. Shi *et al.*, “Realization of high thermoelectric performance in n-type partially filled skutterudites,” *J. Mater. Res.*, vol. 26, no. 15, pp. 1745–1754, 2011.

[18] G. Rogl *et al.*, “N-Type skutterudites (R,Ba,Yb)yCo4Sb12 (R = Sr, La, Mm, DD, SrMm, SrDD) approaching ZT ≈ 2.0,” *Acta Mater.*, vol. 63, pp. 30–43, 2014.

[19] G. Joshi, X. Yan, H. Wang, W. Liu, G. Chen, and Z. Ren, “Enhancement in thermoelectric figure-of-merit of an N-type half-Heusler compound by the nanocomposite approach,” *Adv. Energy Mater.*, vol. 1, no. 4, pp. 643–647, 2011.

[20] X. Yan *et al.*, “Thermoelectric property study of nanostructured p-type half-heuslers (Hf, Zr, Ti)CoSb0.8 Sn0.2,” *Adv. Energy Mater.*, vol. 3, no. 9, pp. 1195–1200, 2013.

[21] C. Fu *et al.*, “Realizing high figure of merit in heavy-band p-type half-Heusler thermoelectric materials,” *Nat. Commun.*, vol. 6, pp. 1–7, 2015.

[22] G. Joshi *et al.*, “Enhanced thermoelectric figure-of-merit in nanostructured p-type silicon germanium bulk alloys,” *Nano Lett.*, vol. 8, no. 12, pp. 4670–4674, 2008.

[23] B. Yu *et al.*, “Enhancement of thermoelectric properties by modulation-doping in silicon germanium alloy nanocomposites,” *Nano Lett.*, vol. 12, no. 4, pp. 2077–2082, 2012.

[24] S. Bathula *et al.*, “Enhanced thermoelectric figure-of-merit in spark plasma

sintered nanostructured n-type SiGe alloys," *Appl. Phys. Lett.*, vol. 101, no. 21, 2012.

[25] J. P. Heremans, M. S. Dresselhaus, E. Bell, Lon, and D. T. Morelli, "When thermoelectrics reached the nanoscale," *Nat. Nanotechnol.*, vol. 8, p. 471, 2013.

[26] M. Zebarjadi *et al.*, "Power factor enhancement by modulation doping in bulk nanocomposites," *Nano Lett.*, vol. 11, p. 2225, 2011.

[27] H. Mizuno, S. Mossa, and J. L. Barrat, "Beating the amorphous limit in thermal conductivity by superlattices design," *Sci. Rep.*, vol. 5, pp. 1–13, 2015.

[28] G. Chen *et al.*, "Increased Phonon Scattering by Nanograins and Point Defects in Nanostructured Silicon with a Low Concentration of Germanium," *Phys. Rev. Lett.*, vol. 102, no. 19, pp. 2–5, 2009.

[29] H. Ikeda and F. Salleh, "Influence of heavy doping on Seebeck coefficient in silicon-on-insulator," *Appl. Phys. Lett.*, vol. 96, no. 1, pp. 1–4, 2010.

[30] M. Verdier, K. Termentzidis, and D. Lacroix, "Crystalline-amorphous silicon nano-composites: Nano-pores and nano-inclusions impact on the thermal conductivity," *J. Appl. Phys.*, vol. 119, no. 17, 2016.

[31] R. Yang, G. Chen, and M. S. Dresselhaus, "Thermal conductivity of simple and tubular nanowire composites in the longitudinal direction," *Phys. Rev. B - Condens. Matter Mater. Phys.*, vol. 72, no. 12, pp. 1–7, 2005.

[32] J. H. Lee, J. C. Grossman, J. Reed, and G. Galli, "Lattice thermal conductivity of nanoporous Si: Molecular dynamics study," *Appl. Phys. Lett.*, vol. 91, no. 22, pp. 1–4, 2007.

[33] N. Neophytou, X. Zianni, H. Kosina, S. Frabboni, B. Lorenzi, and D. Narducci, "Simultaneous increase in electrical conductivity and Seebeck coefficient in highly boron-doped nanocrystalline Si," *Nanotechnology*, vol. 24, no. 20, 2013.

[34] N. S. Bennett, D. Byrne, A. Cowley, and N. Neophytou, "Dislocation loops as a mechanism for thermoelectric power factor enhancement in silicon nano-layers," *Appl. Phys. Lett.*, vol. 109, no. 17, 2016.

[35] C. Gayner and K. K. Kar, "Recent advances in thermoelectric materials," *Prog. Mater. Sci.*, vol. 83, pp. 330–382, 2016.

[36] P. E. Hopkins *et al.*, "Reduction in the thermal conductivity of single

crystalline silicon by phononic crystal patterning," *Nano Lett.*, vol. 11, no. 1, pp. 107–112, 2011.

[37] C. J. Vineis, A. Shakouri, A. Majumdar, and M. G. Kanatzidis, "Nanostructured thermoelectrics: Big efficiency gains from small features," *Adv. Mater.*, vol. 22, no. 36, pp. 3970–3980, 2010.

[38] A. Popescu, L. M. Woods, J. Martin, and G. S. Nolas, "Model of transport properties of thermoelectric nanocomposite materials," *Phys. Rev. B - Condens. Matter Mater. Phys.*, vol. 79, no. 20, pp. 1–7, 2009.

[39] B. Qiu, H. Bao, G. Zhang, Y. Wu, and X. Ruan, "Molecular dynamics simulations of lattice thermal conductivity and spectral phonon mean free path of PbTe: Bulk and nanostructures," *Comput. Mater. Sci.*, vol. 53, no. 1, pp. 278–285, 2012.

[40] S. Fan, J. Zhao, Q. Yan, J. Ma, and H. H. Hng, "Influence of nanoinclusions on thermoelectric properties of n-type Bi2Te3nanocomposites," *J. Electron. Mater.*, vol. 40, no. 5, pp. 1018–1023, 2011.

[41] M. K. Keshavarz, D. Vasilevskiy, R. A. Masut, and S. Turenne, "Synthesis and characterization of bismuth telluride-based thermoelectric nanocomposites containing MoS2nano-inclusions," *Mater. Charact.*, vol. 95, pp. 44–49, 2014.

[42] J. P. Heremans, C. M. Thrush, and D. T. Morelli, "Thermopower enhancement in PbTe with Pb precipitates," *J. Appl. Phys.*, vol. 98, no. 6, 2005.

[43] S. Ahmad *et al.*, "Boosting thermoelectric performance of p-type SiGe alloys through in-situ metallic YSi2 nanoinclusions," *Nano Energy*, vol. 27, pp. 282–297, 2016.

[44] T. H. Zou *et al.*, "Simultaneous enhancement in thermoelectric power factor and phonon blocking in hierarchical nanostructured β-Zn4Sb3-Cu3SbSe4," *Appl. Phys. Lett.*, vol. 104, no. 1, pp. 0–5, 2014.

[45] M. Mohebali, Y. Liu, L. Tayebi, J. S. Krasinski, and D. Vashaee, "Thermoelectric figure of merit of bulk FeSi2-Si0.8Ge0.2 nanocomposite and a comparison with β-FeSi2," *Renew. Energy*, vol. 74, pp. 940–947, 2015.

[46] M. Saleemi *et al.*, "Thermoelectric performance of higher manganese silicide nanocomposites," *J. Alloys Compd.*, vol. 619, pp. 31–37, 2015.

[47] G. Tan *et al.*, "High thermoelectric performance of p-type SnTe via a

synergistic band engineering and nanostructuring approach," *J. Am. Chem. Soc.*, vol. 136, no. 19, pp. 7006–7017, 2014.

[48] S. Johnsen *et al.*, "Nanostructures boost the thermoelectric performance of PbS.," *J. Am. Chem. Soc.*, vol. 133, no. 10, pp. 3460–70, 2011.

[49] Y. Y. Li *et al.*, "Enhanced thermoelectric performance of Cu2Se/Bi0.4Sb1.6Te3nanocomposites at elevated temperatures," *Appl. Phys. Lett.*, vol. 108, no. 6, pp. 3–8, 2016.

[50] T. Zou *et al.*, "Enhanced thermoelectric performance of β-Zn4Sb3based nanocomposites through combined effects of density of states resonance and carrier energy filtering," *Sci. Rep.*, vol. 5, no. January 2016, 2015.

[51] J. Peng *et al.*, "A study of Yb0.2Co4Sb12-AgSbTe2 nanocomposites: Simultaneous enhancement of all three thermoelectric properties," *J. Mater. Chem. A*, vol. 2, no. 1, pp. 73–79, 2014.

[52] L. D. Chen, X. Y. Huang, M. Zhou, X. Shi, and W. B. Zhang, "The high temperature thermoelectric performances of Zr0.5Hf 0.5Ni0.8Pd0.2Sn0.99Sb 0.01 alloy with nanophase inclusions," *J. Appl. Phys.*, vol. 99, no. 6, 2006.

[53] L. D. Zhao, V. P. Dravid, and M. G. Kanatzidis, "The panoscopic approach to high performance thermoelectrics," *Energy Environ. Sci.*, vol. 7, no. 1, pp. 251–268, 2014.

[54] N. Neophytou, "Prospects of low-dimensional and nanostructured silicon-based thermoelectric materials: findings from theory and simulation," *Eur. Phys. J. B*, vol. 88, no. 4, pp. 1–35, 2015.

[55] L. D. Hicks and M. S. Dresselhaus, "Thermoelectric figure of merit of a one-dimensional conductor," *Phys. Rev. B*, vol. 47, no. 24, pp. 8–11, 1993.

[56] N. Neophytou and H. Kosina, "Atomistic simulations of low-field mobility in Si nanowires: Influence of confinement and orientation," *Phys. Rev. B - Condens. Matter Mater. Phys.*, vol. 84, no. 8, pp. 1–15, 2011.

[57] N. Neophytou, X. Zianni, H. Kosina, S. Frabboni, B. Lorenzi, and D. Narducci, "Power factor enhancement by inhomogeneous distribution of dopants in two-phase nanocrystalline systems," *J. Electron. Mater.*, vol. 43, no. 6, pp. 1896–1904, 2014.

[58] J. H. Bahk, Z. Bian, and A. Shakouri, "Electron energy filtering by a nonplanar potential to enhance the thermoelectric power factor in bulk materials," *Phys. Rev. B - Condens. Matter Mater. Phys.*, vol. 87, no. 7, 2013.

[59] C. Bera *et al.*, “Thermoelectric properties of nanostructured Si1-xGexand potential for further improvement,” *J. Appl. Phys.*, vol. 108, no. 12, 2010.

[60] A. J. Minnich, M. S. Dresselhaus, Z. F. Ren, and G. Chen, “Bulk nanostructured thermoelectric materials: Current research and future prospects,” *Energy Environ. Sci.*, vol. 2, no. 5, pp. 466–479, 2009.

[61] R. Kim and M. S. Lundstrom, “Computational study of energy filtering effects in one-dimensional composite nano-structures,” *J. Appl. Phys.*, vol. 111, no. 2, 2012.

[62] K. Nielsch, J. Bachmann, J. Kimling, and H. Böttner, “Thermoelectric nanostructures: From physical model systems towards nanograined composites,” *Adv. Energy Mater.*, vol. 1, no. 5, pp. 713–731, 2011.

[63] J. Tang *et al.*, “Holey silicon as an efficient thermoelectric material,” *Nano Lett.*, vol. 10, no. 10, pp. 4279–4283, 2010.

[64] S. Wolf, N. Neophytou, Z. Stanojevic, and H. Kosina, “Monte Carlo Simulations of Thermal Conductivity in Nanoporous Si Membranes,” *J. Electron. Mater.*, vol. 43, no. 10, pp. 3870–3875, 2014.

[65] S. Wolf, N. Neophytou, and H. Kosina, “Thermal conductivity of silicon nanomeshes: Effects of porosity and roughness,” *J. Appl. Phys.*, vol. 115, no. 20, 2014.

[66] J. A. Perez-Taborda, M. Muñoz Rojo, J. Maiz, N. Neophytou, and M. Martín-González, “Ultra-low thermal conductivities in large-area Si-Ge nanomeshes for thermoelectric applications,” *Sci. Rep.*, vol. 6, no. August, pp. 1–10, 2016.

[67] G. Ding, G. Y. Gao, Z. Huang, W. Zhang, and K. Yao, “Thermoelectric properties of monolayer MSe2 (M = Zr, Hf): Low lattice thermal conductivity and a promising figure of merit,” *Nanotechnology*, vol. 27, no. 37, 2016.

[68] H. Huang *et al.*, “Metallic 1T phase MoS2 nanosheets for high-performance thermoelectric energy harvesting,” *Nano Energy*, vol. 26, pp. 172–179, 2016.

[69] W. Huang, X. Luo, C. K. Gan, S. Y. Quek, and G. Liang, “Theoretical study of thermoelectric properties of few-layer MoS2and WSe2,” *Phys. Chem. Chem. Phys.*, vol. 16, no. 22, pp. 10866–10874, 2014.

[70] S. Kumar and U. Schwingenschlögl, “Thermoelectric response of bulk and monolayer MoSe2and WSe2,” *Chem. Mater.*, vol. 27, no. 4, pp. 1278–1284, 2015.

[71] Y. Tang, R. Hanus, S. W. Chen, and G. J. Snyder, “Solubility design leading

to high figure of merit in low-cost Ce-CoSb<inf>3</inf> skutterudites," *Nat. Commun.*, vol. 6, no. May, pp. 1–7, 2015.

[72] Y. Tang *et al.*, "Convergence of multi-valley bands as the electronic origin of high thermoelectric performance in CoSb3 skutterudites," *Nat. Mater.*, vol. 14, no. 12, pp. 1223–1228, 2015.

[73] M. Zebarjadi *et al.*, "Role of phonon dispersion in studying phonon mean free paths in skutterudites," *J. Appl. Phys.*, vol. 112, no. 4, 2012.

[74] M. Beekman and A. Vandergraaff, "High-temperature thermal conductivity of thermoelectric clathrates," *J. Appl. Phys.*, vol. 121, no. 20, 2017.

[75] Y. Yin, B. Tudu, and A. Tiwari, "Recent advances in oxide thermoelectric materials and modules," *Vacuum*, vol. 146, pp. 356–374, 2017.

[76] S. M. Kauzlarich, S. R. Brown, and G. Jeffrey Snyder, "Zintl phases for thermoelectric devices," *J. Chem. Soc. Dalt. Trans.*, no. 21, pp. 2099–2107, 2007.

[77] J. Shuai *et al.*, " Higher thermoelectric performance of Zintl phases (Eu 0.5 Yb 0.5) 1−x Ca x Mg 2 Bi 2 by band engineering and strain fluctuation ," *Proc. Natl. Acad. Sci.*, vol. 113, no. 29, pp. E4125–E4132, 2016.

[78] A. Nozariasbmarz *et al.*, "Thermoelectric silicides: A review," *Jpn. J. Appl. Phys.*, vol. 56, no. 5S1, p. 05DA04, 2017.

[79] R. Stern, B. Dongre, and G. K. H. Madsen, "Extrinsic doping of the half-Heusler compounds," *Nanotechnology*, vol. 27, no. 33, 2016.

[80] X. Yan *et al.*, "Enhanced thermoelectric figure of merit of p-type half-heuslers," *Nano Lett.*, vol. 11, no. 2, pp. 556–560, 2011.

[81] M. Zebarjadi, K. Esfarjani, M. S. Dresselhaus, Z. F. Ren, and G. Chen, "Perspectives on thermoelectrics: From fundamentals to device applications," *Energy Environ. Sci.*, vol. 5, no. 1, pp. 5147–5162, 2012.

[82] A. F. Ioffe, *Semiconductor thermoelements and thermoelectric cooling*. 1957.

[83] M. Thesberg, H. Kosina, and N. Neophytou, "On the Lorenz number of multiband materials," *Phys. Rev. B*, vol. 95, no. 12, 2017.

[84] N. Ashcroft and N. Mermin, "Solid state physics." 1976.

[85] M. Lundstrom, *Fundamentals of Carrier Transport, 2nd edn*, vol. 13, no. 2. 2002.

[86] G. D. Mahan and J. Sofo, "The best thermoelectric," *Appl. Phys. Sci.*, vol. 93, pp. 7436–7439, 1996.

[87] J. Scheidemantel, C. Ambrosch-Draxl, T. Thonhauser, V. Badding, and O. Sofo, “Transport coefficients from first-principles calculations,” *Phys. Rev. B - Condens. Matter Mater. Phys.*, vol. 68, no. 12, pp. 1–6, 2003.

[88] A. Shakouri and M. Zebarjadi, *Thermal Nanosystems and Nanomaterials*, vol. 118. 2009.

[89] M. V. Fischetti, “Long-range Coulomb interactions in small Si devices. Part II. Effective electron mobility in thin-oxide structures,” *J. Appl. Phys.*, vol. 89, no. 2, pp. 1232–1250, 2001.

[90] R. Kim, S. Datta, and M. S. Lundstrom, “Influence of dimensionality on thermoelectric device performance,” *J. Appl. Phys.*, vol. 105, no. 3, 2009.

[91] J. Schwinger, “Brownian motion of a quantum oscillator,” *J. Math. Phys.*, vol. 2, no. 3, pp. 407–432, 1961.

[92] L. V. Keldysh, “Diagram technique for nonequilibrium processes,” *J. Exptl. Theor. Phys.*, vol. 20, no. 4, p. 1018, 1965.

[93] S. Datta, “Nanoscale device modeling: the Green’s function method,” *Superlattices Microstruct.*, vol. 28, no. 4, pp. 253–278, 2000.

[94] S. Datta, *Quantum transport: Atom to transistor*. Cambridge, 2005.

[95] S. Datta, *Electronic transport in mesoscopic systems*. Cambridge University Press, 1995.

[96] M. P. Anantram, M. S. Lundstrom, and D. E. Nikonov, “Modeling of nanoscale devices,” *Proc. IEEE*, vol. 96, no. 9, pp. 1511–1550, 2008.

[97] S. O. Koswatta, S. Hasan, M. S. Lundstrom, M. P. Anantram, and D. E. Nikonov, “Nonequilibrium Green’s function treatment of phonon scattering in carbon-nanotube transistors,” *IEEE Trans. Electron Devices*, vol. 54, no. 9, pp. 2339–2351, 2007.

[98] R. Rhyner and M. Luisier, “Phonon-limited low-field mobility in silicon: Quantum transport vs. linearized Boltzmann Transport Equation,” *J. Appl. Phys.*, vol. 114, no. 22, 2013.

[99] R. Golizadeh-Mojarad, A. N. M. Zainuddin, G. Klimeck, and S. Datta, “Atomistic non-equilibrium Green’s function simulations of Graphene nano-ribbons in the quantum hall regime,” *J. Comput. Electron.*, vol. 7, no. 3, pp. 407–410, 2008.

[100] N. Neophytou and M. Thesberg, “Modulation doping and energy filtering as effective ways to improve the thermoelectric power factor,” *J. Comput.*

Electron., vol. 15, no. 1, pp. 16–26, 2016.

[101] M. Thesberg, M. Pourfath, N. Neophytou, and H. Kosina, "The Fragility of Thermoelectric Power Factor in Cross-Plane Superlattices in the Presence of Nonidealities: A Quantum Transport Simulation Approach," *J. Electron. Mater.*, vol. 45, no. 3, pp. 1584–1588, 2016.

[102] M. Thesberg, M. Pourfath, H. Kosina, and N. Neophytou, "The influence of non-idealities on the thermoelectric power factor of nanostructured superlattices," *J. Appl. Phys.*, vol. 118, no. 22, 2015.

[103] T. B. Boykin and G. Klimeck, "The discretized Schrödinger equation and simple models for semiconductor quantum wells," *Eur. J. Phys.*, vol. 25, no. 4, pp. 503–514, 2004.

[104] M. P. L. Sancho, J. M. L. Sancho, and J. Rubio, "Quick iterative scheme for the calculation of transfer matrices: application to Mo(100)," *J. F Met. Phys.*, vol. 14, p. 1205, 1984.

[105] A. Price, A. Martinez, R. Valin, and J. R. Barker, "Impact of different electron-phonon scattering models on the electron transport in a quantum wire," *J. Phys. Conf. Ser.*, vol. 526, no. 1, 2014.

[106] R. Kim and M. S. Lundstrom, "Computational study of the Seebeck coefficient of one-dimensional composite nano-structures," *J. Appl. Phys.*, vol. 110, no. 3, p. 034511, 2011.

[107] S. V. Faleev and F. Léonard, "Theory of enhancement of thermoelectric properties of materials with nanoinclusions," *Phys. Rev. B - Condens. Matter Mater. Phys.*, vol. 77, no. 21, 2008.

[108] A. Minnich and G. Chen, "Modified effective medium formulation for the thermal conductivity of nanocomposites," *Appl. Phys. Lett.*, vol. 91, no. 7, pp. 1–4, 2007.

[109] M. Liu and X. Y. Qin, "Enhanced thermoelectric performance through energy-filtering effects in nanocomposites dispersed with metallic particles," *Appl. Phys. Lett.*, vol. 101, no. 13, 2012.

[110] J. Zhou and R. Yang, "Quantum and classical thermoelectric transport in quantum dot nanocomposites," *J. Appl. Phys.*, vol. 110, no. 8, 2011.

[111] B. Lorenzi *et al.*, "Paradoxical Enhancement of the Power Factor of Polycrystalline Silicon as a Result of the Formation of Nanovoids," *J. Electron. Mater.*, vol. 43, no. 10, pp. 3812–3816, 2014.

[112] N. Neophytou and H. Kosina, “Optimizing thermoelectric power factor by means of a potential barrier,” *J. Appl. Phys.*, vol. 114, no. 4, 2013.

[113] B. Qiu *et al.*, “First-principles simulation of electron mean-free-path spectra and thermoelectric properties in silicon,” *Epl*, vol. 109, no. 5, 2015.

[114] M. P. Persson, A. Lherbier, Y.-M. Niquet, F. Triozon, and S. Roche, “Orientational Dependence of Charge Transport in Disordered Silicon Nanowires,” *Nano Lett.*, vol. 8, no. 12, pp. 4146–4150, 2008.

[115] A. Shakouri, “Recent Developments in Semiconductor Thermoelectric Physics and Materials,” *Annu. Rev. Mater. Res.*, vol. 41, no. 1, pp. 399–431, 2011.

[116] J. H. Bahk and A. Shakouri, “Minority carrier blocking to enhance the thermoelectric figure of merit in narrow-band-gap semiconductors,” *Phys. Rev. B*, vol. 93, no. 16, pp. 1–17, 2016.

[117] M. Luisier and G. Klimeck, “Atomistic full-band simulations of silicon nanowire transistors: Effects of electron-phonon scattering,” *Phys. Rev. B - Condens. Matter Mater. Phys.*, vol. 80, no. 15, pp. 1–11, 2009.

[118] M. T. Dunham *et al.*, “Enhanced phonon scattering by nanovoids in high thermoelectric power factor polysilicon thin films,” *Appl. Phys. Lett.*, vol. 109, no. 25, 2016.

[119] Y. He, D. Donadio, and G. Galli, “Morphology and temperature dependence of the thermal conductivity of nanoporous SiGe,” *Nano Lett.*, vol. 11, no. 9, pp. 3608–3611, 2011.

[120] M. Samanta, S. Roychowdhury, J. Ghatak, S. Perumal, and K. Biswas, “Ultrahigh Average Thermoelectric Figure of Merit, Low Lattice Thermal Conductivity and Enhanced Microhardness in Nanostructured (GeTe)x(AgSbSe2)100−x,” *Chem. - A Eur. J.*, vol. 23, no. 31, pp. 7438–7443, 2017.

[121] P. Gorai, V. Stevanović, and E. S. Toberer, “Computationally guided discovery of thermoelectric materials,” *Nat. Rev. Mater.*, vol. 2, p. 17053, 2017.

[122] L. D. Zhao *et al.*, “All-scale hierarchical thermoelectrics: MgTe in PbTe facilitates valence band convergence and suppresses bipolar thermal transport for high performance,” *Energy Environ. Sci.*, vol. 6, no. 11, pp. 3346–3355, 2013.

[123] H. J. Goldsmid, “Bismuth telluride and its alloys as materials for thermoelectric generation,” *Materials (Basel).*, vol. 7, no. 4, pp. 2577–2592, 2014.

[124] M. Lundstrom, “Notes on Bipolar Thermal Conductivity,” vol. 2017, no. 2, pp. 1–8, 2017.

[125] G. J. Snyder and E. S. Toberer, “Complex thermoelectric materials,” *Nat. Mater.*, vol. 7, no. February, pp. 105–114, 2008.

[126] Q. Zhang *et al.*, “Deep defect level engineering: A strategy of optimizing the carrier concentration for high thermoelectric performance,” *Energy Environ. Sci.*, vol. 11, no. 4, pp. 933–940, 2018.

[127] P. G. Burke, B. M. Curtin, J. E. Bowers, and A. C. Gossard, “Minority carrier barrier heterojunctions for improved thermoelectric efficiency,” *Nano Energy*, vol. 12, pp. 735–741, 2015.

[128] H. S. Kim *et al.*, “Suppression of bipolar conduction via bandgap engineering for enhanced thermoelectric performance of p-type Bi0.4Sb1.6Te3alloys,” *J. Alloys Compd.*, vol. 741, pp. 869–874, 2018.

[129] L. Zhang, P. Xiao, L. Shi, G. Henkleman, J. B. Goodenough, and J. Zhou, “Suppressing the bipolar contribution to the thermoelectric properties of MgSiSn by Ge substitution,” *J. Appl. Phys.*, vol. 117, p. 155103, 2015.

[130] S. Foster, M. Thesberg, and N. Neophytou, “Thermoelectric power factor of nanocomposite materials from two-dimensional quantum transport simulations,” *Phys. Rev. B*, vol. 96, no. 19, 2017.

[131] G. Tan, L. D. Zhao, and M. G. Kanatzidis, “Rationally Designing High-Performance Bulk Thermoelectric Materials,” *Chem. Rev.*, vol. 116, no. 19, pp. 12123–12149, 2016.

[132] L. Musland and E. Flage-Larsen, “Thermoelectric effect in superlattices; applicability of coherent and incoherent transport models,” *Comput. Mater. Sci.*, vol. 153, no. 0314, pp. 88–96, 2018.

[133] R. Dettori, C. Melis, X. Cartoixa, R. Rurali, and L. Colombo, “Model for thermal conductivity in nanoporous silicon from atomistic simulations,” *Phys. Rev. B*, vol. 91, p. 054305, 2015.

[134] C. Jeong, R. Kim, M. Luisier, S. Datta, and M. Lundstrom, “On Landauer versus Boltzmann and full band versus effective mass evaluation of thermoelectric transport coefficients,” *J. Appl. Phys.*, vol. 107, no. 2, 2010.

[135] P. Larson, S. Mahanti, and M. G. Kanatzidis, “Electronic structure and transport of Bi_2Te_3 and $BaBiTe_3$,” *Phys. Rev. B*, vol. 61, no. 12, pp. 8162–8171, 2000.

[136] D. Chakraborty, L. de Sousa Oliveira, and N. Neophytou, “Enhanced Phonon Boundary Scattering at High Temperatures in Hierarchically Disordered Nanostructures,” *J. Electron. Mater.*, vol. 48, no. 4, pp. 1909–1916, 2019.

[137] J. C. Irvin, “Resistivity of bulk silicon and of diffused layers in silicon,” *Bell Syst. Tech. J.*, vol. 26, no. 2, pp. 387–401, 1962.

[138] S. M. Lee, D. G. Cahill, and R. Venkatasubramanian, “Thermal conductivity of Si-Ge superlattices,” *Appl. Phys. Lett.*, vol. 70, no. 22, pp. 2957–2959, 1997.